Exopher-like vesicle formation as a novel pathomechanism in the kidney autoimmune disease membranous nephropathy

Dissertation

For the attainment of the academic degree

Doctor of Natural Sciences
(Dr. rer. nat.)

Department of Biology

University of Hamburg

Presented by

Karen Lahme

Hamburg 2025

The presented work was conducted externally in the Department of Physiology in the Institute of Cellular and Integrative Physiology at the University Medical Center Hamburg-Eppendorf under the supervision of Prof. Dr. Catherine Meyer-Schwesinger. Prof. Dr. Julia Kehr supervised this work in the Department of Biology at the University of Hamburg.

1. Reviewer: Prof. Dr. Markus Glatzel
2. Reviewer: Prof. Dr. Catherine Meyer-Schwesinger

Date of the Disputation: 23.09.2025

If you can DREAM it,
you can DO it.

- Walt Disney -

Table of content

List of figures

List of tables

Abbreviations

abs	Antibodies
ACR	Albumin to creatinine ratio
ADR	Adriamycin
ATP	Adenosine triphosphate
BCA	Bicinchoninic acid assay
BRS	Blocking reagent solution
BSA	Bovine serum albumin
BUN	Blood-urea-nitrogen
Ch	Chicken
Dk	Donkey
DMEM	Dulbecco's Modified Eagle's Medium
DMSO	Dimethyl sulfoxide
DN	Diabetic nephropathy
Dtc	Distal tubular cell
DTT	Dithiothreitol
DUB	Deubiquitinating enzyme
ec	Endothelial cell
ECM	Extracellular matrix
EDTA	Ethylenediamine tetraacetic acid
EGTA	Ethylene glycol bis(β-aminoethylether) tetraacetic acid
ELISA	Enzyme-linked immunosorbent assay
ELV	Exopher-like vesicle
EM	Electronmicroscopy
ESRD	End-stage renal disease
EtOH	Ethanol
EV	Extracellular vesicle
FP	Footprocess
FCS	Fetal calf serum
FSGS	Focal segmental glomerulosclerosis
g	g-force
g	Gram
GBM	Glomerular basement membrane
GFP	Green fluorescent protein

GFR	Glomerular filtration rate
Glepp1	Glomerular epithelial protein 1
Gp	Guinea pig
Gt	Goat
HBSS	Hank`s Balanced salt solution
HCl	Hydrochlorid acid
HEPES	4-(2-hydroxyethyl)-1-piperazineethanesulfonic acid
HRP	Horse radish peroxidase
huIgG	Human immunglobulin G
iEM	Immunogold electron microscopy
IF	Immunofluorescence
IgAN	Immunglobulin A Nephropathy
IgG	Immunglobulin subtype G
IP	Immunoprecipitation
IS	ImageStream®
kDA	Kilo dalton
K48-pUB	Lysine-48 polyubiquitine
LAMP2	Lysosomal-associated membrane protein 2
LC-MS/MS	Liquid Chromatography with tandem mass spectrometry
LIMP2	Lysosomal integral membrane protein-2
mAb	Monoclonal antibody
MB594	Membrite 594
mc	Mesangial cell
MCD	Minimal change disease
MGN	Membranous glomerulonephritis
MN	Membranous nephropathy
MP	Major process
MPC	Magnetic particle collector
Ms	Mouse
NaCl	Sodium chloride
NaF	Sodium fluoride
NaN_3	Sodium azide
NaV	Sodium vanadate
NS	Nephrotic syndrome
NTA	Nanoparticle tracking analysis

PBS	Phosphate buffered saline
pc	Podocyte
PD	Pulldown
PFA	Paraformaldehyde
PLA_2R1	M-type phospholipase A2 receptor 1
PMSF	Phenylmethylsulfonyl fluoride
Ptc	Proximal tubular cell
pUB	Poly-Ubiquitin
rb	Rabbit
rbIgG	Rabbit immunoglobulin
rpm	Rounds per minute
SD	Slit diaphragm
SDS	Sodium dodecyl sulfate
SDS-PAGE	Sodium Dodecyl Sulfate – PolyAcrylamid Gel Electrophoresis
SEM	Scanning electron microscopy
SEM	Standard error of the mean
SSC	Side scatter
TBS	Tris buffered saline
TEM	Transmission electron microscopy
THSD7A	Thrombospondin type 1 domain containing 7A
TMB	3,3′,5,5′-Tetramethylbenzidine
UCH-L1	Ubiquitin carboxy-terminal hydrolase L1
uEV	Urinary extracellular vesicle
UPS	Ubiquitin-proteasome system
Veh	Vehicle
WB	Immunoblot
WGA	Wheat germ agglutinin

Zusammenfassung

Podozyten sind spezialisierte Nierenzellen, die für den Erhalt der glomerulären Filtrationsbarriere essenziell sind. Ihre verzahnten Fußfortsätze spielen eine entscheidende Rolle bei der Filtration von Abfallstoffen aus dem Blut. Bei chronischer Nierenerkrankung (chronic kidney disease, CKD), einer Erkrankung, die weltweit etwa jeden zehnten Menschen betrifft, werden Podozyten nach und nach geschädigt und schließlich verloren. Eine der Hauptursachen für CKD ist die Autoimmunerkrankung membranöse Nephropathie (MN).

MN ist gekennzeichnet durch zirkulierende Autoantikörper, die an Proteine der Podozyten-Fußfortsätze binden und Antigen-Antikörper-Komplexe im subepithelialen Raum bilden. Zusätzlich führen Störungen der Proteostase, verursacht durch eine Dysfunktion des Ubiquitin-Proteasom-Systems (UPS), zur Anhäufung beschädigter Proteine, ein Prozess, der in Tiermodellen mit dem Fortschreiten der Erkrankung korreliert. Sowohl die Ablagerung von Immunkomplexen als auch das proteostatische Ungleichgewicht tragen zur Schädigung der Podozyten bei und beeinträchtigen die Integrität der glomerulären Filtrationsbarriere.

Die zellulären Mechanismen, die für die Entfernung von Immunkomplexen und die Aufrechterhaltung der Proteostase in Podozyten verantwortlich sind, sind bislang weitgehend unbekannt. Darüber hinaus ist unklar, warum MN Patient:innen sehr unterschiedliche klinische Verläufe aufweisen. Während einige Patient:innen in ein terminales Nierenversagen übergehen, erreichen andere eine spontane Remission. Die derzeit verfügbaren diagnostischen Methoden, einschließlich Nierenbiopsien und der Messung von Autoantikörpern im Serum, liefern keine direkten Informationen über das Ausmaß der Podozytenschädigung und erlauben keine zuverlässige prognostische Einschätzung, die jedoch notwendig wäre, um die unterschiedlichen Krankheitsverläufe besser zu verstehen.

Diese Studie untersucht eine vielversprechende Alternative: extrazelluläre Vesikel (EVs), die von Podozyten in den Urin abgegeben werden. Diese Vesikel bieten eine nicht-invasive Möglichkeit, die beiden zentralen Mechanismen der Podozytenschädigung, Störungen der Proteinregulation und die Entfernung von Immunkomplexen, zu analysieren und als potenzielle Biomarker für die Überwachung der Podozytengesundheit und des Krankheitsverlaufs bei MN zu nutzen.

Von Podozyten stammende extrazelluläre Vesikel im Urin (p-uEVs) spiegeln die Proteostase der Podozyten krankheitsspezifisch wider. In Mausmodellen variiert die Menge dieser p-uEVs je nach Art und Ausmaß der Podozytenschädigung. Die Proteinzusammensetzung dieser Vesikel, insbesondere im Hinblick auf das UPS, entspricht weitgehend derjenigen der Podozyten selbst, was sie zu einem leistungsfähigen Instrument macht, um den proteostatischen Zustand der Zellen nicht-invasiv zu beurteilen.

Die Studie zeigte außerdem, dass Podozyten unter Stress, ausgelöst durch Proteasom-Inhibition oder autoimmune Schädigung, die Ausschüttung von p-uEVs erhöhen. In einem

THSD7A-assoziierten MN-Mausmodell sowie im Urin von Patient:innen konnten diese p-uEVs als spezifischer Subtyp identifiziert werden, sogenannte exopher-ähnliche Vesikel (exopher-like vesicles, ELVs). Analysen ergaben, dass die Aggregationen im glomerulären Urinraum von Patientenbiopsien Exopheren ähneln und mit dem Urin als ELVs ausgeschieden werden. Darüber hinaus ermöglichte die prospektive Untersuchung von ELVs aus Patient:innen Urin, die Identifikation der krankheitsverursachenden Autoantikörper gebunden an den ELVs, selbst in Fällen, in denen die Standarddiagnostik negative Ergebnisse erbrachte. Damit stellen ELVs einen hochsensitiven und krankheitsspezifischen Biomarker für MN dar.

Diese Ergebnisse unterstreichen die Bedeutung der Vesikelabgabe über ELVs als fundamentalen Podozyten-Mechanismus, um Immunkomplexe zu entfernen und auf proteostatischen Stress zu reagieren. Ihre Entdeckung legt einen neuen pathophysiologischen Mechanismus für MN nahe: Bei einem Angriff durch Autoantikörper binden diese an Antigene der Fußfortsätze, was zur Ablagerung von Immunkomplexen führt. Als Reaktion bilden Podozyten ELVs, um die Komplexe in den Urinraum zu transportieren und dort auszuscheiden. Diese ELVs enthalten sowohl die Autoantikörper als auch krankheitsassoziierte Stressoren und bieten so einen Weg der Entlastung, um die Zellfunktion zu erhalten.

Die Analyse von ELVs eröffnet neue Möglichkeiten für eine sensitive, nicht-invasive Diagnose und Verlaufskontrolle der MN. Darüber hinaus bietet sie einen einzigartigen Einblick in den proteostatischen Zustand der Podozyten. Mit weiterer Entwicklung könnte dieser Ansatz die prognostische Genauigkeit verbessern und neue therapeutische Strategien für Patient:innen mit glomerulären Erkrankungen ermöglichen.

Summary

Podocytes are specialized kidney cells essential for maintaining the glomerular filtration barrier. Their interdigitating foot processes (FPs) play a crucial role in filtering waste from the blood. In chronic kidney disease (CKD), a condition affecting one in ten people worldwide, podocytes are progressively damaged and ultimately lost. One major cause of CKD is the autoimmune disease membranous nephropathy (MN). MN is characterized by circulating autoantibodies that bind to podocyte foot processes proteins, forming antigen-autoantibody aggregates in the subepithelial space. Additionally, disturbances in proteostasis, driven by dysfunction of the ubiquitin-proteasome system (UPS), lead to the accumulation of damaged proteins, a process shown to correlate with disease progression in rodent models. Both immune complex deposition and proteostatic imbalance contribute to podocyte injury and compromise the integrity of the glomerular filtration barrier. The cellular mechanisms responsible for clearing immune complexes and maintaining proteostasis in podocytes remain largely unknown. Furthermore, it remains unclear why MN follows divergent clinical courses, with some patients progressing to end-stage renal disease while others enter spontaneous remission. Current diagnostic tools, including kidney biopsies and serum autoantibody measurements, do not provide direct insights into the extent of podocyte injury or enable reliable prognostic evaluation, which would be needed to unravel the differences in the disease courses.

This study explores a promising diagnostic approach, the use of urinary extracellular vesicles (EVs) released by podocytes into the urine. These vesicles could offer a non-invasive means to study the two key mechanisms of podocyte injury, protein disturbances and immunecomplex accumulation clearance, as potential biomarkers to monitor podocyte health and disease progression in MN.

Podocyte-derived urinary extracellular vesicles (p-uEVs) reflect podocyte proteostasis in a disease-specific manner. In mouse models the p-uEV abundance changes in a disease specific manner, depending on the underlying podocyte injury. The protein composition of the p-uEVs, particularly regarding the UPS, mirrors that of podocytes, making p-uEVs a powerful tool to assess the proteostatic status of podocytes non-invasively. This study further discovered that podocytes increase p-uEV release in response to stress, achieved by proteasomal inhibition or by autoimmune-mediated injury. In a THSD7A-associated MN mouse model and in patient urine, these p-uEVs were identified as a specific EV subtype called exopher-like vesicles (ELVs). Analyses revealed that the glomerular urinary space aggregates in patient biopsies resembled ELVs and were released into the urine. Additionally, prospective studies of patient ELVs allowed the identification of the disease-causing autoantibody bound to ELVs and thus facilitate the detection of immune activity in MN patients, even when standard diagnostics failed. This makes ELVs a highly sensitive and disease-specific biomarker for MN.

Together, these findings highlight vesicle shedding via ELVs as a fundamental podocyte response mechanism, balancing immune complex removal and adaptation to proteostatic stress. Their discovery proposes a novel pathomechanism for MN: when podocytes are attacked by autoantibodies, the binding to foot process antigens leads to a deposition of immune complex aggregates. The podocyte responds with ELV formation, translocating the immune complex to the urinary space and releases them into the urine. These ELVs carry the autoantibody, and disease associated stressors, offering a clearance route for the podocyte to maintain function. ELV analysis opens new possibilities for the sensitive, non-invasive diagnosis and monitoring of MN. It also offers a unique window into the proteostatic health of podocytes. With further development, this approach could enhance prognostic accuracy and lead to novel therapeutic strategies for patients with glomerular disease.

1 Introduction

1.1 The kidney - the body's key regulator of physiological health

The kidneys are vital, bean-shaped organs located in the posterior abdominal cavity on either side of the spine. Encased in a fibrous capsule and cushioned by layers of adipose tissue, they function as the body's primary filtration system[1, 2], by filtering blood to remove waste products [3, 4]. Therefore, the kidney filters about 150 liter of blood per day, whereby only a fraction of the whole, approximately 1.5 liter becomes urine[5]. Beyond the important function of filtration, the kidneys maintain homeostasis by regulating fluid and electrolyte balance, blood pressure, controlling acid-base balance, and producing hormones[6]. Blood circulates through the kidneys, where essential nutrients, like glucose, electrolytes, and water are selectively reabsorbed, and waste products like urea and creatinine are excreted within urine[7]. The kidneys produce hormones such as erythropoietin, which stimulates red blood cell production, and renin, which plays a role in blood pressure regulation[8-10]. Further, they are also involved in maintaining acid-base balance by excreting hydrogen ions and reabsorbing bicarbonate from the urine. This process helps to keep the blood's pH within a narrow, physiological range, ensuring that metabolic processes can continue unhindered[2]. Additionally, the kidneys play a role in vitamin D metabolism, converting inactive vitamin D into its active form (calcitriol), which is essential for calcium homeostasis and bone health[11].

With this the kidneys are essential to various systems within the body, ensuring the proper functioning and making the kidneys indispensable for maintaining general physiological stability and health[12].

1.1.1 Structure and composition of the kidney

The kidney is divided into three main regions, the renal cortex, renal medulla, and renal pelvis, of which each plays a unique role in renal function. The renal cortex is the outer layer of the kidney, where the renal nephrons, the structures responsible for blood filtration, are located. Beneath the cortex lies the renal medulla, an inner region composed of pyramid-shaped subunits known as renal pyramids. These structures contain loops of Henle and collecting ducts, which concentrate urine and transport it toward the renal pelvis. The renal pelvis, a central funnel-shaped cavity, collects urine produced by the nephrons and directs it into the ureter, which transports it to the bladder for excretion (Fig. 1). The renal hilum, a key anatomical feature, serves as the entry and exit point for the renal artery, renal vein, and ureter, ensuring efficient vascular and urinary transport[2, 7, 13].

The precise organization of these regions supports the kidney's ability to efficiently filter blood and produce urine.

1.1.2 Nephron - the functional unit

The nephron is the basic functional unit, responsible for the crucial processes of blood filtration and urine formation. Each kidney contains approximately one million nephrons, each comprising the two main parts, a renal corpuscle and a renal tubule[14]. The renal corpuscle consists of the glomerulus, harbouring a dense network of capillaries where the blood filtration occurs (described in more detail below), and the Bowman's capsule, which encases the glomerulus, separates it from the tubular system and collects the primary urine filtrate. The renal tubule is divided into the proximal tubule, loop of Henle, distal tubule, and collecting duct (Fig. 1). These segments play a crucial role in reabsorbing water, ions, and nutrients further facilitating the secretion of additional waste into the filtrate, as described in more detail below.

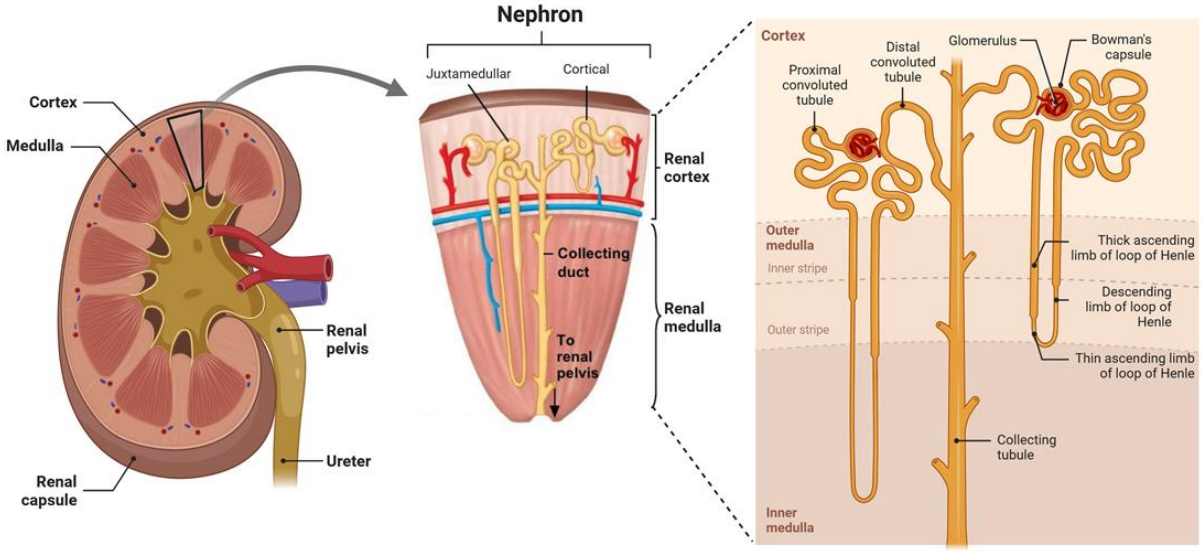

Figure 1: Structure of the kidney and nephron. Scheme created with Biorender and modified from Pearson Education, Inc., publishing as Benjamin Cummings Copyright 2008.

1.1.2.1 Glomerulus - the filtration unit

The glomerulus, with its specialized network of capillaries (glomerular tuft), formed by endothelial cells and surrounded by epithelial and mesangial cells within the Bowman's capsule, is the heart of the filtration process (Fig. 2A). Blood flows through the supplying arterioles into the glomerulus, whereby the resistance in the capillaries generates high pressure, together with concentration and osmolarity gradients enables the ultrafiltration across the multi-layered glomerular barrier into the urinary space in the Bowman's capsule[6]. The glomerular capillary barrier has a unique structure that allows for efficient filtration. This barrier consists of three layers. The fenestrated endothelium of these capillaries features small pores that enable the rapid passage of water and small molecules, while restricting blood cells[15]. Beneath the endothelium lies the glomerular basement membrane, a dense

extracellular matrix, selective according to size and charge, which prevents the passage of larger molecules, like the serum protein albumin[16-19]. Surrounding the capillaries with their cell body are podocytes, specialized epithelial cells with foot processes that interdigitate with the foot processes of neighboring podocytes, forming filtration slits. These podocytes are essential in maintaining the integrity of the filtration barrier[6, 20], as described in detail below. The blood leaves the glomerulus through the efferent arteriole, which is now free of waste products but contains as well small molecules like electrolytes and glucose. The filtered fluid, known as glomerular or primary filtrate, collected in Bowman's space travels through the renal tubule for further processing and reabsorption of filtered small molecules[3].

1.1.2.2 Podocytes – the gatekeepers of filtration

Podocytes are integral cells in the kidney's filtration system, often described as the key cells of the renal filter. They play a critical role in maintaining the glomerular filtration barrier and adapting to physiological and pathological stressors. These cells are highly specialized, mesenchymal-derived epithelial cells that are terminally differentiated[21]. These cell bodies house essential organelles, including the nucleus, Golgi apparatus, endoplasmic reticulum, lysosomes, and mitochondria, reflecting high anabolic and catabolic activity[22, 23]. These cells exhibit apico-basal polarity, allowing them to orient between the urinary space and the glomerular basement membrane (GBM)[24, 25]. While podocyte foot processes anchor to the GBM, their cell bodies remain freely suspended in the capsular space. Podocytes wrap around the glomerular capillaries with their flat cell bodies and extend 5 to 10 long, branching major (primary) processes. These major processes give rise to numerous secondary processes, often referred to as foot processes (FPs), which interdigitate in a zipper-like fashion with the foot processes of neighboring podocytes[13]. This intricate interdigitation forms the filtration slits essential for the kidney's ability to filter blood (Fig. 2). The podocyte cytoskeleton is fundamental to maintain morphology, elasticity, and resistance to contractile capillary forces[26]. The cell body and primary processes contain microtubules (24 nm) and intermediate filaments (10 nm), while the secondary foot processes primarily rely on microfilaments (7-9 nm), composed mainly of filamentous actin[27-30]. Actin filaments, arranged in bundles interconnected by α-actinin-4 and myosin, provide structural integrity and interact dynamically with microtubules[31]. The foot processes anchor to the GBM through focal adhesion complexes, including integrins, syndecans, vinculin, talin, and dystroglycan, which link the actin cytoskeleton to extracellular matrix proteins such as laminin, entactin, collagen IV, and agrin[32-34]. The foot processes are interconnected by specialized cell-cell contacts known as slit diaphragms (SD), which are highly specialized molecular filters composed of key proteins such as the transmembrane proteins Nephrin and Neph1, integral membrane proteins like podocin and signaling adaptors e.g. CD2AP[35] (Fig. 2B). This structure selectively prevents

large molecules and proteins from passing into the filtrate and ensure the structural plasticity of the FP [23, 36, 37]. Nephrin and Neph1 form a zipper-like network that stabilizes the filtration barrier, while podocin, a stomatin family protein, anchors nephrin to the plasma membrane [33, 38]. Mutations or damage to slit diaphragm proteins can lead to an impaired filtration and allows proteins to breach the barrier. Podocytes are responsible for synthesizing and secreting key GBM components such as collagen IV, laminin, entactin, and agrin[22, 32, 39], leading to stabilization and functional integrity of the GBM.

Despite their critical role in the filtration process, podocytes are exposed to a variety of environmental stressors. These include metabolic, toxic, and immune-related challenges from both the blood and the urinary side of the filtration barrier. As a result, podocytes are highly susceptible to injury, and upon damage, they undergo a uniform morphological reaction characterized by cytoskeletal reorganization, foot process effacement, cytosolic vacuolization, and hypertrophy[40, 41]. Over 80 different pathways have been implicated in podocyte distress, involving circulating factors, cell-surface signaling, metabolism, fibrosis, inflammation, and changes to the actin cytoskeleton[42]. Many of these pathways are connected to developmental programs, such as those mediated by the Notch, Wnt, and mTOR pathways. Disruption of these pathways can lead to protein homeostasis imbalances and energy metabolism disturbances, which, when prolonged, result in irreversible dedifferentiation or loss of the podocytes[43, 44]. When podocytes are damaged, they become less specialized, losing their ability to maintain the filtration barrier, leading to progressive renal dysfunction. A key feature of this dysfunction is the alteration in protein homeostasis. Research in animal models has shown that enhanced abundance of the ubiquitin-proteasomal system (UPS) and autophagosomal-lysosomal pathways (ALP) accompanies podocyte injury[45-48]. These pathways are involved in degrading and recycling damaged proteins. However, when they are impaired, they fail to maintain cellular protein quality, leading to accumulation of misfolded proteins within the podocytes. At the same time, the proteolytic systems that normally degrade damaged proteins become impaired, contributing to the buildup of these aggrieved proteins, which further disrupt podocyte function and integrity[45, 49, 50].

The disruption of these central intracellular signaling pathways leads to a cascade of events that gradually impair podocyte structure and function, culminating in dedifferentiation[50, 51]. As the podocytes lose their specialized properties, they are no longer able to fulfill their critical role in the filtration process, resulting in a loss of serum proteins into the urine, thereby contributing to the progression of kidney disease. Clinically, such injury manifests as nephrotic syndrome, marked by the overall accepted hallmarks like hyperlipidemia, hypoalbuminemia and proteinuria.

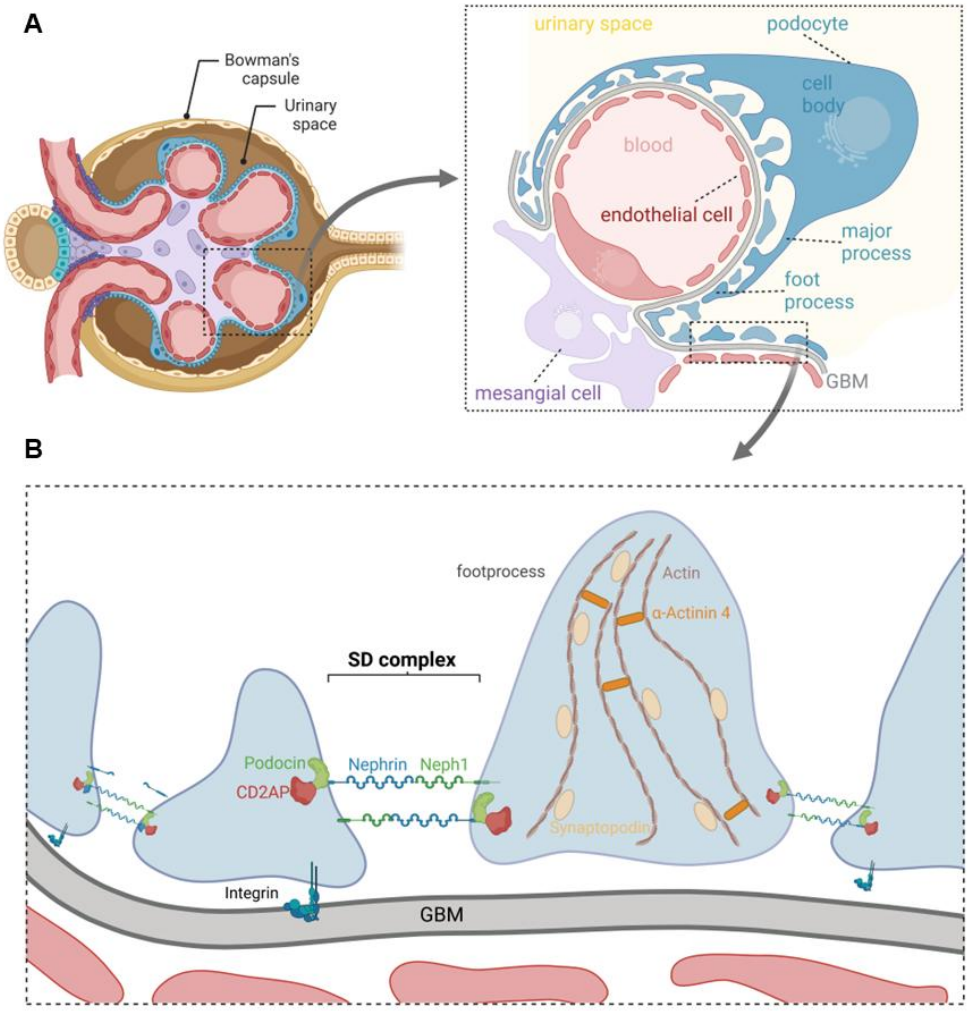

Figure 2: Structure of the glomerulus and slit diaphragm. Simple illustration depicts **A)** structure of the glomerulus, built up by mesangial (purple), endothelial (red), and podocyte cells (blue) within epithelial cells of the Bowman's capsule and **B)** main proteins important for slit diaphragm assembly and podocyte foot process structure, together with the GBM and endothelial cells forming the filtration barrier. GBM= glomerular basement membrane, SD= slit diaphragm. Scheme created with Biorender.

1.1.2.3 Renal tubular system - the reabsorption unit

Once the blood is filtered through the glomerulus, the primary urine moves on to the renal tubule, where further processing occurs. Consisting of proximal tubule, loop of Henle, distal and connecting tubules, finally ending in the collecting duct, the tubular system is responsible for the reabsorption of vital substances and the excretion of additional waste products into the filtrate, processing the concentrated final urine[6]. Cells along the tubular system, like proximal and distal tubular cells, are able to take up molecules or vesicles from the primary urine, in a targeted or random manner, that have been secreted by other cells as waste or as a means of cell-cell communication[52].

By adjusting the volume and composition of the urine, the kidneys regulate the body's fluid balance and maintain proper concentrations of electrolytes. This process also helps to regulate blood pressure, as they can alter the volume of fluid in the body by controlling how much is reabsorbed or excreted[53]. Additionally, the control of bicarbonate reabsorption to regulate the acid-base balance is a crucial function of the tubular system[6, 54].

1.2 Nephropathy and nephrotic syndrome

Nephropathy refers in the broadest sense to kidney disorders or damage and includes various kidney diseases. If the glomeruli are specifically affected, this is referred to as a glomerulopathy, while diseases that only affect the podocytes are called podocytopathies. Both can have inflammatory or non-inflammatory origins, leading to either nephritic or nephrotic syndrome, respectively**[55, 56]**.

The nephrotic syndrome (NS) is one of the most prevalent disorders in the field of nephrology[57, 58]. The exact causes of NS remain unknown, but it is characterized by increased permeability of the glomerular filtration barrier. Persistent nephrotic syndrome has a poor prognosis, often progressing to end-stage renal failure and posing a life-threatening risk due to cardiovascular complications as a consequence of plasma protein loss and altered lipid metabolism[57, 59]. The main clinical criteria in patients suffering from NS are, besides the urinary protein loss, often more than 3.5 g per day, edema as well as hypoalbuminemia and hyperlipidemia in the serum.

From a pathological perspective, nephrotic syndrome is primarily associated with three well-defined disease patterns: 1) minimal change disease (MCD), 2) focal segmental glomerulosclerosis (FSGS), and 3) membranous glomerulonephritis (MGN)[57, 60], described in more detail later. These diseases, which are summarized under the term primary podocytopathies, are primarily due to damage to the podocytes, which manifests itself in extensive narrowing of the foot process, disruption of the slit diaphragm and subsequent glomerular protein leakage. While the exact mechanisms behind podocyte injury remain unclear, it is evident that podocytes, crucial for the glomerular filtration barrier, are particularly vulnerable in nephrotic syndrome. The specific pathological changes depend on the underlying cause of the disease. In the following, different glomerulopathies and podocytopathies relevant for this work are described in more detail.

1.2.1 Glomerulonephropathies

1.2.1.1 Diabetic nephropathy

Diabetic nephropathy (DN), also known as diabetic kidney disease, is one of the main causes of end-stage renal failure worldwide and is a growing problem due to the increasing prevalence of type 1 and 2 diabetes[61, 62]. The early stages of DN are marked by increased kidney size, glomerular hypertrophy, and hyperfiltration. As the disease progresses, patients develop strong proteinuria (>300 mg/day), accompanied by mesangial cell proliferation, extracellular matrix (ECM) accumulation, and ultimately glomerulosclerosis[63, 64]. Clinically, DN is recognized by persistent hyperglycemia, hypertension, and progressive proteinuria, but its underlying mechanisms remain highly complex and not yet fully understood.[61, 65-69].

1.2.1.2 IgA nephropathy

Immunoglobulin A nephropathy (IgAN) is the most common form of primary glomerulonephritis, characterized by the mesangial deposition of IgA1, in some cases also IgG or IgM and is often accompanied by complement protein C3, leading to the stimulation of inflammatory components[70-72]. More than 50% of IgAN patients exhibit elevated serum IgA levels and circulating IgA-containing immune complexes (CICs)[73, 74]. Research suggests that these mesangial IgA deposits originate from CICs containing abnormally glycosylated polymeric IgA1, which plays a key role in glomerular injury[75-79]. The pathogenesis of IgAN is believed to involve four interrelated mechanisms, commonly referred to as "Hits 1–4"[80]. In brief, 1) an increased level of circulating galactose-deficient IgA1 and 2) the production and binding of unique anti-glycan antibodies, lead to 3) the formation of pathogenic IgA1-containing CICs, which 4) deposits in mesangial cells. These processes drive glomerular damage, leading to mesangial cell proliferation, extracellular matrix expansion and cytokine activation[80, 81]. Clinically, patients typically present with proteinuria and hematuria in the early stages, which can progress to nephrotic syndrome over time. Without intervention, a significant proportion of patients will suffer kidney failure within 10–15 years of diagnosis[82-84].

1.2.1.3 Toxic nephropathy

Toxic nephropathy refers to kidney damage caused by toxins, often presenting with non-specific symptoms. This is not surprising, as being the primary organ for filtration and excretion, the kidney is particularly vulnerable to toxins. The risk of nephrotoxicity depends on the structure, dosage, metabolism, and excretory pathway of the substance. This damage can affect the glomerulus, vasculature, or tubulointerstitium, leading to partial or complete dysfunction of the affected structures[85]. Both, endogenous toxins (such as myoglobin and

hemoglobin) and exogenous substances (including medications, heavy metals, intoxicants, and environmental pollutants) have been implicated, with drugs being a common cause of kidney injury[86-88]. Clinical manifestations vary based on the site and severity of the damage. In many cases, toxicity-induced kidney injury is reversible if exposure to the harmful substance is limited. However, prolonged exposure can lead to irreversible renal damage[87].

Patients typically present with acute kidney injury, characterized by reduced glomerular filtration rate (GFR) and impaired solute transport. Depending on whether the glomerulus, vasculature, or tubules are affected, additional specific symptoms may occur, and the affected parts have to be identified through histological analysis[87, 89].

1.2.2 Podocytopathies

1.2.2.1 Membranous nephropathy (MN)

Membranous nephropathy (MN) is the most common cause of nephrotic syndrome in adult Caucasian[90, 91]. With an incidence of approximately 1 in 100,000, MN is one of the most glomerular diseases, predominantly affecting men[92]. MN can occur as a primary (idiopathic) glomerular disease or as a secondary cause due to systemic lupus erythematosus, infections (e.g., hepatitis B, HIV, malaria), toxin exposure, certain drugs (e.g., gold salts, penicillamine, NSAIDs), or malignancies[93-95]. THSD7A-positive MN is strongly associated with malignancies, with 20% of affected patients diagnosed with cancer within three months of MN detection[96]. MN is diagnosed through kidney biopsy, which reveals characteristic granular immune deposits along the glomerular capillary loops, electron-dense subepithelial deposits within the GBM and the proof of circulating autoantibodies in the serum (serum titer)[97, 98]. The clinical course of MN is highly variable, about 25% of patients achieve spontaneous remission while maintaining kidney function, whereas one-third progress to dialysis-dependent kidney failure within 10 to 15 years despite immunosuppressive therapy. Further, around 40% of MN patients develop end-stage renal disease (ESRD), while another subset of patients presents with persistent moderate proteinuria (3-5 g per day) but stable kidney function, requiring only supportive treatment[94].

The pathogenesis of MN is not yet fully understood, but it is an autoimmune disease in which autoantibodies are directed against important foot process proteins of the podocytes, resulting in the formation and deposition of immune complexes at the filtration barrier (Fig. 3). The antigen-autoantibody accumulations trigger podocyte damage with foot process effacement and stimulating extracellular matrix production, leading to GBM thickening as the disease progresses[98, 99], overall resulting in podocyte injury and subsequent proteinuria[98, 100]. Further, this binding of circulating autoantibodies to podocyte antigens is believed to activate the

complement system. Complement-dependent[101, 102] and complement-independent[103, 104] pathways are recognized to drive podocyte injury in MN.

The identification of the M-type phospholipase A2 receptor (PLA_2R1)[105] and thrombospondin type-1 domain-containing 7A (THSD7A)[106] as target antigens marked a significant breakthrough in MN research, with autoantibody titers correlating with disease activity and serving as diagnostic and prognostic biomarkers[105, 107-110]. They are the most well-characterized autoantigens, approximately 80% of MN patients are PLA_2R1-autoantibody positive, while only 5% exhibit THSD7A autoantibodies, suggesting the involvement of additional, yet-to-be-identified podocyte antigens [99] for the 15% of MN patients who are PLA_2R1- and THSD7A-negative, as well as those with autoimmune-associated secondary MN. Recent studies have identified potential new antigens, such as Nell1[111], NCAM1[112] as well as exostosin 1 (EXT1) and exostosin 2 (EXT2), which both are particularly associated with lupus nephritis[113].

Current MN treatments rely on general immunosuppressive therapies, but new approaches are being developed to specifically target B-cell depleting agents like rituximab by as well as novel complement inhibitors to target the complement system[114, 115].

As one of the leading causes of nephrotic syndrome and ESRD, MN remains a major clinical challenge[90, 116]. Despite the well-characterized immune deposition patterns, the precise molecular events driving antigen accumulation and immune complex formation in MN are still not fully elucidated. A deeper understanding of these mechanisms is essential for advancing targeted therapies and improving patient outcomes.

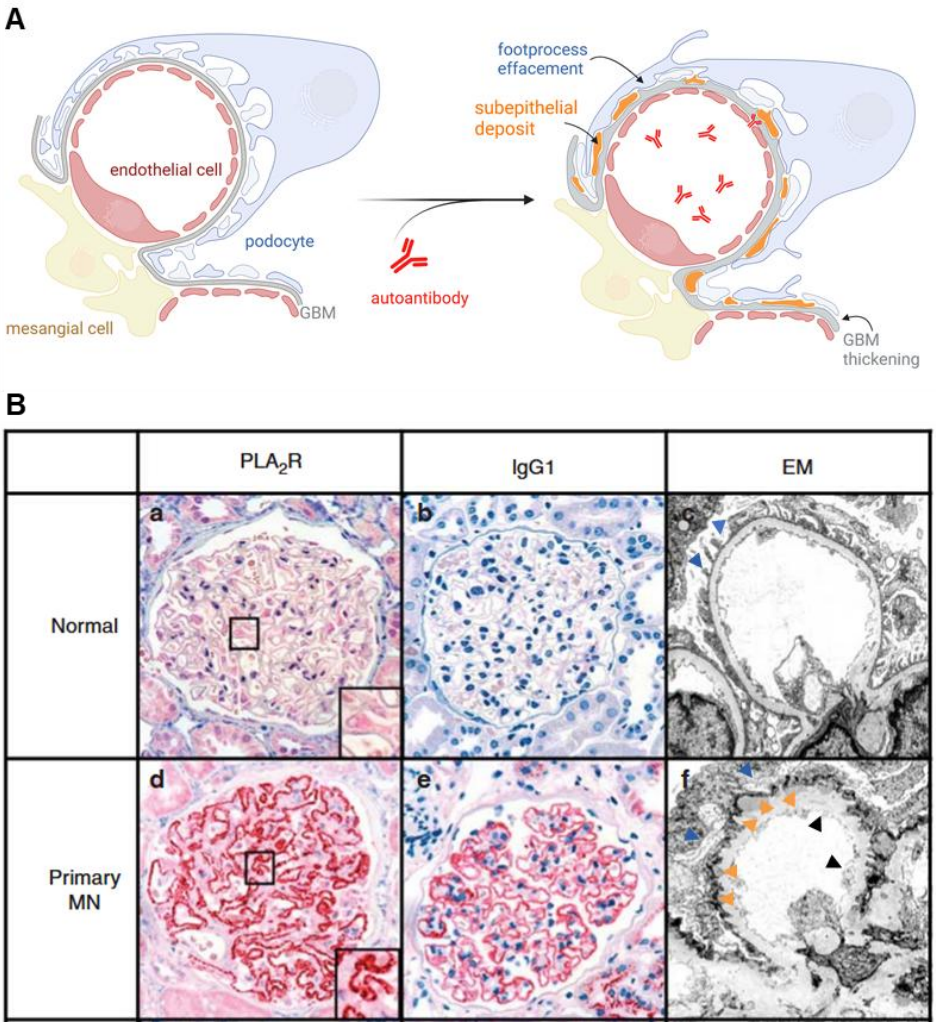

Figure 3: Membranous nephropathy pathology. A) Scheme of main hallmarks in MN induced by circulating autoantibody binding to podocyte foot process proteins (created with Biorender). **B)** Immunohistochemical staining (APAAP method; original magnification x 1.140) of PLA_2R1 and IgG1 and transmission electron microscopy (EM; original magnification x 7.000) of renal biopsies from a normal kidney (a-c) and from a primary PLA_2R1^+-MN patient (d-f). Foot processes (normal) and FP effacement (MN) are highlighted with blue arrows. Subepithelial deposits along the GBM underneath the podocytes FP are depicted by orange and GBM thickening by black arrows (modified from Hoxha et al. 2012, Kidney International).

1.2.2.2 Minimal change disease (MCD)

Minimal change disease (MCD) is a glomerular disorder characterized by the absence of significant abnormalities under light microscopy, only subtile changes can be detected, such as mild mesangial expansion or vacuolization. This lack of pronounced structural damage is a defining hallmark of MCD in patient biopsies[117]. A key diagnostic feature of MCD is the diffuse effacement of podocyte foot processes, which can only be visualized using electron microscopy. This effacement leads to the loss of filtration barrier integrity, resulting in severe proteinuria. Additionally, an increase in lysosomes and cytoplasmic vacuoles is often observed in affected podocytes. Despite these cellular alterations, the GBM remains structurally intact,

distinguishing MCD from other glomerulopathies that involve basement membrane thickening or immune complex deposition[57].

1.2.2.3 Focal segmental glomerulosclerosis (FSGS)

Idiopathic FSGS, also referred to as primary FSGS, encompasses a broad spectrum of morphological patterns and underlying causes[118]. The name is derived from two characteristics of the disease. Firstly, the disease initially occurs focally, i.e. only a limited number of glomeruli are affected. Secondly, only certain capillary loops within these glomeruli are affected, i.e. it occurs segmentally. These affected loops eventually collapse, which is often accompanied by the accumulation of hyaline material. Another common finding in FSGS is the adhesion of these sclerotic regions to Bowman's capsule. While unaffected portions of the glomeruli typically appear normal, mesangial expansion may occasionally be observed, as well as podocyte foot process effacement. Historically, a histological diagnosis of FSGS required the identification of segmental sclerotic lesions in at least one glomerulus. However, more recent diagnostic criteria have expanded to include non-sclerotic glomerular lesions[12, 119]. To distinguish idiopathic FSGS from secondary forms, which result from pathogenic events such as nephron loss, structural abnormalities, or mutations in podocyte-associated genes, the term idiopathic FSGS was introduced[120, 121]. Unlike primary FSGS, many secondary forms do not exhibit complete podocyte foot process effacement, providing a histological distinction between the two[57, 122, 123].

1.3 Mouse models for the study

1.3.1 Diabetic nephropathy

The BTBR (Black and Tan, Brachyury) *ob/ob* leptin-deficient mouse strain was utilized to investigate DN in mice. Under normal chow conditions, BTBR mice exhibit hyperinsulinemia, indicative of insulin resistance, a hallmark of type 2 diabetes[124]. However, insulin resistance alone does not fully define the disease. Obesity is a significant independent risk factor for type 2 diabetes, therefore the *ob/ob* mutation was additionally introduced into the BTBR background[125]. This mutation leads to a leptin deficiency, resulting in obesity and, in combination with insulin resistance, ultimately progressing to type 2 diabetes[126]. BTBR *ob/ob* mice exhibit marked hyperglycemia (350–400 mg/dl) and significantly increased body weight compared to their littermates. From four weeks of age, they develop progressive albuminuria, which increases more than tenfold at week 20[127]. Additionally, these mice show key structural and functional changes, such as glomerular hypertrophy, capillary basement membrane

thickening, and podocyte loss, all pathological features closely resembling human diabetic glomerular injury[127]. Major advantage of the BTBR *ob/ob* model is the rapid disease progression (18–20 weeks) which enables the studying of metabolically induced podocyte injury in a rather short timeframe[128].

1.3.2 Toxic nephropathy

A well-established rodent model for toxic nephropathy is induced by adriamycin (ADR), a widely used chemotherapeutic agent. Initially, ADR triggers chemical and toxic renal injury, which progressively leads to immune and structural alterations, resulting in significant tissue damage[129, 130]. This ADR-induced nephropathy, particularly in its immune-mediated chronic proteinuric phase, serves as an experimental analogue of human FSGS[131-133]. Among various mouse strains, BALB/c mice are recognized as a dose-dependent yet highly reliable model for establishing stable ADR nephropathy[131]. The disease is characterized by the onset of nephrotic syndrome, marked by increased proteinuria as early as three days post-ADR injection. With disease progression pathological, ultrastructural, and functional abnormalities emerge, including focal glomerulosclerosis, interstitial expansion, and immune cell infiltration, histological hallmarks that closely resemble chronic kidney diseases in humans [131, 133, 134]. ADR-induced damage to endothelial cells and podocytes has been well documented by Sun et al., shedding light on the underlying pathogenesis of the disease[135, 136].

1.3.3 Membranous nephropathy

To study antibody-mediated podocyte injury, passive disease models are used and rely on the injection of disease-inducing antibodies that specifically target the relevant antigen. Thrombospondin type 1 domain-containing 7A (THSD7A) and M-type phospholipase A2 receptor 1 (PLA_2R1), both play a crucial role in MN. The identification of THSD7A and PLA_2R1 as the primary target antigens in most idiopathic MN cases has been a major breakthrough, opening new avenues for research[105, 106, 137]. However, endogenous PLA_2R1-based rodent models are unavailable, as rodents do not express PLA_2R1 on the podocyte surface. In contrast, THSD7A is constitutively expressed in rodents, allowing for the development of reliable $THSD7A^+$-MN mouse models[137-139]. This passive $THSD7A^+$- MN model is induced by the intravenous administration of rabbit anti-THSD7A antibodies (rbTHSD7A-abs), which bind to the extracellular region of THSD7A. Similar to the autoantibodies found in $THSD7A^+$-MN patients, rbTHSD7A-abs recognize THSD7A in a conformation-dependent manner[138, 139]. THSD7A is localized at the basal part of the podocyte foot processes, adjacent to the slit diaphragm and beneath Nephrin[104]. Consequently, autoantibody binding occurs rapidly at the subepithelial aspect of foot processes, particularly near the slit diaphragm region. The mice

develop proteinuria within 1–3 days [104]. In this model, glomerular accumulations of THSD7A and rbTHSD7A-abs appear in a pattern similar to that seen in human THSD7A$^+$-MN patients, though at a lower intensity[139]. Therefore, the THSD7A$^+$-MN model as our antibody-mediated injury model was selected for this study.

1.4 Ubiquitin proteasome system (UPS)

Maintaining cellular homeostasis requires a delicate balance between protein synthesis, quality control, and degradation. To regulate protein turnover, cells utilize multiple protein degradation systems, with the ubiquitin-proteasome system (UPS) being the primary pathway responsible for the degradation of misfolded, damaged, or regulatory proteins. This system serves as a crucial quality control mechanism, ensuring proper cellular proteostasis by degrading over 80% of intracellular proteins[140, 141].

Proteins are targeted for proteasomal degradation by ATP-dependant ubiquitination at lysine residues through a three-step enzymatic cascade. This process consists of: 1) ubiquitin activation (E1), in which ubiquitin is activated in an ATP-dependent manner, 2) ubiquitin conjugation (E2), the activated ubiquitin is transferred to an E2 enzyme and 3) ubiquitin ligation (E3), the E3 ligase facilitates the transfer of ubiquitin to the target protein's lysine residue[142] (Fig. 4). Successive rounds of this process generate polyubiquitinated proteins, where the length and branching pattern of ubiquitin chains determine the protein's cellular fate. These chains are further regulated by deubiquitinating enzymes (DUBs), which can edit or remove ubiquitin modifications[143]. Substrates polyubiquitinated via lysine 48 (K48) linkages, with at least four ubiquitin molecules attached, are predominantely shuttled to the proteasome for degradation[144, 145].

The proteasome is a multi-subunit proteolytic complex that exists in several structural forms. The constitutive 26S/30S proteasome consists of two main components. The 20S Core Particle (CP) is the catalytically active part of the proteasome. It is composed of four stacked rings, two outer α-rings, which regulate substrate entry and two inner β-rings, containing the three proteolytic active β-subunits β1c, β2c and β5c. These three catalytic subunits differ from one another in their cleavage specificity: β1 cleaves mainly after acidic amino acids (caspase-like activity), β2 preferantially after basic amino acids (trypsin-like activity) and β5 cleaves after hydrophobic amino acids (chymotrypsin-like activity). The 19S regulatory particle is functionally connected to the 20S CP by a gated protein translocation channel. This complex recognizes, unfolds, and translocates ubiquitinated proteins into the 20S core for degradation. Together both parts building up the 26S/30s proteasome [46, 146, 147] (Fig. 4).

Cells possess the ability to dynamically adjust their proteolytic capacity by inducing the immunoproteasome, a specialized variant of the constitutive proteasome that is activated in response to pro-inflammatory interferon signaling[148-150]. The immunoproteasome incorporates

distinct catalytic β-subunits into the 20S CP, β5i (also known as Lmp7), β1i, and β2i (Fig. 4). The immunosubunits have different cleavage specificites than their constitutive counterparts. This modification enhances the generation of peptides, particularly antigenic peptides suitable for MHC class I presentation[46, 148]. Studies using rat and mouse models of chronic podocyte injury have revealed that while injured podocytes upregulate the immunoproteasome, its enzymatic function becomes impaired[45]. This impairment leads to the accumulation of K48-linked polyubiquitinated proteins, which are typically destined for degradation but fail to be efficiently processed[45, 46]. One key contributor to this dysfunction is the oxidative modification of UPS enzymes, such as the deubiquitinating enzyme ubiquitin carboxy-terminal hydrolase L1 (UCH-L1). Interestingly, UCH-L1 is selectively expressed in injured podocytes across all species in a de novo manner. However, under conditions of cellular stress, UCH-L1 undergoes modifications that render it enzymatically inactive, further exacerbating proteasomal dysfunction[49, 151-153].

Notably, the expression levels of UPS-related proteins such as LMP7 and UCH-L1 in human biopsy samples and experimental rodent models often do not correlate with their actual functional activity. This discrepancy poses challenges for diagnostic and prognostic assessments.

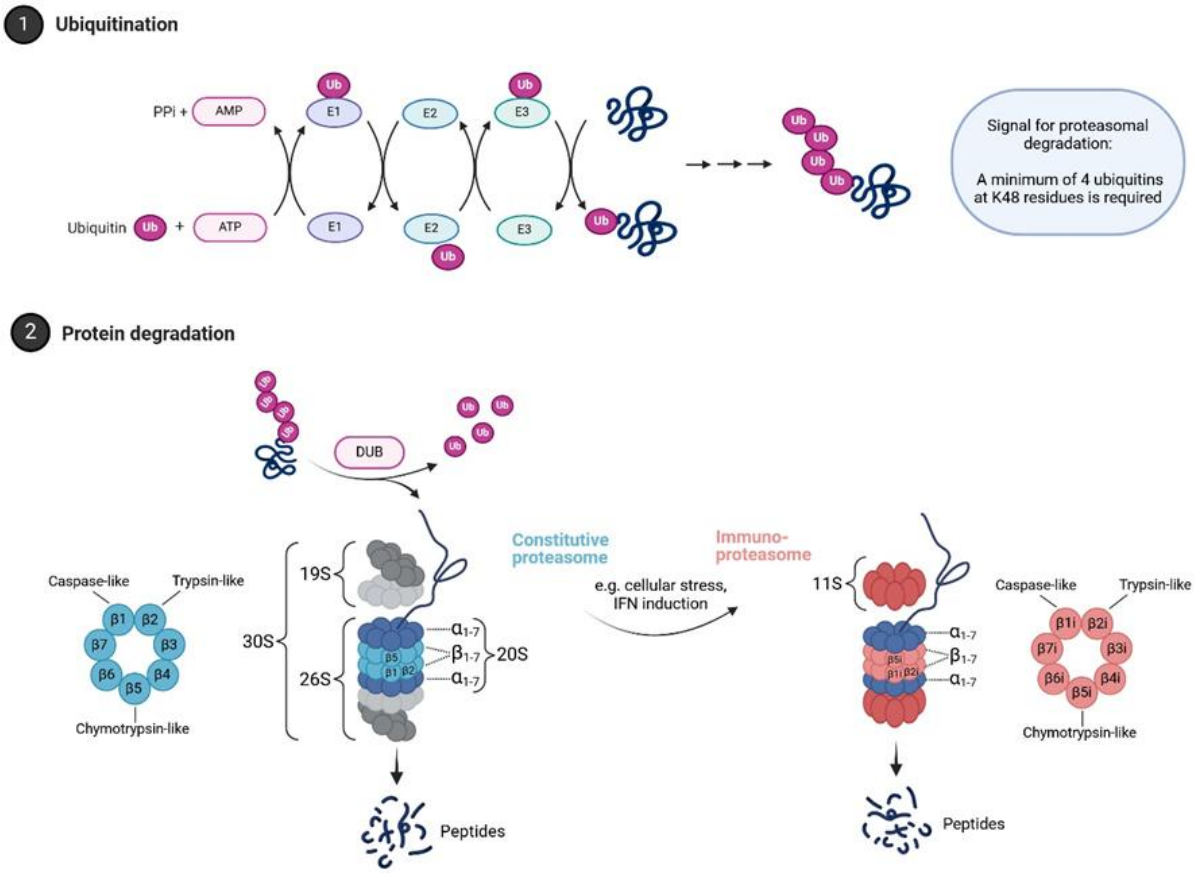

Figure 4: Protein degradation by ubiquitin proteasome system. A) Enzymatic cascade of protein ubiquitination. **B)** Structure of constitutive and immunoproteasom for protein degradation. Scheme created with Biorender.

1.5 Extracellular vesicles

Extracellular vesicles (EVs) are a heterogenous population (Fig. 5), surrounded by a lipid bilayer membrane and secreted by nearly all cell types, playing a crucial role in intercellular communication[154-157]. Originally, they were thought to be cellular waste, EVs are now recognized as key players in cell signaling and serving as potential biomarkers and hold promise for non-invasive diagnostics and therapeutic applications[158]. The ability of EVs to deliver their cargo to specific cells is being explored for therapeutic purposes. Understanding their mechanisms of release, cargo selection, and uptake is crucial for harnessing their potential in clinical applications[159]. They carry proteins, lipids, mRNA, and DNA, influencing processes such as immune responses, tissue repair and inflammation[160, 161]. Their composition and abundance changes in pathological conditions, contributing to disease progression through immune activation, coagulation, or cellular injury while also exhibiting protective and regenerative properties. Found in blood, saliva, urine, and other body fluids, as well as altering recipient cell function. Their role extends beyond normal physiology to pathological conditions, where excessive EV release can contribute to inflammation,

malignancy, and disease progression. EV release is influenced by various stimuli, including cytokines, pro-inflammatory signals, hypoxia, cellular injury, and stress conditions[159]. The regulation of EV biogenesis involves complex molecular mechanisms, including endosomal-sorting-complex-required-for-transport (ESCRT) proteins[162, 163], RAB GTPases[164], and lipid remodeling pathways. Their uptake by recipient cells occurs via endocytosis, membrane fusion, or receptor-ligand interactions, depending on surface proteins and extracellular conditions[165, 166]. EVs exhibit molecular and structural heterogeneity, which presents both opportunities and challenges in their study and application. EVs can be categorized into various subtypes based on factors such as size, density, biogenesis, and isolation methods. However, no distinct phenotype uniquely defines each subtype because of overlapping characteristics, including size, marker expression, composition, and function[160, 167]. The methods used to isolate EVs significantly influence their characterization and biomarker identification, making this a crucial challenge for both research and clinical applications. Currently, there is no universally standardized protocol for obtaining pure EV populations, as the selection of an isolation technique depends on the intended downstream analysis and application. Various approaches are available, including serial ultracentrifugation, size exclusion chromatography, ultrafiltration, density-gradient centrifugation, and immunoprecipitation or affinity capture[168] (Fig. 6).

EV classification relies on 1) biogenesis, differentiating ectosomes formed via plasma membrane budding from exosomes originating of the endosomal membranes and fuse via multivesicular body transport with the plasma membrane, 2) size, divided into large EVs (~200 nm to 5 µm), including microvesicles, exophers and apoptotic bodies and small EVs (~50 to 200 nm) and 3) content and function such as mitovesicles, oncosomes and migrasomes[160, 167, 169] (Fig. 5). Surface marker proteins are often used to narrow the vesicle type, including tetraspanins (CD9, CD63, CD81), tumor-susceptibility gene 101 (TSG101) and ESCRT related proteins[170]. Due to these heterogenous characteristic of EVs, classification and nomenclature continue to evolve.

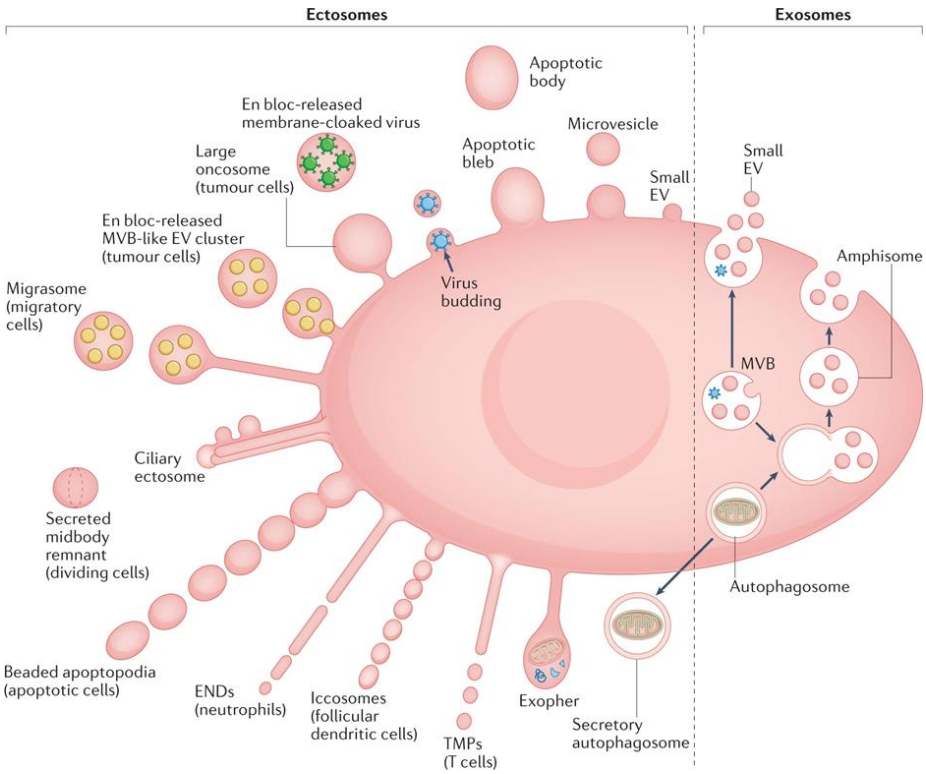

Figure 5: Heterogeneity of extracellular vesicles. Illustration from E.I. Buzas 2020, Nature reviews immunology.

1.5.1 Urinary EVs

Urinary extracellular vesicles (uEVs) are heterogeneous, as they are released from different cells of the urogenital tract, with EVs of renal, prostate and bladder origin are the main contributors[168]. Recently it was shown, that the kidney is the predominant source of uEVs, as confirmed by studies comparing uEV composition with in vitro models of kidney cells and mass spectrometry analysis of nephrostomy versus bladder-derived uEVs. Omics studies further revealed that 99.96% of uEV proteins originate from the apical side of the urogenital tract, with only a small fraction derived from infiltrating or contaminating cells[171-174].

Markers expressed by uEVs reflect their origin across different urogenital tract segments. Early research identified aquaporins (AQP1, AQP2), ion transporters (NKCC2, NHE3, NCC)[168, 175, 176], cubilin, megalin, and aminopeptidase, confirming proximal tubular origins, while nephrin, podocalyxin, and podocin indicate glomerular and podocyte contributions[177, 178]. Urinary EVs derived from the bladder and prostate have also been characterized, along with regenerative markers like Klotho, CD133, and SSEA4[179-181].

EVs provide a direct reflection of cellular activity, making them promising diagnostic and prognostic markers, as demonstrated in diabetic nephropathy, where Wilms tumor 1 (WT1) levels in urinary exosomes serve as indicators of disease progression[159].

In urine samples, uromodulin and albumin can interfere with uEV separation and characterization, particularly in proteomics and RNA sequencing. Patients with nephrotic-range proteinuria present challenges in EV detection due to high urinary protein levels, requiring specialized isolation methods[168, 182]. To address these limitations, several isolation techniques, e.g., dialysis, ultrafiltration, size exclusion chromatography, differential and density gradient ultracentrifugation, immunoprecipitation and analysis methods such as nanoparticle tracking analysis, flow-cytometry, electron microscopy and immune-blot have to be combined to allow uEV characterization (Fig. 6)[183] .

For accurate uEV quantification, normalization is required to correct for urine concentration variability. The most appropriate method is normalization to urine creatinine levels, similar to the albumin-to-creatinine ratio[170, 182, 184]. In general, urinary EVs secreted by nephron-lining cells, offer valuable insights into kidney function and disease.

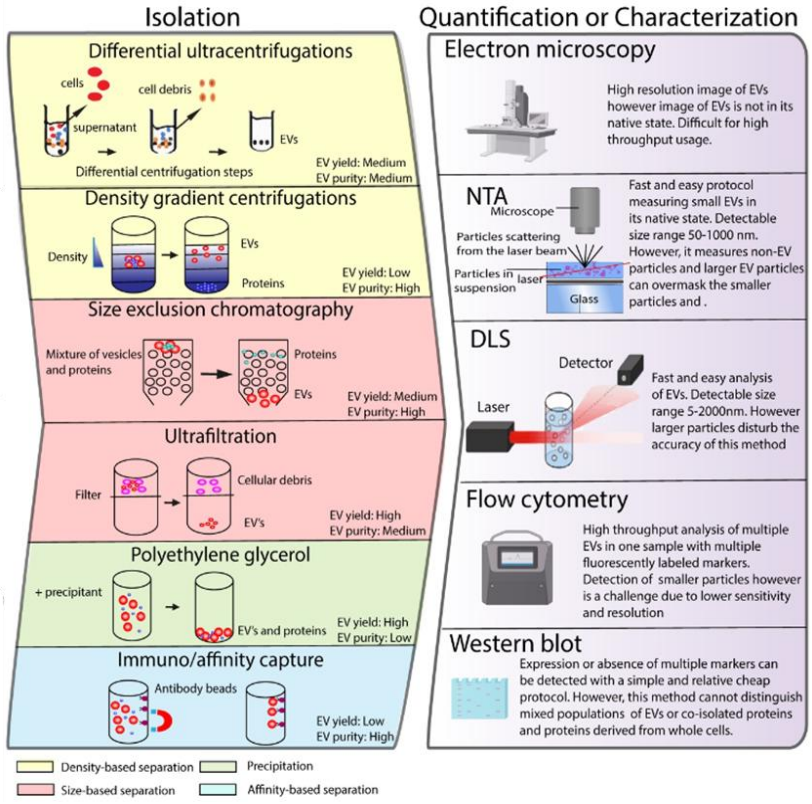

Figure 6: Extracellular vesicle isolation methods and quantification techniques. Abbreviations: NTA (Nanoparticle Tracking Analysis), DLS (Dynamic Light Scattering). Illustration from M. J. Lorenowicz et al. 2020, Theranostics.

1.5.2 Exophers

Exophers are a novel EV subtype, which are formed by budding out from the cell plasma membrane into the extracellular space[185, 186]. Exophergenesis was first observed in *Caenorhabditis elegans*, in which neurons under proteotoxic stress expel large membrane-bound vesicles[185]. Exophergenesis has been identified as critical process in protein and organelle clearance to counteract the issues of misfolded proteins and mitochondrial dysfunction in stressed neurons, as cells rely on mechanisms such as chaperone activity, protein degradation, autophagy, and mitophagy to maintain cellular homeostasis[185, 187].

These exophers contain aggregated proteins, damaged mitochondria, and other cellular debris. Exopher production increases when proteostasis is disrupted, such as impaired autophagy, chaperone suppression, or proteasome impairment. Notably, neurons that produce exophers maintain better function compared to those that do not, suggesting a neuroprotective role[185, 187, 188]. Once extruded, exophers are processed by surrounding tissues. In *C. elegans*, exophers enter the hypodermis, where their contents are either degraded or distributed to other cells[188]. This suggests that exopher-mediated clearance extends beyond simple waste removal and may involve intercellular material transfer. Similar exopher-like structures have been identified in murine cardiomyocytes, where they expel mitochondria that are subsequently processed by cardiac macrophages[189]. Additionally, both human and mouse neurons exhibit exopher production, indicating evolutionary conservation of this mechanism.

Beyond neuronal function, exophergenesis also plays a role in muscle cells. In *C. elegans*, body wall muscle (BWM) cells produce exophers in response to developing embryos within the uterus[190].

At a molecular level, exopher production is regulated by conserved cellular pathways. Components involved in phagocytosis, including CED-1, CED-6, and CED-7, participate in exopher processing[185, 188, 190]. Additionally, intermediate filaments, dynein motors, and microtubule integrity influence aggregate collection and exopher extrusion[191]. The autophagy protein ATG-16.2 and the BH3-only protein EGL-1 have also been implicated in promoting exophergenesis, linking it to broader stress response pathways[192, 193]. The involvement of EGL-1 suggests a link between exophergenesis and mitochondrial dynamics, with potential implications for neurodegenerative disease treatment. Interestingly, exopher production shares similarities with apoptosis, including membrane blebbing and mitochondrial fragmentation, but occurs without caspase activation, distinguishing it from programmed cell death[193].

In conclusion, exophergenesis represents a fundamental yet previously unrecognized branch of cellular homeostasis control while mechanical stress, oxidative stress, and mitochondrial dysfunction have all been shown to enhance exopher formation. It serves as both a neuroprotective mechanism and a transgenerational resource management system. Its conservation across species suggests it may play a crucial role in cellular homeostasis and disease prevention. Future research should focus on elucidating the precise molecular mechanisms underlying exopher production.

2 Aim

This study aims to determine whether podocyte-derived urinary extracellular vesicles (p-uEVs), specifically exopher-like vesicles (ELVs), serve as biomarkers of proteostatic disturbances in membranous nephropathy. Motivated by the critical role of proteostasis dysregulation in podocyte injury, the objective is to elucidate their role and utilization in immune complex clearance, oxidative stress adaptation, and podocyte homeostasis. By correlating urinary p-uEV content with glomerular proteostasis markers in experimental models and patient samples, this research seeks to identify disease-specific vesiculation patterns and their relevance to podocytes' ability to handle immune complexes in membranous nephropathy pathophysiology. Additionally, the study explores the diagnostic and prognostic potential of urinary ELVs as a non-invasive tool for monitoring disease progression and therapy response.

3 Materials and Methods

3.1 Materials

3.1.1 Appliances

Table 1: Appliances

Appliance	Type	Company
Analytic scale	510	Kern
Cell culture hood		ThermoScientific
Centrifuges	5417R 5804 R Heraeus Multifuge	Eppendorf AG Eppendorf AG Heraeus
COBAS		Roche
Confocal Microscope	LSM 800 airyscan1 LSM 980 airyscan2 Nikon A1 R LSM	Carl Zeiss AG Carl Zeiss AG Nikon Instruments
Critical point dryer	CPD 030	Bal-Tec
Electron-transmission microscope	TEM Leo 910 TEM Jeol 1400plus	Carl Zeiss Carl Zeiss
Gel electrophoresis chamber	MiniProtean Tetra Vertical Cell Criterion Vertical Cell	BioRad Laboratories
HPLC system	Ultimate 3000 RSLC	Universal scientific
Imager	Amersham ImageQuant 800	Cytiva
Imaging flow cytometer	Amnis® ImageStream$^{®X}$ MkII	Cytek
Incubator	BB15 CO_2	ThermoScientific
Light microscope	Axiovert 25 Leica DMi8 M/C/A inverse Nanolive 3D Cell Explorer-fluo Visitron-SD-TIRF with SoRa unit	Carl Zeiss Leica Microsystems Nanolive SA Yokogawa
Magnetic particle collector	DynaMag^{TM}-2	Invitrogen AG
Magnetic stirrer	RCT digital	IKA
Mass spectrometer	Orbitrap ExplorisTM	Thermo Fisher
Microplate spectrophotometer	EL808 Ultra	BIO-TEK Instruments

Multichannel pipette	S8	Brand GmbH&Co KG
Nanoparticle Tracking Analyzer	LM10 unit	NanoSight
pH-meter	PHS-3CB	Want
Pipettes	0.5-10 µl 2-20 µl 20-200 µl 100-1000 µl	Eppendorf AG
Pipet controller	Accu-jet	Brand
Platform shaker	Rocky GRS	Labortechnik Froebel
Power supply	PowerPac Universal	BioRad Laboratories
Precision scale	AC100	Mettler Toledo
Roller shaker	SRT6D	Stuart
Rotor ultracentrifuge	TLA-55 Type70Ti	Beckman coulter
Scanning electron microscope	SEM Jeol 7500F	JEOL
Sputter coater	SCD 500	Bal-Tec
Steam cooker	FS10	Braun GmbH
Thermomix	Thermomixer 1.5 ml Thermomixer 2.0 ml	Eppendorf AG
Trans Blot system	Trans-Blot turbo	BioRad Laboratories
Ultracentrifuges	Optima MAX-TL LE80K	Beckman coulter
Vibratom	VT1000S	Leica Biosystems
Vortex	Vortex Genie 2	Scientific industries
Waterbath		GFL, Gesellschaft für Labortechnik

3.1.2 Software

Table 2: Software

Software	Company
Axiovision	Zeiss
Fiji	Open source program based on ImageJ

+PEMP macro +TrackMate v7 plugin	
g:Profiler version 0.0.2	ELIXIR
GraphPad Prism	GraphPad Software
HiD® Histo Digital reconstruction	Chimaera
IDEAS	Amnis/Cytek
Illustrator	Adobe
ImageJ	Wayne Rasband
Imaris 8.2.1	Oxford instruments
KC Junior	BioTek Instruments
Meta-Morph version 7.10.5.476	Molecular Devices
Microsoft office	Microsoft
NTA 3.0 software	Nanosight
Photoshop	Adobe
R version 4.3.0	GNU General Public License
Spectronaut 18.6	Biognosys
STEVE v1.6.3496	Nanolive SA
ZEN 3.0	Zeiss

3.1.3 Consumable materials

Table 3: Consumable material

Material	Catalogue number	Company
6 well Plates	83.3920	Sarstedt AG & Co. KG
96 well Plates	82.1581	Sarstedt AG & Co. KG
96 well Plates High-bind	82.1581.200	Sarstedt AG & Co. KG
Cell strainer 100 µm	833945100	Sarstedt AG & Co. KG
Centrifuge tubes 15 ml 50 ml	 62.554.502 62.547.254	Sarstedt AG & Co. KG
SUPER PAP PEN Liquid Blocker	N71310-N	Science Services
Dialysis membrane Spectra/Por® Biotech CE MWCO 100 000, 16 mm	8967.1	Carl Roth
DynaBeads ™ M-450 Tosylactivated	14013	Invitrogen ThermoFisher

Extra Thick Blot Filter Paper, Precut, 8.6 x 13.5 cm	1703967	BioRad Laboratories
Filter Unit 5 µm Millex-SV	SLSV025LS	MerckMillipore
FluoroDish glass bottom	FD35-100	World Precision Instruments
Gelloader pipette tips	70.1190100	Sarstedt AG & Co. KG
Gloves (Nitrile)	SAP150993	Dermagrip
Gradient gels: <u>4-15 % Mini-Protean TGX Precast Gels:</u> 10 well stainfree 12 well stainfree 15 well stainfree <u>4-15% Criterion TGX Stain-Free Gel:</u> 18 Well 26 Well	 4568083 4568085 4561086 5678044 5678085	BioRad Laboratories
Microscope cover glasses round Microscope high precision coverslip	DKR1 DHR1	A. Hartenstein GmbH
Microscope slides	1000200	Paul Marienfeld GmbH & Co. KG
Microscope slides superfrost	03-0060	R. Langenbrick GmbH
Nanosep® Centrifugal Devices with Omega™ Membrane 300K	OD300C34	Pall
Parafilm M Sealing Film	HS234526B	Heathrow Scientific
Petri dishes	821472	Sarstedt AG & Co. KG
Pipette tips 1000 µl 200 µl 10 µl	 70.3050 70.3030 70.3010.100	Sarstedt AG & Co. KG
Polystrene magnetic particles	PM-40-10	Spherotech
PVDF Immobilon-P membrane	IPVH00010	Sigma
Reaction tubes 0.5 ml 1.5 ml 2.0 ml	 72.699 72.690.001 72.691	Sarstedt AG & Co. KG

SafeSeal tube, 1.5 ml, Protein Low Binding	72.706.600	Sarstedt AG & Co. KG
Scalpels	5518091	B.Braun
SEC qEV original 70 nm columns	SP1109823	IZON
Sera-Mag Magnetic particles	16437655	Fisher Scientific
Serological Pipettes 2 ml 5 ml 10 ml 25 ml	 86.1252.001 86.1253.001 86.1254.001 86.1685.001	Sarstedt AG & Co. KG
Syringe 1 ml Syringe 2 ml Syringe 50 ml	300928 8728844F-06	B. Braun
TC-flask T75 standard TC-flask T75 standard filter cap	83.3911 83.3911.002	Sarstedt AG & Co. KG
Ultracentrifugation tubes 1.5 ml Polypropylene Tube with Snap-on Cap, 11 x 39mm	357448	Beckman Coulter GmbH
Ultracentrifugation tubes 26.3 ml, Polycarbonate Bottle, 25 x 89 mm with Cap Assembly	355618	Beckman Coulter GmbH
Ultrafiltration tubes Amicon Ultra-15, PLHK Ultracel-PL Membran, 100 kDa	UFC910024	Merck millipore

3.1.4 Chemicals and kits

Table 4: Chemicals and kits

Chemical/Kit	Catalogue number	Company
Acetic acid	6755.1	Carl Roth
Acetonitrile	100030	Merck Millipore
Bortezomib PS-341	F1200	UBPBio
Bovine serum albumin	A7906	Sigma-Aldrich
Bromphenol blue	11844788	Chemsolute
Bruprenorphine (TEMGESIC)	ind00979	Indivior Europe
Calcium chloride	CN93.1	Carl Roth
Calyculin A	BML-EI192	Enzo
Citraconic acid	2604	Sigma-Aldrich
Cold water fish skin gelatine	G7041	Sigma-Aldrich
Coomassie brilliant blue G-250	1.15444	Sigma-Aldrich

Cozy XL Prestained protein standard	11850790	HighQu
Collagenase from C. histolyticum	C9891-1G	Sigma-Aldrich
Creatinin Jaffe	114444	Hengler Analytik
DAKO antigen retrieval solution	S2367	DAKO
Dithiotreitol	D9779-5G	Sigma-Aldrich
DMSO	4720.2	Carl Roth
DNase I from bovine pancreas	10104159001	Roche
Dulbecco´s Modified Eagle Medium	41965-039	ThermoFisher
Dulbecco´s Phosphat Buffered Saline	14190-144	Gibco
EDTA	E4884	Sigma-Aldrich
EGTA	3054.2	Carl Roth
Elisa gt anti mouse albumin antibody	A90-134A	Bethyl Laboratories
Epoxomicin	BML-PI127-0100	Enzo
Ethanol	2273.2500	Chemsolute
Ethylenglycole	6881.1	Carl Roth
Fetal Bovine Serum Fetal Bovine Serum exosome depleted	10500064 A2720803	ThermoFisher Gibco
Fluormount-G	0100-01	Southern Biotech
Formaldehyde	F8775	Sigma-Aldrich
Glutaraldehyde	354400	Sigma-Aldrich
Glycerol	G5516	Sigma-Aldrich
Glycine	3908.2	Carl Roth
Gum arabic	4159.3	Carl Roth
Hank`s Balanced Salt Solution (HBSS)	14170-138	Gibco
HEPES	9105.3	Carl Roth
Hoechst	62249	ThermoFisher
Horse serum	VEC-S-2000	Vector
Isofluran	HDG9623	Baxter
Isotonic sodium chloride solution 0.9%	SAP 150090	B. Braun
JetPEI	101000053	Polyplus
Micro BCA Protein Assay Kit	23235	ThermoFisher
Milk powder	T145.5	Carl Roth

ß-Mercaptoethanol	31350-010	Gibcp
Neufuchsin	72200	Sigma-Aldrich
Normal goat serum	NS02L	Sigma-Aldrich
Osmium tetroxide	419494	Merck
Paraformaldehyde	15710	Electron Microscopy Sciences
Penicillin-Streptomycin	15070063	Gibco
Phosphoric acid	6366.1	Carl Roth
PhosSTOP™	4906845001	Sigma-Aldrich
PMSF	P7626-5G	Sigma-Aldrich
Poly-L-lysine	P2636	Sigma-Aldrich
Polyvinylpyrrolidone	4607.1	Carl Roth
Ponceau	33427.01	Serva
Propylene oxid	10487920	Fisher Scientific
Protease XXIV	8038	Sigma-Aldrich
RotiQuant	0120.1	Carl Roth
RPMI medium	61870044	Gibco
SCALEVIEW A2	193-18455	FUJIFILM Wako Chemicals
SDS	20765.03	Serva
SigmaFast Protease Inhibitor	S8830	Sigma-Aldrich
Sodium azid	S2002	Sigma-Aldrich
Sodium chloride	1367.5000	Chemsolute
Sodium fluorid	S-1504	Sigma-Aldrich
Sodium phosphate	S-9763	Sigma-Aldrich
Sodium orthovanadate	S6508	Sigma-Aldrich
Suc-LLVY-AMC	4011369	Bachem
Sucrose	9097.1	Carl Roth
SuperBlock™ Blocking Buffer	37535	ThermoScientific
SuperSignal™ West Femto Maximum Sensitivity Substrate	34095	ThermoScientific
SuperSignal™ West Pico PLUS Luminol/Enhancer Solution	34578	ThermoScientific
TMB Elisa Peroxidase substrate	OORA01684	aviva systems biology
TPer	78510	ThermoFisher
Trifluoroacetic acid	6957.3	Carl Roth
Tris (Trizma Base)	T1503	Sigma-Aldrich

Triton X-100	T8787	Sigma-Aldrich
Tween 20	P1379	Sigma-Aldrich
Urea	U5128	Sigma-Aldrich
Xylol	8080.2500	J.T. Baker
ZytoChem-Plus AP Polymer Kit	POLAP-100	Zytomed systems

3.1.5 Buffers

Table 5: Buffers and composition

Buffer	Composition
Binding buffer 1	0.05 M carbonate-bicarbonate pH 9.6
Binding buffer 2	2 mM EDTA in filtered PBS with a pH of 7.4
Blocking buffer 1	50 mM Tris, 0.14 M NaCl, 1% BSA pH 8.0
Blocking buffer 2	5% normal horse serum in PBS with 0.05% TritonX-100
Blocking buffer 3	filtered PBS containing 2% cold water fish gelatine and SuperBlock™ in a 1:1 ratio
Blocking reagent solution (BRS)	mixing 100 ml of phosphate-buffered saline (PBS), 0.8% (w/v) of bovine serum albumin (BSA), 0.1625% (w/v) of sodium acid and 2% cold water fish skin gelatin
Bouin`s solution	0.2 M PB buffer, 0.044 M picric acid, 5% (V/V) acidic acid and 10% (V/V) formaldehyde in aqua dest
Cryoprotection solution	0.1 M PB (pH 7.4), 30% ethylenglycol 30% sucrose and 1% polyvinylpyrrolidone
Elution buffer	0.1M glycine in PBS pH of 3.5
Fixation solution	0.2 M PB, 0.15% Bouin`s solution, 4% PFA, 0.08% glutaraldehyde
Loading buffer reducing (5x)	250 mM Tris-HCl pH 6.8, 10% SDS, 0,5 M DTT, 50% glycerol, 0.25% bromophenol blue
Loading buffer non-reducing (5x)	250 mM Tris-HCl pH 6.8, 10% SDS, 50% glycerol, 0.25% bromophenol blue
Migration buffer	0.25 M Tris base, 1.92 M glycine, 1% SDS, pH 8.3

Neutralization buffer	0.1M Tris and pH 8.0
PB-Buffer	100 mM phosphate in ddH_2O pH 7.4
Preservation solution 1	660 mM NaN_3, 200 mM EGTA in ddH_2O
Preservation solution 2	100 mM PMSF in 100% ethanol
Proteinase Inhibitor Cocktail	1 mM sodium fluoride, 1 mM sodium orthovanadate, 100 nM Calyculin A, and 1x SigmaFast EDTA-free
TBS-T	10 mM Tris pH 7.4, 100 mM NaCl, and 0.05% Tween20
Transfer buffer	0.192 M glycine, 25 mM Tris base, 20% EtOH
Urea buffer	8 M Urea, 10 mM DTT in 50 mM Tris, pH 8,0
Wash buffer 1	50 mM Tris, 0.14 M NaCl, and 0.05% Tween-20 pH 8.0
Wash buffer 2	0.1M sodium phosphate buffer pH 8
Wash buffer 3	2% exosome-depleted FCS in filtered PBS
Sample buffer	50 mM Tris, 0.14 M NaCl, 1% BSA and 0.05% Tween-20 pH 8.0
Staining buffer	PBS with 8% exosome-depleted FCS

3.1.6 Antibodies and dyes

Table 6: Antibodies and dyes

Antibody/dye	clone/ catalogue number	company	IF/IHC	WB	IS	iEM	PD	*In vitro*	*In vivo*
rb anti-THSD7A	#HPA000923	Atlas	1:200, 1:400	1:1000	1:50				
hu anti-THSD7A	reference[194]	self-made		1:1000		1:20		1:100	
rb anti-THSD7A	reference[139]	self-made						1:200	
ms anti-THSD7A mAb	reference[195]	self-made	1:50						

control rabbit IgG	#I5006	Sigma							1:200
ms anti-myc	#sc-41	Santa Cruz		1:1000					
rb anti-PLA_2R1	#HPA012657	Thermo Fisher	1:200	1:1000	1:50				
gp anti-Nephrin	#GP-N2	Progen	1:200	1:2000	1:50				
rb anti-α-Actinin 4	#0042-05 clone IG-701	Immuno Globe	1:200	1:1000	1:50				
gt anti-Annexin A1	#AF3770	R&D Systems	1:400	1:1000					
rb anti-Annexin A1	ab214486	Abcam		1:2000					
APC anti-Annexin A1	#BLD640912	Novus Biologicals			1:10				
CoraLight Plus 647 anti-Annexin V	#CL647-66245	Protein Tech			1:10				
Pacific Blue anti-CD63	#BLD-353011/353012	BioLegend			1:50				
Pacific Blue anti-CD81	#BLD-349516	BioLegend			1:50				
ms anti-Flotillin	#610821	BD Bioscience		1:1000					

rb anti-14-3-3 AF546	#Sc-1657 AF546 pan 14-3-3-H8	Santa Cruz			1:50				
rb anti-14-3-3	# Sc-1657 Pan 14-3-3 H8	Santa Cruz		1:1000					
ms anti-β-actin	#A5441 clone AC-15	Sigma		1:5000					
cy2-dk anti-human IgG	#709-225-149	Jackson ImmunoResearch Laboratories	1:100						
rb anti-phospho-Paxillin	#44722G	Thermo Fisher	1:100						
cy5 rb anti-rabbit IgG	#711-175-152	Jackson ImmunoResearch Laboratories	1:200		1:200				
cy2-dk anti-human IgG	#709-225-149	Jackson ImmunoResearch Laboratories	1:200		1:200				
CoraLite® 488 anti-human IgG4	#CL488-66408	Protein Tech	1:100		1:50				
ms anti-human IgG4	#9190-01	Southern-Biotech							

ms anti-human IgG4	#9200-09	Southern-Biotech	1:4000						
gt anti-human IgG	#209-005-088	Jackson ImmunoResearch Laboratories	1:7500						
12 nm Colloidal Gold AffiniPure™ Goat Anti-Human IgG (H+L) (EM Grade)	#109-205-088	Jackson ImmunoResearch				1:10			
12 nm Colloidal Gold AffiniPure™ Donkey Anti-Rabbit IgG (H+L) (EM Grade	#711-205-152	Jackson ImmunoResearch				1:50			
rhodamine-wheat germ agglutinin (WGA)	#RL-1022	Vector	1:400				1:20		

biotin-WGA	#B-1025-5	Vector	1:400						
AF647-streptavidin	#S21374	Molecular Probes	1:200						
rb anti-C1q	A0136	Dako	1:200						
rb anti-Podocin	#P0372	Sigma		1:1000	1:10				
rb anti-Mitofusin-2	#9482	Cell Signaling	1:200	1:1000	1:50				
rb anti-MnSOD	#06-984	Millipore	1:100						
ms anti-ATPB	#ab14730	Abcam		1:1000					
rb anti-C5b9	#M0777	Dako	1:100						
rb anti-C5b9	#ab55811	abcam		1:1000					
gt anti-Cathepsin B	#PA5-47975	Invitrogen	1:200						
ms anti-Glepp1	#MABS1221	Millipore	1:200				1:20		
rb anti-LAMP2	#L0668	Sigma		1:1000					
rb anti-LIMP2		Paul Saftig, CAU Kiel, Germany	1:500	1:1000	1:50				
rb anti-α2	#2455S	Cell Signaling		1:1000					
ms anti-α3	#sc-166205	Santa Cruz		1:1000					
rb anti-CD63	#ab216130	Abcam		1:1000					

rb anti-CD9	#ab92726	Abcam		1:1000					
rb anti-GFP	#ab2090	Abcam	1:400	1:1000					
rb anti-k48pUB	#05-1308	Millipore		1:1000	1:50				
rb anti-k48pUB	#ab140601	Abcam	1:300						
rb anti-LMP7	#ab3329	Abcam		1:1000					
rb anti-LMP7		Elke Krüger, Greifswald	1:300	1:5000					
gp anti-nephrin	#GP-N2	Progen	1:200	1:1000					
gt anti-8-oxo-guanidine	#ab10802	Abcam	1:300						
rb anti-p57		Santa Cruz	1:400						
ch anti-tdTomato	#ORB182397	BiOrbit	1:300	1:1000					
rb anti-TSG101	#ab125011	Abcam	1:100	1:1000					
rb anti-ubiquitin	#NB300-129	Novus	1:300	1:1000					
rb anti-UCH-L1	#ab27053	Abcam		1:1000					
rat anti-UCH-L1 mAb	reference[196]	self-made	1:50	1:250					
MemBrite® Fix Cell Surface	#30096	Biotium			1x				

dye 594/615									
MitoSOX™	#M36008	Invitrogen	10µM		10µM				
LysoView™ 488	#77067	Biotium	1:20		1:20				
Periodic-acid-Schiff reagent	#1.08033.0500	Sigma							
Hematoxylin	#24420.02	Serva							
Hoechst 33342	#H3570	Thermo Fisher	1:1000						

Abbreviations: *IS* = ImageStream®; *IF* = immunofluorescence; *WB* = immunoblot; *iEM* = Immunogold EM; *PD* = Pulldown; *A* = application; *rb* = rabbit, *ms* = mouse; *gt* = goat; *ha* = hamster; *gp* = guinea-pig; *dk* = donkey, *mAb* = monoclonal antibody

All secondary antibodies used were either biotinylated, HRP- gold-, or fluorescent dye-conjugated affinity purified donkey antibodies (Jackson ImmunoResearch).

3.2 Methods

3.2.1 Cell culture

3.2.1.1 HEK cell transfection

HEK293T cells (Sigma, # 12022001) were cultivated in DMEM supplemented with 10% FCS and 1X penicillin/streptomycin at 37°C and 5% CO_2 in vented uncoated tissue culture flasks. JetPEI was used to perform transient transfection of HEK293T cells with full length human huTHSD7A or huPLA$_2$R1[197] constructs, according to the manufacturer instructions. In brief, 5 µg of the respective plasmid DNA was combined with 10 µl of JetPEI and 10 mM sodium chloride in a final volume of 500 µl. Following an incubation period of 25 minutes at room temperature, the mixture was gently added to HEK293T cells that were seeded at the same

day of transfection. The protein was permitted to be expressed by the cells for a period of 48 hours at 37 °C and 5% CO_2.

3.2.1.2 Generation of HEK cell THSD7A and PLA_2R1 protein lysates

The proteins generated by the HEK cells were isolated for protein analysis by immunoblot, in order to detect autoantibodies against huTHSD7A or huPLA_2R1 in murine sera or in the eluted antibody fraction from enriched patient exopher-like vesicles. The transfected HEK cells were harvested by scraping with a cell scraper in ice cold PBS. The resulting cell suspension was transferred to a 1.5 ml tube, centrifuged at 900 x g for 10 min at 4 °C, and the supernatant was discarded. In order to eliminate any remaining medium residues, the pellet was resuspended in PBS, centrifuged once more at 4 °C at 900 x g for 10 min. The supernatant was discarded, and the pellet lysed in T-PER with Proteinase Inhibitor Cocktail and PhosStop. After the protein was quantified using the ROTI®Quant universal assay in accordance with the instructions provided by the manufacturer, 10 µg of total protein was prepared for immunoblotting under non-reducing conditions (5x non-reducing loading buffer).

3.2.1.3 HEK cell cultivation for EV collection

For the purpose of collecting extracellular vesicles, HEK293T cells were cultivated after thawing in DMEM with 10% FCS in uncoated, vented cell culture flask at 37 °C and 5% CO_2 for at least 2 days. The medium of the cultured cells was aspirated and the cells were washed three times with PBS and then further cultured in an exosome-depleted medium (DMEM + 5 % exosome depleted FCS). After ~30 hours, the medium was collected and further processed in order to isolate the EV, as explained in more detail below.

3.2.2 Human sample collection

The study presented here is in accordance with all applicable ethical regulations. Human studies had received ethical approval, and similar samples are not available for access by external users. Approval from the ethics committee and written consent from the patients were also obtained 1) specifically for the analysis of the urine and correlations to the diagnostic biopsy samples (ethical approval #2023-101080-BO-ff) and 2) in order to generate human glomerular extract, the healthy (tumor-free) part of the kidney that was not required for pathological diagnosis was utilized. Patients were required to submit written agreement before

samples may be used for research purposes. As patients were anonymised, no information regarding their age or gender is accessible.

3.2.3 Animal experiments

Male BALB/c mice purchased from Charles River were of a pure genetic background. *Gt(ROSA)26Sortm4(ACTB-tdTomato,-EGFP)Luo/J x hNPHS2Cre* mice (*mT*/*mG*)[198] with a BALB/c background were obtained from the Huber laboratory (III Medical Clinic, UKE, Hamburg-Eppendorf). Membrane-bound green fluorescent protein (GFP) is expressed in podocytes of *mT*/*mG* reporter mice, while membrane-bound tomato is expressed in all other renal cells. All analyses were carried out on mice aged 12-20 weeks. Animals stayed in a pathogen-free animal facility at the University Medical Center Hamburg-Eppendorf. They were housed with unrestricted access to water and standard animal food (Altromin 1328 P), and were synchronized to a light-dark cycle lasting for 12:12 hours. In the present study, THSD7A$^+$-MN was induced in male BALB/c or *mT*/*mG* mice through intravenous injection of 180 µl (1.5 mg/ 30 g mouse) of rabbit anti-THSD7A antibodies or unspecific rabbit IgG as control. After 3 days, animals develop proteinuria, which approaches nephrotic ranges after seven days.
For the purpose of analyzing the effect of proteasomal inhibition on vesicle formation inhibitor analysis were conducted, mice were treated therapeutically with the proteasomal inhibitor epoxomicin (0.5 mg/kg bodyweight in 125 µl) or with vehicle (25% DMSO in 125 µl PBS) which were administered via intra-peritoneal injections for a period of four consecutive days starting on day 7 after MN induction. For analgesia purposes, mice were administered subcutaneously buprenorphine hydrochloride (0.1 mg/kg bodyweight, TEMGESIC) 30 minutes before 3.5% isoflurane inhalation narcosis to collect organs. Finally, animals were sacrificed by cervical dislocation. The body temperature was maintained at 37 °C ± 0.5 °C during all procedures. All experimental approaches were carried out in accordance with the guidelines established by the Behörde für Justiz und Verbraucherschutz, Amt für Verbraucherschutz, Lebensmittelsicherheit, and Veterinärwesen in Hamburg, Germany.

3.2.3.1 Murine sample collection

For urine collection, mice were injected subcutaneous with 1 ml isotonic 0.9% NaCl solution before placing them in metabolic cages over a period of 4 hours. If possible, repeated collection of urine was always carried out at the same time of the day, mainly in the evening. The urine was collected from the metabolic cage, transferred in a 1.5 ml tube and centrifuged for 10 min at 5000 g and 4 °C. The supernatant was transferred into a new 1.5 ml tube.

The collection of blood and kidneys was performed after isoflurane anesthesia (in detail refer to “Animal experiments”). First, blood from the aorta was taken with a syringe and transferred to a 1.5 ml tube. After this, kidney packages were removed carefully from the mouse leaving the aorta and muscles still attached and intact. Isolated kidney packages were thoroughly perfused through the renal arteries with 5 ml PBS/Dynabeads™ M-450 Tosylactivated/200 µl of Polystyrene Magnetic Particles per kidney to remove blood components such as unbound immunoglobulins from the renal circulation and to separate glomeruli from the rest by using a magnet, and separate the glomeruli with magnetic particles stuck in the small capillaries within the glomerulus only. Successful perfusion was controlled by proper discoloration of the kidney. Samples were either stored at -80°C prior to further analysis, fixed in 4% PFA for histological evaluations, or processed for glomerular isolation. For EM evaluations mice kidneys were perfused *in vivo* (see detailed descriptions of every method below).

3.2.3.2 Mouse serum analysis

In order to separate blood cells from serum, mouse blood was centrifuged for 10 minutes at 1500 g, 4 °C. In accordance with the instructions provided by the manufacturer, serum albumin amount was determined using a commercially available ELISA system (for further information see “Urinary albumin to creatinine ratio”). A COBAS system was utilized for the purpose of performing automated measurements in order to ascertain the levels of serum triglycerides, cholesterol and blood urea nitrogen (BUN).

Through the use of immunoblotting, specific rabbit THSD7A antibodies that were circulating in the serum were identified. For this purpose, non-reduced lysates of the huTHSD7A and as negative control huPLA$_2$R1 proteins that were generated in HEK cells were put on an SDS-PAGE. To identify the presence of rbTHSD7A abs, 300 µl of mouse serum was combined with SuperBlockTM in a ratio of 1:2. The mixture was incubated as primary antibody on the Western blot membrane over night at a temperature of 4°C and detected with anti-mouse HRP as secondary antibody.

3.2.3.3 Urinary albumin to creatinine ratio

Quantification of albumin content in the urine was performed using an ELISA system that is available for commercial use in accordance with the instructions provided by the manufacturer. To provide a brief overview, goat anti-mouse albumin antibodies were coated in a dilution of 1:100 to high-binding 96-well plates in binding buffer and allowed to incubate overnight at 4 °C. Once the plates had been washed three times in wash buffer, and blocked for 30 minutes at

room temperature with blocking buffer 1, the plates were washed again three times with wash buffer. Standards and urine were diluted in sample buffer and incubated at room temperature for 60 minutes. After three times washing, the secondary antibody, a horseradish peroxidase goat anti-mouse albumin at a concentration of 1:40,000, was applied and allowed to bind at room temperature for 60 minutes. The plates were washed five times with wash buffer and 100 µl of the enzyme TMB substrate provided with the kit was added. The plates were incubated for approximately 5 minutes in the dark. The reaction was stopped by adding 50 µl phosphoric acid per well. The extinction was measured using an ELISA plate reader at a wavelength of 450 nm. The concentration of albumin in the urine was determined by using the formula for absorption, which is as follows: absorption = (A - D)/1 + (x/C)B + D, where A and D are values from the standard curve. Calculations were made to determine the regression values for the standard curve in order to evaluate the precision of the values that were measured. Standard curves with r values greater than 0.9950, were utilized. Urinary albumin values were standardized to the urine creatinine values of the same individuals, determined by either the Jaffé method or calculated against the urine volume and the results were plotted as [mg albumin / mg creatinine] or as [mg albumin / µl urine] respectively.

3.2.4 Glomeruli isolation

Murine glomeruli: As described in Takemoto *et al.* murine glomeruli were isolated by performing Dynabead perfusion[199]. Briefly, the kidneys were perfused with a magnetic bead solution containing 50 µl of Dynabeads™; M-450 Tosylactivated and 200 µl of Polystyrene Magnetic Particles diluted in 50 ml of HBSS. The capsule was removed from the perfused kidneys and they were roughly shredded with a scalpel. The kidney pieces were divided into two 2 ml tubes and further digested with a mixture of collagenase in HBSS (1.2 mg/ml collagenase) and 100 U/ml DNaseI for 15 minutes at 37 °C and 1,300 rpm in a thermomix. Using a 2 ml syringe pestle, kidney homogenate was passed through a 100 µm cell strainer set on a 50 ml tube and washed with 10 ml HBSS. The second digested kidney was strained the same way over a new 100 µm filter into the same 50 ml tube and rinsed with 10 ml HBSS. The solution in the tube was then strained through a new 100 µm filter in a new 50 ml tube, and the filter rinsed again with 10 ml HBSS. The solution was centrifuged for 5 minutes at 600 g at 4 °C. The supernatant was discarded and the pellet was resuspended in 6 ml HBSS, divided in four 2 ml tubes, which were placed on a magnetic particle concentrator (MPC) to separate the glomeruli from the tubuli. After putting the tubes on the MPC, it was placed on ice and incubated for a duration of five minutes. Following the removal of the supernatant, the pellets were resuspended in 1.5 ml of HBSS with 0.05% BSA, and the samples were again

incubated on the MPC for 5 minutes. This procedure was repeated twice. Following the third wash, isolated glomeruli of the same mouse were combined in one tube as follows: after addition of 1 ml of HBSS to the first tube, the glomeruli were resuspended and transferred to the next sample tube. This process continued until all glomeruli of the same sample were collected in the last tube in a total volume of 1 ml. To determine the degree of contamination with tubuli, a phase contrast microscope was used count the number of tubuli and isolated glomeruli in 10 µl of the sample. The glomeruli were pelleted by centrifugation for 10 minutes at 1500 g and 4 °C, the supernatant was discarded, the glomeruli pellet shock frozen in dry ice and stored at -80 °C.

Human glomeruli: For immunoblots, human glomeruli were used as positive controls. In order to prepare an extract of human glomeruli, healthy sections of kidney taken from individuals who had undergone nephrectomy were utilized. Following the separation of the cortex from the medulla, the kidney cortex was weighed and shredded using a scalpel, approximately 0.5 g of tissue were distributed into each tube A digestion solution consisting of 1.2 mg/ml Collagenase 1 A and 100 U/ml DNaseI was added to each reaction tube. In a ThermoMixer, digestion was carried out for 15 minutes at 37 °C and 1,300 rpm. After passing the tissue homogenate through a 212 µm sieve that was put on a beaker, the tissue homogenate was pushed through the sieve using a tiny Erlenmeyer flask and low pressure. PBS containing 0.05% BSA was used to rinse the sieve several times in between each tissue sample. To further separate glomeruli from tubular remnants, the glomeruli solution was added to a sieve with a mesh size of 53 µm. This ensured that whole glomeruli were retained on the sieve, while tubuli are supposed to pass the sieve. In order to flush the glomeruli from the sieve into a new beaker, the sieve was flushed with high pressure applied with a syringe loaded with PBS that contained 0.05% BSA. In order to enhance the purity level of the glomerular isolate, the last step was repeated twice, each time employing a clean 52 µm sieve. The obtained suspension was centrifuged for 10 minutes at a speed of 800 g at 4 °C. The supernatant was decantated, and the pellet was resuspended in a solution of PBS with 0.05% BSA. The number of isolated glomeruli as well as their purity was determined under a phase contrast microscope.

3.2.5 Morphological analyses

Cleared kidney slices: Cleared kidney slices were obtained by immersion fixed kidney pieces from *mT/mG* mice with 4% PFA overnight at 4 °C. The kidneys were then sliced with a Vibratome to a thickness of 300 µm. After that, the slices were washed with PBS and optically cleared for a period of 48 hours using SCALEVIEW A2. Immunofluorescence of exopher-like vesicles was performed by incubating cleared slices with cy5 anti-rabbit IgG at a concentration

of 1:100 for three days. A thorough washing process for 48 hours was followed by the acquisition of 3-dimensional image stacks with a Nikon A1 R confocal laser scanning microscope equipped with a 60x CFI Plan Apo Lambda immersion oil objective (NA 1.42). Furthermore, a Visitron Spinning Disk Microscope was employed, which was fitted with a 100x CFI Plan Apo Lambda (NA 1.45) objective. Additionally, a Yokogawa CSU W-1 Spinning Disk unit was utilized, which had 50 µm pinholes and a Photometrics Prime 95B (back-illuminated sCMOS camera). In order to visualize the mGFP and cy5 tags, solid-state lasers with wavelengths of 488, 640, and 647 nm were used. Image stacks were acquired using Z-steps of 0.130 and 0.150 µm, respectively. The deconvolution of the 3-dimensional images was accomplished with Nikon's NIS-elements AR 5.42.02 by employing a theoretical PSF and utilizing an automatic deconvolution algorithm. After that, additional processing was performed on the 3D image data sets by using the tools provided by Nikon Denoise.ai and Clarify.ai. The use of NIS-elements allowed for the visualization of both the 3-dimensional volume views of the entire glomerulus as well as the 2-dimensional MIPs derived from the podocyte cell body region. With the help of Imaris 8.2.1, a 3-dimensional reconstruction of the picture stacks was created using the blend mode, starting from the podocyte cell body area. In order to provide the best possible representation, the brightness, contrast, and gamma were edited.

Light microscopy: The general renal morphology in the THSD7A^{+}-MN patient biopsy was evaluated by light microscope. Thereby, 1.5 µm thick paraffin sections were stained with periodic-acid-Schiff reagent in accordance to manufacturer instructions and the nuclei were counterstained with Hematoxylin.

Immunohistochemical analyses: The diagnostic kidney biopsy of the THSD7A^{+}-MN patient was being cut into 1 µm paraffin sections which were deparaffinized and rehydrated. For THSD7A, antigen retrieval was achieved by boiling in DAKO antigen retrieval buffer, pH 9 for 15 minutes at 98°C, followed by cooling. Protease XXIV, with a concentration of 5 µg/ml was used to obtain huIgG4 and huIgG, incubated for 15 minutes at 37°C, and the reaction was terminated in 100% EtOH. After antigen retrieval nonspecific binding was blocked with blocking buffer 2 for 30 minutes at room temperature followed by incubation at 4°C overnight with rabbit anti-THSD7A, mouse anti-huIgG4, or goat anti-huIgG in blocking buffer. The staining was captured using the ZytochemPlus AP Polymer kit in accordance with the instructions provided by the manufacturer. Following the counterstaining of the nuclei with hematoxylin, the slices were mounted with gum arabic. Evaluation of stainings was performed with an Axioskop (Axiovert 25) and the Axiovision program.

Immunofluorescent analyses paraffin sections: Deparaffinization and rehydration were performed on the patient biopsies as well as on the mouse kidney paraffin sections. Antigen retrieval was accomplished by either 1) boiling the sample in DAKO retrieval buffer with a pH

of 9 or pH 6.1, or 0.05% citraconic acid for 30 minutes at a temperature of 98 °C, and then cooling it, or 2) by digesting the sample with protease XXIV for 15 minutes at 37 °C, and washing it in 100% ethanol. Blocking buffer 2 was used to prevent unspecific binding for a period of 30 minutes at room temperature. The primary antibodies were incubated overnight at 4 °C in blocking buffer 2. After washing the samples in PBS, fluorochrome-labeled donkey secondary antibodies (all 1:200, Jackson Immunoresearch Laboratories), biotinylated-WGA (followed by AF647-streptavidin), or rhodamine-coupled WGA, and Hoechst were applied to the samples for 30 minutes at room temperature. The sections were mounted with fluoromount after being washed with PBS.

Immunofluorescence of urinary exopher-like vesicles (ELVs): Using the ImageStream® antibodies in accordance to the procedure specified in the paragraph ImageStream®, urinary EVs were stained for qualitative EV characterisation. The staining panel was extended to include the proteins of interest to facilitate additional analysis of the ELV content (for a summary of the antibodies and dyes that were utilized, see table 6). Round cover slips were coated with poly-L-lysine (1:1000 in sterile water), incubated 1 hour at room temperature, washed three times for 5 minutes with PB buffer and air-dried for 15 minutes. Stained EVs were dried at 37 °C on the coated coverslips and mounted on slides using fluoromount. EVs were stained with MemBrite 594/615 as a general EV marker, and huIgG4-AF488 as well as 14-3-3-AF546 to demarcate them as ELVs in combination with the proteins of interest.

Immunofluorescence was analyzed using conventional and high-resolution confocal microscopy, specifically with an LSM800 equipped with Airyscan 1 or an LSM980 with Airyscan 2, utilizing ZEN 3.0 software, or with a Visitron-SD-TIRF microscope featuring a SoRa unit from Yokogawa for the assessment of foot process effacement.

3.2.5.1 Ultrastructural analyses

Pre-embedding Immunogold EM (conducted by Prof. Lars Fester, Neuranatomy, Bonn, Germany): For the investigation of immunogold labeling, experimental mice were fixed *in vivo* in accordance with the protocol described by Somogyi and Takagi (1982)[200]. Briefly, a transcardial perfusion with fixation solution was performed, after perfusion kidneys were removed and postfixed in 1 ml of 0.1 M PB buffer with 4% paraformaldehyde and 0.15% picric acid for 24 hours at 4 °C. Sections of fixed tissue were cut using a vibratome at a thickness of 60 µm. These sections were then placed into a cryoprotection solution for 24 hours. The cryoprotection solution was removed from the 60 µm thin slices in order to perform the pre-embedding immunogold staining. This was accomplished by washing the slices twice in 0.1 M PBS for a duration of 20 minutes. Subsequently, the slices were washed in 0.1 M PBS with

10% sucrose for 30 minutes, followed by additional 30 minutes in 0.1 M PBS with 20% sucrose. After transferring the tissue to a drop of PBS containing 20% sucrose, it was snap frozen with nitrogen and then allowed to defrost at room temperature. Following that, the tissue was washed three times in PBS at pH 7.4 for 10 minutes each time.

Jackson ImmunoResearch's 12 nm Colloidal Gold-AffiniPure Donkey anti-rabbit IgG (H+L) was utilized for the purpose of detecting bound rbTHSD7A-abs. Through the use of the affinity-purified, pathogenicity-inducing patient THSD7A autoantibody[194] as the primary antibody, indirect immunostaining was carried out for the purpose of detecting THSD7A antigen. This was done to avoid the possibility of cross-reactivity with the injected and bound rabbit THSD7A-abs as well as the intrinsic mouse IgG that was present in the sample. Jackson ImmunoResearch's 12 nm Colloidal Gold-AffiniPure Goat anti-human IgG (H+L) was then utilized to identify the bound patient THSD7A autoantibody. Blocking reaction was performed for 1 hour using blocking reagent solution (BRS) that was supplemented with 2% normal goat serum. This was done in order to enhance the specificity of the primary antibody reaction.

BRS was used to incubate the primary antibody over night at 4°C. Once the tissue had been treated for 24 hours, it was washed three times with PBS at a 5-minute interval. Then, it was incubated for 2 hours with a 1:50 solution of a 12 nm gold-conjugated antibody solution in BRS. Afterwards, the tissue was rinsed three times in PBS pH 7.4 for 5 minutes, and set aside to soak for 10 minutes in a 1% glutaraldehyde solution in 0.1 M PB. A solution of 1% OsO_4 in water was used to postfix the tissue at a temperature of 4 °C for 10 minutes. This was followed by dehydration in an ethanol series. After immersing the probes in propylene oxide twice for 5 minutes, they were left to remain in a 4:1 solution of epon and propylene oxide overnight. Finally, using a Reichert Jung Ultracut microtome, tissue samples were thinly sectioned and examined under a Zeiss electron microscope and TEM Jeol 1400plus. ImageSPViewer and the image viewer Jeol were used as assisting tools for taking pictures.

3D reconstruction (conducted by Dr. Desiree Loreth, UKE Hamburg, Germany): The HiD® Histodigital reconstruction approach[201] was used to create a three-dimensional model from 30 to 48 sequential electron micrographs. The first step was to use stiff image registration to standardize the orientation of the micrographs and align all of the images. Even with slice alignment, the thin pieces will not produce a consistent 3D image due to the non-linear deformations caused by cutting and subsequent processing. To fix these distortions and make the data set spatially coherent, the second step is to use an intensity-based non-rigid registration procedure. The Chimaera SDK was used to generate volume visualizations.

Scanning electron microscopy (SEM) (conducted by Prof. Lars Fester, Neuranatomy, Bonn, Germany): The 60 µm mouse kidney slices that had been bouin-fixed were subjected to a

series of ethanol/aqua dest baths with raising ethanol concentrations (30%, 50%, 70%, 90%, 100%) at 10 minute intervals. They were then immersed in an acetone/EtOH bath with increasing acetone concentrations (50%, 70%, 90%, 100%) at ten-minute intervals for evaluation in the scanning electron microscope. Tissue samples were subsequently vacuum-dried after being dried in a critical point dryer. Thereafter, they were placed on a carbon plate with conductive silver using a metallic probe holder. They were further dried in a vacuum chamber for another 24 hours. After applying a 5 nm layer of platinum using a sputter coater, the surface was examined using a scanning electron microscope (SEM) Jeol 7500F equipped with a YAG and a LABE backscatter electron detector (BSE).

3.2.6 Extracellular vesicle (EV) isolation

EV isolation from human embryonic kidney culture: After the cell culture medium was collected, preservation solution 1 and 2 were added in a dilution of 1:100 each. Following the centrifugation of the medium for 10 minutes at a speed of 1500 g and 4 °C, the supernatant was collected and centrifuged again for 10 minutes at 3000 g and 4 °C. A syringe filter with a pore size of 5 µm was used to filter the supernatant. Following the ultra-centrifugation of the filtered medium for 1.5 hours at a speed of 100,000 g at 4 °C, the supernatant was discarded, and the pellet was resolved in filtered PBS. EV concentration was measured by Nanoparticle Tracking analysis.

EV isolation from mouse urine: Urine samples were centrifuged for 10 minutes at 5000 g at 4 °C. The supernatant was collected and supplemented with the preservation solution 1 and 2 each in 1:100 dilutions. The Spectra/Por Biotech CE 100 kDa cut-off dialysis membrane was used to dialyze the urine for 20 hours at 4°C in 1 x PBS on a magnetic stirrer in order to decrease the protein quantity in the nephrotic urine. The dialyzed urine was then ultracentrifuged for 1.5 hours at 4°C and 100,000 g. The pellet was dissolved in filtered PBS after the supernatant was discarded. ImageStream® was used to assess the concentration of EVs by staining with the overall vesicle MemBrite® Fix Cell Surface dye 594/615.

EV isolation from patient urine: In general, a 24-hour urine or spot urine prior to the kidney biopsy was collected from nephrotic patients in the clinic. Two patients were prospectively followed, and urinary samples were collected at time of their routine clinical management. Control urine was collected as spot urine samples from healthy volunteers. In accordance with the instructions that were published and suggested by the MISEV[170, 202], urine was collected and processed in the following manner. The preservation solutions 1 and 2 were added to the urine in a dilution of 1:100 each. The urine was centrifuged for 10 minutes at 2500 g at 4 °C.

The supernatant was filtered using syringe filters with a pore size of 5 µm in order to completely eliminate cell debris. Before being used, aliquots of 50 ml were stored at -80 °C.

Urine samples that had been frozen were thawed overnight at 4 °C, then extensively vortexed and centrifuged for ten minutes at 2500 g at 4 °C to remove aggregates. In order to reduce the abundance of contaminating proteins that were present in the highly proteinuric urine, the urine was ultrafiltrated by centrifugation at 3000 g and 4 °C using 100 kDa cut-off filter tubes until half of the initial volume was reached. Thereafter, the filtered supernatant was ultracentrifuged for 1.5 hours at 4 °C and 100,000 g, the supernatant was discarded, and the EV pellet was dissolved in filtered PBS. ImageStream® analysis was used to determine the particle count per milliliter using MemBrite® Fix Cell Surface dye 594/615. From here on, the obtained EV samples are referred to as total urinary EVs (input). The general workflow for total urinary EV isolation and subsequent huIgG4^{+}-EV enrichment for the individual analyses (ImageStream®, immunofluorescence, immunoblotting, NTA, autoantibody elution, proteomics) is summarized in Fig. 7.

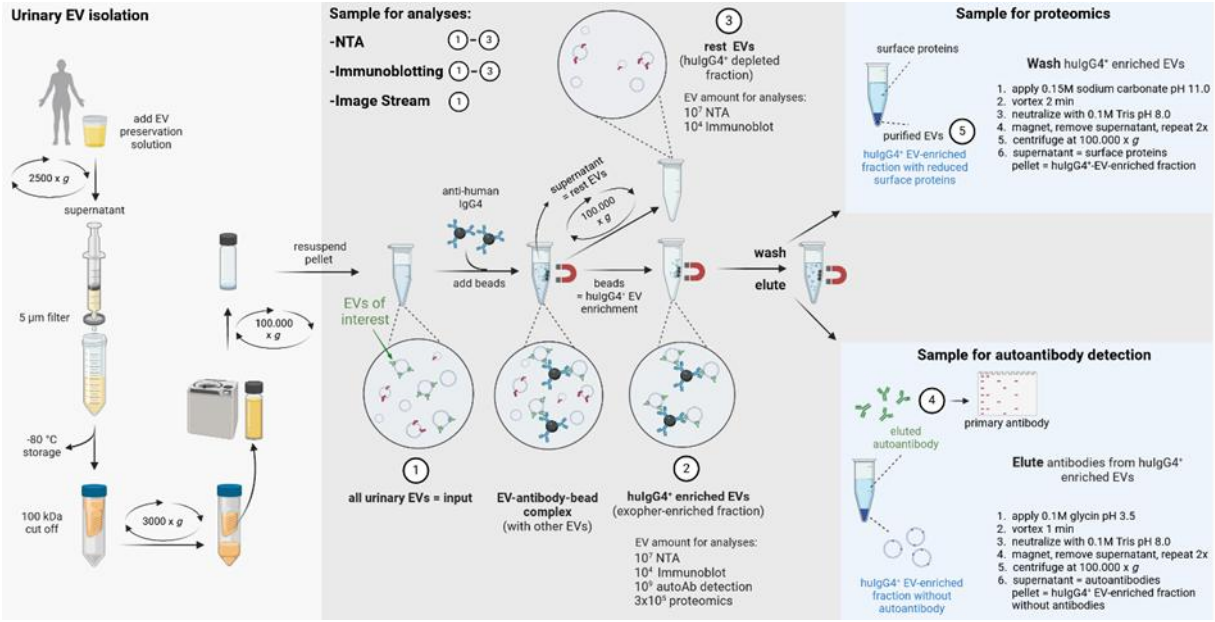

Figure 7: General workflow of human urinary EV isolation and huIgG4^{+}-EV enrichment for analyses. Scheme visualizes the procedures and generated EV samples as detailed in the methods. Created with Biorender.

3.2.6.1 GLEPP1^{+}-vesicle purification from total urinary and HEK cell derived EVs

Preparation of GLEPP1-beads for EV pulldown: After being washed with 0.1M sodium phosphate buffer pH 8 wash buffer 2 on a MPC, to exchange the storage buffer, Dynabeads™ M-450 Tosylactivated were ready for use. Dynabeads were covalently conjugated with anti-human Glepp1 antibody in accordance with the instructions provided by the manufacturer. Briefly, after washing twice with 0.1M sodium phosphate buffer with vortexing in between, 1 µg antibody per 20 µl beads was added (20 µl beads were used for one IP with 1x10^{9} EVs). The

mix of antibody and beads was filled up to 200 µl with wash buffer 2 and incubated for 36 hours at 4 °C on a roller shaker. The tube was put on the MPC, the supernatant was discarded and the beads carefully washed with wash buffer 2. Beads coupled to antibodies were then suspended in blocking buffer 3 and then blocked on a roller shaker for 1 hour at room temperature. Wash buffer 2 was used to rinse beads carefully on a MPC twice.

GLEPP1$^+$-EV pulldown: The initial material utilized for the experiment was 1x10^9 total EVs isolated from urine or produced by HEK cells. After adding total EVs to the prepared GLEPP1-beads, the beads were filled to a volume of 250 µl with binding buffer 2. The mixture was then incubated overnight on a roller shaker at 4 °C. The MPC was used to concentrate the EVs that were attached to the GLEPP1 beads. The supernatant, containing the unbound rest EVs was transferred to a new 1.5 ml tube. With strictly vortexing for a period of 2 minutes, the enriched GLEPP1$^+$-EVs that were bound to the beads, were eluted from the beads. To determine the EV concentration (in particles per milliliter), the ImageStream® device was utilized and MemBrite® Fix Cell Surface dye 594/615 stained EVs were measured. A SDS-PAGE was loaded with 2x10^4 GLEPP1$^+$ and HEK cell derived EVs in DTT reducing loading buffer and immunoblotting was performed.

3.2.6.2 Enrichment of huIgG4$^+$-EVs from total EVs

Preparation of huIgG4-beads for EV pulldown: After being rinsed with wash buffer 2 on a MPC, Dynabeads™ M-450 Tosylactivated were utilized for antibody coupling. Anti-human IgG4 antibodies were covalently coupled to Dynabeads in accordance with the instructions provided by the manufacturer. Briefly, after washing twice with wash buffer 2 with vortexing in between, 1 µg antibody per 20 µl beads were added (20 µl beads were used for one IP with 1x10^9 EVs). The mix of antibody and beads were filled up to 200 µl with wash buffer 2 and incubated for 36 hours at 4 °C on a roller shaker. The tube was put on the MPC, the supernatant was discarded and the beads carefully washed with wash buffer 2. Using a roller shaker, antibody-coupled beads were blocked in filtered PBS for one hour at room temperature using blocking buffer 3. In wash buffer 2, beads were carefully washed on an MPC for two times.

HuIgG4$^+$-EV pulldown: Depending on the intended assay different amounts of total EVs were utilized as starting material (sample 1, Fig. 7): 10^6 (immunoblotting), 10^9 (proteomic studies), 10^9 (ImageStream®, NTA), or 10^{10} (autoantibody elution) After adding isolated total EVs to the blocked huIgG4-beads, the bead / EV solution was filled up to a volume of 250 µl with binding buffer 2. The mixture was then incubated overnight on a roller shaker at 4 °C. An MPC was used to capture the EVs that were coupled to the huIgG4 beads. Following the removal of the supernatant that included the rest EV fraction (huIgG4$^+$-EV depleted; sample 3 in Fig. 7), the bead bound enriched huIgG4$^+$-EVs were eluted by thoroughly vortexing for 2 minutes in PBS

(which corresponds to sample 2 in Fig. 7). On the MPC the supernatant containing the huIgG4^{+}-EVs was transferred to a new tube and PBS was added and vortexed to uncouple remaining EVs. The rest and huIgG4^{+}- EVs were pelleted by ultracentrifugation for 1.5 hours at 4 °C at 100,000 g. The remaining EV pellet was dissolved in sterile PBS, and the concentration (in particles per milliliter) was determined using the ImageStream®.

3.2.6.3 Autoantibody elution from urinary patient vesicles

In order to elute autoantibodies from the huIgG4^{+}-bead-bound EVs (which correspond to sample 2 in Fig. 7) the beads with bound EVs were incubated for 2 minutes in 50 µl elution buffer. Thereafter, the beads were strongly vortexed for one minute and an equal volume of neutralizing buffer was added. A MPC was used to capture the beads, the supernatant, containing the EVs as well as the autoantibodies was collected. The beads were incubated again with elution buffer, vortexed and neutralized as before, in order to elute remaining EVs and autoantibodies. Both supernatants were combined. To isolate the EVs from the supernatant, the supernatant was ultracentrifuged for 1.5 hours at 100,000 g, 4 °C. The supernatant that included the previously eluted autoantibodies (which corresponds to sample 4 in Fig. 7) was saved for the use as a primary immunoblot antibodies.

3.2.7 ImageStream® analysis

The ImageStream® was used to analyze vesicle abundance and marker composition. Analysis was performed using total EVs isolated from 250 µl of mouse urine and 10^{9} EVs isolated from patient urine. To determine the particle/ml concentration of individual EV sample preparations, 3 µl of isolated total EVs were stained.

EV staining for ImageStream®: For analysis, EVs were incubated in staining buffer, Membrite594 (1x) and appropriate antibodies for 45 minutes in darkness at room temperature in a total volume of 10 µl.

With the usage of a 300 kDa filter, stained EVs were washed in 500 µl wash buffer 3. After centrifugation for 10 minutes at 5000 g, the EVs were resolved in a wash buffer 3. Different controls were included in all of the studies: (1) buffer controls without any EVs or antibodies, (2) EV samples without antibodies, and (3) buffer with antibodies only. Before being applied, each antibody (see table 6) was centrifuged for 10 minutes at 15000 g at 4 °C. Antibodies, as cy5 anti-rabbit, AF546 anti-14-3-3, CoraLite Plus 647 anti-AnnexinV, and 1x MemBrite ® Fix Cell Surface dye 594/615 were utilized for staining mouse EV samples. The following

antibodies were utilized for the labeling of human extracellular vesicles: CoraLite ® 488 anti-human IgG4, PacBlue anti-CD63, PacBlue anti-CD81, APC anti-AnnexinA1, CoraLite Plus 647 anti-AnnexinV, and 1x MemBrite® Fix Cell Surface dye 594/615.

ImageStream® measurements: Standard sheath fluid (Dulbecco's PBS pH 7.4) served as solvent for the EV analysis with an ImageStream®X MkII Analyses were carried out with a low flow rate and a 60x magnification. Channel 2 (480-560 nm filter) was used to detect mGFP, FITC, and cy2 emission signals, channel 3 (560-595 nm filter) for AF546 and mTomato signals, Channel 4 (595-640 nm filter) for MemBrite ® Fix Cell Surface dye 594/615, channel 7 (430-505 nm filter) for PacBlue and AF647, cy5, and APC signals were detected with channel 11 (640-745 nm filter). The detection of site scatter (SSC) was achieved through the use of channel 6 (745-800 nm), as brightfield channels 1 and 9 were used, with filters ranging from 430-480 nm and 570-595 nm, respectively.

Mouse EV gating: For *mT/mG* reporter mice, total vesicle population contained of all fluorescent EVs positive for mTomato (Ch03) and mGFP (Ch02). Gates were set to select either signals positive for mGFP (podocyte EVs), mTomato (all other EVs), and in addition, positive for both signals. An analysis was performed on either the $mGFP^+$ population or the $mTomato^+$ population to determine the presence of rbIgG (Ch11) and Annexin V (Ch11) signal ($mGFP^+$ population: Ch11 against Ch02). The $mTomato^+$ population (Ch03) was treated likewise.

For calculating total vesicle population in the urine of BALB/c mice, gating was set to only include MemBrite® 594/615 positive EVs. The fluorescence of Ch04 MemBrite594/615 was plotted against SSC Ch06. Every single event that exhibited a low SSC (less than 1000) but a fluorescence intensity for MemBrite594/615 was counted to the total EV population, which was used for subsequent studies. The $MemBrite594/615^+$ population was plotted for the markers rbIgG (cy5 Ch11) and 14-3-3 (AF546 Ch03).

Human EV gating: EVs that were positive for Ch04 MemBrite594/615 fluorescence were plotted against SSC Ch06. All events that showed low SSC (<1000) but a fluorescent intensity for MemBrite594/615 were used as total EVs ($MemBrite594^+$) for further analysis. The $MemBrite594^+$ population was further analyzed for additional markers. The marker huIgG4 in combination with 14-3-3, Annexin A1, Annexin V, and CD63/81 with uniform gates were plotted. Data analysis was performed using Amnis IDEAS software (version 6.2).

3.2.8 Nano particle tracking (NTA) analysis

An evaluation of the EV size distributions within the EV fractions was performed by NTA analysis. A total of 10^9 EVs each was used for the NTA measurment of patient EV samples (input, rest EVs, and huIgG4$^+$-EVs). To accomplish this, huIgG4$^+$-EVs were removed from huIgG4-beads by applying extensive vortexing for a period of three minutes, shortly centrifugal spin down, removing unbound beads at the MPC and collecting the supernatant as it contains the huIgG4$^+$-EVs. This procedure was repeated once more after adding 20 µl PBS to the beads. The eluted EVs were quantified at the ImageStream® via Membrite594 staining.
For NTA measurment, 10^9 EVs were diluted in a total amount of 1.5 ml PBS, and ~500 µl were injected into the sample chamber of an LM10 instrument provided by Nanosight. Screen gain was set to 2, and camera level to 15. These were the standard parameters for all the measurements. Five videos with a duration of 1 minute each were captured for each sample, and the temperature inside the chamber was controlled at 25 °C. The NTA 3.0 software was utilized to carry out the data analysis. For further analysis, the following software settings were used: detection threshold = 6, screen gain = 10. With this device a maximum particle size of 5 µm is detectable, larger particles were not included in the size distributation measurement.

3.2.9 Immunoblot

Immunoblots were performed with mouse and human glomerular lysates, human podocyte cell lysates as well as mouse and human patient urine EV lysates.

Patient urinary Glepp1$^+$-EVs: 2x10^4 enriched GLEPP1$^+$-EVs (see detailed pulldown description method above) were lysed in 10 µl PBS containing 2 µl 5x reducing loading buffer, the samples were incubated for 10 minutes at room temperature and loaded on an SDS-PAGE.

Human embryonic kidney cell culture EVs: 2x10^4 total EVs isolated from human embryonic kidney exosome-depleted medium were resuspended in 10 µl PBS. Subsequently, 2 µl of a 5x reducing loading buffer was added, samples were incubated for 10 minutes at room temperature and loaded for SDS-PAGE analyses.

Patient urinary huIgG4$^+$-EVs: 2x10^4 enriched huIgG4$^+$-EVs (see detailed pulldown description method above) were lysed in 10 µl PBS with 2 µl 5x reducing loading buffer, incubated for 10 minutes at room temperature and loaded for SDS-PAGE.

It is important to note that abundances of EV proteins that are obtained by immunoblotting are appropriate for qualitative findings ("protein xy is present"). Issues with normalization make it difficult to come up with quantitative findings, such as "protein xy is more abundant in sample A than in sample B", due to 1) Normalization to absolute EV number is problematic because

of the size variations of EV populations, which leads to different total protein abundances; 2) Normalization to protein content is problematic because BCA measurements are not reliable from the nephrotic urine despite all of the efforts that have been made to reduce albumin contamination; 3) Normalization to home keeper is hindered because there are not adequate and uniform EV home keepers within the various EV fractions.

Murine and human glomeruli: To separate the glomeruli into soluble and insoluble pellet, the glomeruli were lysed in two steps. The first step was to extract the soluble fraction, by adding 30 µl of T-Per containing protease inhibitor cocktail per 1000 glomeruli. A pestle was used to mechanically shred the glomeruli within the lysis buffer, and then the mixture was incubated for 30 minutes on ice with vortexing every 5 minutes. After centrifuging the lysed glomeruli for 30 minutes at 4 °C, 16000 g, the supernatant containing the soluble proteins was recovered. After lysing the remaining pellet in 30 µl per 1000 glomeruli urea buffer, the pellet was shredded again using a pestle, incubated for 30 minutes on ice with vortexing every 5 minutes. After that, the lysate was centrifuged for 30 minutes at 16000 g, 4°C, and the supernatant containing the insoluble proteins was collected. The soluble and insoluble fractions were denatured using 1x reducing loading buffer and incubated at 95 °C for 10 minutes. 6 µl of the soluble and insoluble fraction, which refers to 200 glomeruli, were loaded for SDS-PAGE and analyzed by immunoblot.

Human podocyte cell lysates: 10 µg protein were lysed under non-reducing conditions by adding 1x non-reducing loading buffer. Samples were incubated for 10 minutes at room temperature and loaded for SDS-PAGE analyses.

In general, samples were separated using a 4-15% MiniProtean TGX gel in migration buffer. The semi dry transfer of proteins was carried out in transfer buffer in a BioRad TransBlot Turbo System, to a PVDF membrane for 30 minutes at 25 mA. Immediately following the transfer, ponceau staining was performed to visualize all proteins. Therefore, the membrane was washed 2 minutes in ddH_2O after blotting and incubated in ponceau for 10 seconds to 5 minutes, depending on the signal intensity. The membrane was washed three times in ddH_2O and the signal was visualized at the ImageQuant800. The membrane was decolorized by washing with a TBS-T for 5 minutes, and subsequently blocked for 1 hour at room temperature with 5% nonfat milk in TBS-T. The membrane was washed three times with TBS-T for 5 minutes each before incubation with primary antibodies that were diluted in Superblock blocking reagent or 2.5% non-fat milk in TBS-T overnight on a shaker at 4 °C. The primary antibody solutions were discarded and the membrane was washed three times for 5 minutes each in TBS-T before and after incubation in HRP- coupled secondary antibody solutions (1:10000, 5% nonfat milk in TBS-T). Using either the Chemiluminescent Substrate West Pico Plus or the Chemiluminescent Substrate Femto Super Signal Maximum Sensitivity Substrate

for a 5 minute incubation, protein signal was visualized with the Amersham ImageQuant 800. ImageJ software was used to perform densitometric analysis. Protein signals were normalized to either ponceau, β-actin, or vesicular markers from the same membrane. When experiments involving multiple membranes, they were combined and an internal calculation of the relative changes to control was done. This calculation was performed within the same membrane. In the immunoblots shown, bands that belong to the same membrane are displayed. If this was not the case, fine dashed white lines indicate when bands where not enclosed to another on the membrane.

3.2.10 Proteomics of huIgG4^{+}-EVs

To isolate the huIgG4^{+}-EVs for proteomic analysis, the huIgG4^{+}-bead bound EVs (which correspond to sample 2 in Fig. 7) were washed with PB buffer and removed from the beads. Following the addition of 50 µl 0.15 M sodium carbonate pH 11, the mixture was incubated for 1 minute, vortexed for 2 minutes, and then neutralized with neutralize buffer. The supernatant containing the huIgG4^{+}-EVs was collected using an MPC, and the beads were incubated once more with 0.15 M sodium carbonate, pH 11.0. After this, the beads were vortexed and neutralized to remove any remaining EVs from the beads. The beads were collected on the MPC, and the supernatant containing the huIgG4^{+} enriched EV fraction was collected. The supernatant was ultracentrifuged for 1.5 hours at 100,000 g and 4 °C. The supernatant was removed and the EVs were ready for proteomics analysis (sample 5 in Fig. 7). Therefore, the EV pellets were lysed in 20 mM HEPES pH 8, with 1% (v/v) sodium dodecyl sulfate (SDS), vortexed and then incubated at 95 °C for 5 minutes. The samples were frozen in dry ice and stored at -80 °C.

The following proteomic sample processing, measurements and analyses were performed by Prof. Uwe Völker, Dr. Kristin Surmann and Dr. Stephan Michalik, Functional Genomics, Greifswald, Germany.

Samples were thawed at room temperature while shaking for 15 minutes at a speed of 1400 rpm to improve the extraction process. Following an incubation period of 5 minutes in an ultrasonication bath, the samples were centrifuged for 60 minutes at 17,000 g at room temperature. In order to determine the concentration of soluble proteins present in the supernatant, a BCA assay (Micro BCA Protein Assay Kit) was performed with bovine serum albumin serving as the standard. In order to establish a normalization standard, 550 ng of ^{15}N-labeled protein extract of *Bacillus subtilis* was added to 41.5 µl of each sample, which corresponded to 3x10^{5} EVs. The samples were then filled up with 20 mM HEPES, pH 8. Thereafter, disulfide boundaries were reduced for a period of 30 minutes in 2.5 mM DTT, and

free cysteine SH-groups were subsequently alkylated using 10 mM iodoacetamide for an additional 30 minutes in the dark. After that, 8 µl of a SeraMag bead mix containing 20 µg per µl was added to each sample to prepare protein extracts for tryptic digestion. The protein to trypsin ratio was 25:1, and the SP3 bead-based protocol[203] was applied. Following the termination of the trypsin reaction with 0.5% (v/v) trifluoric acid and the separation of peptides from the beads through the use of a magnet and centrifugation, the peptides were analyzed by performing a nanoLC-MS/MS utilizing an Orbitrap ExplorisTM mass spectrometer coupled to an Ultimate 3000 RSLC. By applying a solvent gradient ranging from 0% to 100% acetonitrile in 0.1% acetic acid, the separation of peptides from a 1 µl peptide solution (which corresponds to peptides of $1.23x10^4$ EVs) was effectively achieved. The mass spectrometry data were obtained in a data independent mode.

The Spectronaut 18.6 software was chosen to carry out the data analysis. Initially, a spectrum library was derived from a sample set that included the fractions of exopher-like vesicles in the four urine samples. This was accomplished by comparing the sample set to a Uniprot database that was restricted to human entries (2022). We used the following parameter settings: tryptic digestion (trypsin/P; 7-52aa), up to two missed-cleavages were permitted, carbamidomethylation at cysteine was designated as a fixed condition, and oxidation at methionine was classified as a variable condition. After that, the library was utilized to compare spectra with each pellet and supernatant fraction that was present in each urine sample. Furthermore, an existing *B. subtilis* ^{15}N spectral collection was made available for investigation. Statistical analysis was done with R version 4.3.0. For additional processing, the Spectronaut ion report was imported into R. A median normalization was performed on the ions with regard to the sample-specific *B. subtilis* spike-in signal for each sample. In order to calculate the iBAQ protein intensity, only the normalized ions that had a Q-value that was lower than 0.001 were given consideration and only proteins that had a Q-value that was lower than 0.001 and had at least two peptides were taken into account for this calculation. After that, the iBAQ values that were obtained were filtered so that only the unique protein groups were kept.

Following the completion of this procedure, the gProfiler analysis was carried out using the final list of proteins that were found in each sample. The gprofiler2 program[204] (version 0.2.2) was utilized in order to execute this investigation. The g:SCS multiple testing correction approach was applied, and the significance threshold was set to 0.05. The tools tidyverse[205] (v2.0.0), ggtext[206] (v0.1.2), glue[207] (v1.7.0), and ggh4x[208] (v0.2.6) helped in order to facilitate the generation of plots.

The final data includes identified proteins and linked pathways according to Gene Ontology[209]. Raw data and the spectral library have been deposited to the ProteomeXchange Consortium via the PRIDE partner repository with the dataset identifier PXD049008. The account details for the PRIDE repository are:

Username: reviewer_pxd049008@ebi.ac.uk
Password: pQXHqNCm.

3.2.11 Statistical analysis

If it is not explicitly indicated differently, the black line in point clouds represents the mean, and the results were expressed as mean ± standard error of the mean (SEM). A significance level of *p < 0.05 was defined. For the purpose of comparing the means in a time course, a two-way ANOVA was performed using Prism 8.2.1 for Windows, which was developed by GraphPad Software and is available on their website at www.graphpad.com. In order to make comparisons between animal experiments, the one-way ANOVA with Dunn's post-test for multiple comparisons was used. The p value is used in conjunction with Spearman's correlation analysis to determine whether or not the observed correlation is statistically significant or if it may have been the result of random chance. This is a test of the null hypothesis, which states that there is no association between the two variables that are being tested compared to one another. When the p value is less than 0.05, it indicates that there is a statistically significant probability that the observed correlation occurred by chance. Comparative analysis was performed using the Mann-Whitney U test on animal experiments that consisted of only two groups. The repetitions that were utilized were biological replicates, and the measurements were taken out of different samples obtained from independent experiments. A blind assignment was made to each of the experimental groups, and all of the mice were littermates.

4 Results

4.1 Isolation and abundance of urinary EVs

Membranous nephropathy is characterized by podocyte stress and disruptions in protein homeostasis, including UPS upregulation and dysfunction, which contribute to podocyte injury and disease progression[45]. Urinary extracellular vesicles have emerged as valuable biomarkers for kidney disease, providing a non-invasive means to assess cellular changes in the renal system. Given the potential of EVs as biomarkers and the critical role of the UPS in maintaining podocyte function, the first aim of this study was to investigate whether EV abundance and UPS-related proteostatic disturbances in MN are reflected in urinary EVs. The presence of UPS components in uEVs may offer insights into podocyte injury mechanisms and disease tracking.

4.1.1 Small and large extracellular vesicles can be isolated from human and mouse urine and contain ubiquitin-proteasome system proteins

Extracellular vesicles present in biofluids such as urine can be categorized based on their size and the expression of specific marker proteins such as TSG101 and Annexin A1[168, 169]. First, the purity of the EV isolation method was ensured. Urinary EVs from healthy human donors and BALB/c wildtyp mice were isolated using a combination of 100K (100,000 g) ultracentrifugation and size-exclusion chromatography. The integrity and morphology of these vesicles were then assessed via electron microscopy, revealing the presence of vesicles of various sizes with minimal visible debris (Fig. 8A). To further classify these vesicles, human and mouse uEVs were fractionated into large EVs (lEVs) and small EVs (sEVs) through differential ultracentrifugation. Nanoparticle tracking analysis confirmed that the size distributions of lEVs and sEVs were comparable between human and murine samples, reinforcing the consistency of the fractionation approach (Fig. 8B).

In a next step, the presence of established EV markers as well as the presence of ubiquitin-proteasome system components within these fractions was analyzed. Immunoblotting confirmed the enrichment of key EV-associated proteins, including TSG101, Annexin A1, Flotillin, and CD9, within both lEV and sEV populations (Fig. 8D). Importantly, components of the ubiquitin-proteasome system were also identified in these vesicles. Immunoblotting revealed the presence of polyubiquitinated proteins, K48-linked ubiquitinated proteasome substrates, and the deubiquitinating enzyme UCH-L1, equally abundant in lEVs and sEVs, suggesting that urinary EVs carry UPS-related proteins (Fig. 8D). To quantitatively assess the distribution of UPS components across the two EV populations, it was first confirmed that TSG101 served as a suitable loading control for both small and large EVs (Fig. 8C). Following

normalization to TSG101, it could be observed that the levels of polyubiquitinated proteins, K48-ubiquitinated substrates, and UCH-L1 were comparable between lEVs and sEVs from both human and murine urine samples (Fig. 8E). This suggests that UPS-related cargo is consistently packaged within EVs, regardless of vesicle size.

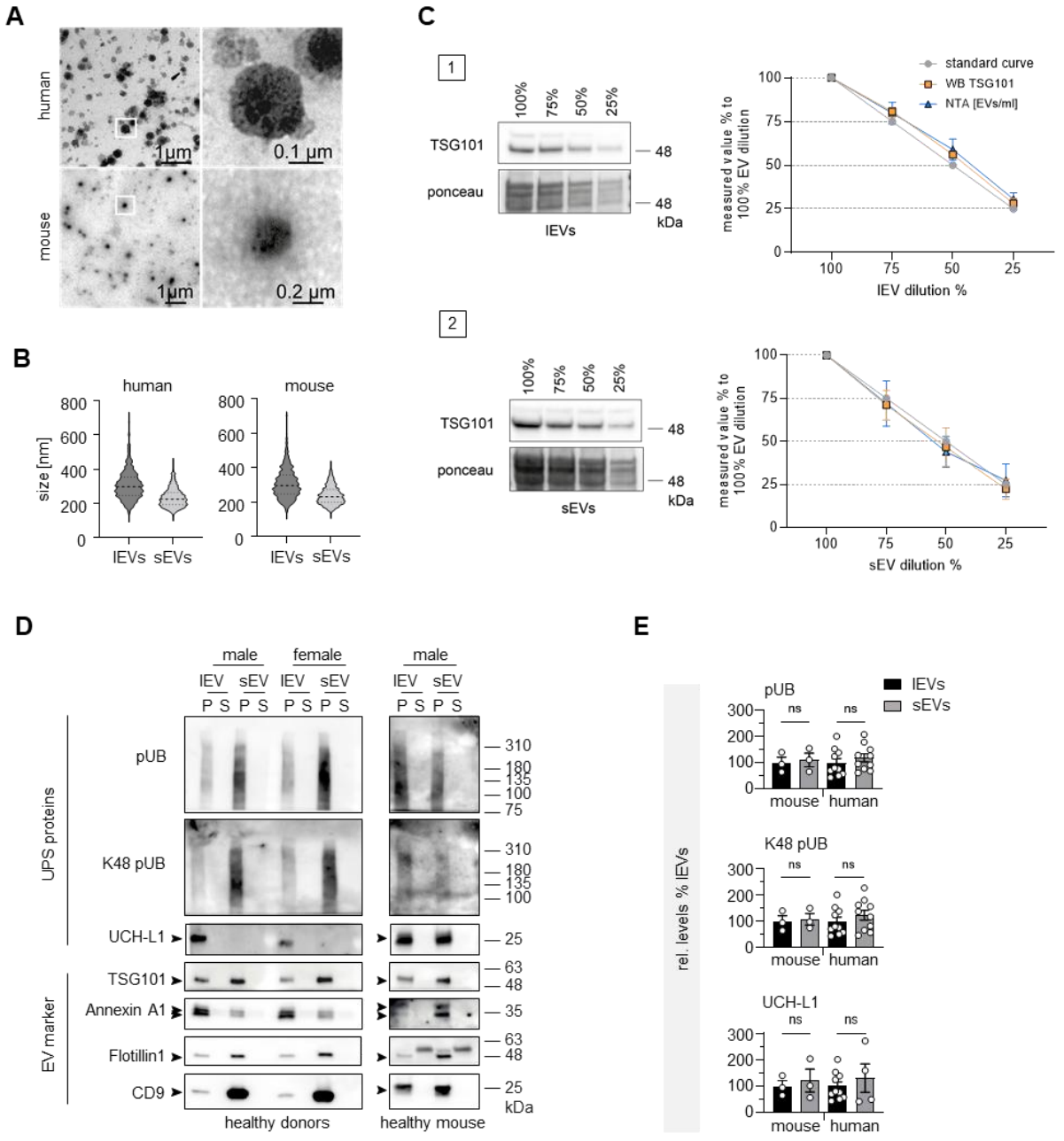

Figure 8: Large and small urinary EVs from human and mice contain UPS associated proteins. Urinary EVs from humans and mice were isolated and fractionated into large (lEVs) and small (sEVs) EVs using differential ultracentrifugation (sEVs at 100,000 g and lEVs at 16,000 g, respectively). **A)** Electron microscopy images of total isolated human and murine urinary EVs confirm the purity of the preparations. **B)** Nanoparticle tracking analysis (NTA) was used to assess EV size distribution in human and mouse urine. Violin plots represent the median, as well as the 25% and 75% percentiles. In humans, lEVs range from 45 to 779 nm (mean: 326 nm), while sEVs range from 51 to 446 nm (mean: 213 nm). Similarly, mouse lEVs range from 48 to 792 nm (mean: 309 nm), and sEVs range from 46 to 411 nm (mean: 206 nm). **C) Panel 1:** lEVs and **panel 2**: sEVs were diluted 75, 50 and 25% and loaded on an SDS-PAGE. Immunoblots show a serial dilution dependent TSG101 signal in large and small EVs. Ponceau staining was used as loading control. Concentration of the diluted EV samples were measured by nanoparticle tracking analysis (NTA). TSG101 immunoblot signal (orange, arbitrary unit) of undiluted and diluted EV samples as well as the NTA EV concentration per ml (light blue) were calculated to the undiluted value as 100% and plotted together with a hypothetical standard curve (grey). **D)** EVs were analyzed by immunoblotting for UPS-proteins and EV markers in healthy human and murine samples. "P" denotes the EV pellet, while "S" represents the urine supernatant. **E)** Quantification of UPS proteins normalized to TSG101 levels in mouse (N=3) and human (N=10) small EVs (grey) relative to large EVs (black, set at 100%), values are expressed as mean +/-SEM.

4.1.2 Tracking urinary EV alterations and morphological podocyte damage across podocyte injury mouse models

Podocyte *mT*/*mG* reporter mice, which express membrane-bound GFP (mGFP) specifically in podocytes and membrane-bound tdTomato in all other cells, were utilized to determine whether the quantity of uEV generation and secretion by podocytes differs in different podocyte injury settings. Cleared kidney sections of *mT/mG* mice showed the specific expression of GFP in podocytes and tdTomato in all other cells in the glomerulus. Therefore, these reporter mice were evaluated whether they enable a clear distinction between podocyte-derived (GFP^+) EVs and EVs originating from non-podocyte renal cells ($Tomato^+$). Confocal microscopy confirmed the ability to monitor podocyte-specific EV release into the urinary space in *mT/mG* mice and further validated the presence of GFP^+ EVs in both the small (sEV) and large (lEV) urinary EV fractions isolated from the transgenic mouse urine (Fig. 9A).

To investigate whether the type of podocyte injury differentially influences urinary EV secretion, various mouse models of podocyte damage were analyzed. These included the BTBR *ob/ob* model of type 2 diabetic nephropathy (DN) as a representative of metabolic podocyte injury, the Adriamycin (ADR) nephritis model to mimic toxic podocyte injury, and the THSD7A-associated membranous nephropathy (MN) model to reflect immune (autoantibody)-mediated podocyte injury. Each model captures distinct pathophysiological mechanisms leading to podocyte damage. The timelines for disease induction and sample collection for each model are summarized in Fig. 9B. In the metabolic injury model, urine samples were collected from BTBR *ob/ob* mice at 8, 12, and 18-20 weeks of age. Glomeruli were isolated from kidneys of mice sacrificed at week 18 or 20, respectively. For both, the toxic and antibody-mediated podocyte injury models, Adriamycin and THSD7A antibodies were administered on day 0, and the mice were sacrificed on day 12. Urine samples were collected one day prior to induction (untreated (UT)) and on days 1, 3, 6, 9, and 12 post-induction (Fig. 9B). All three models exhibited significant proteinuria, as measured by the albumin-to-creatinine ratio (ACR) in urine samples collected on the day of sacrifice, confirming the presence of podocyte dysfunction and kidney injury (Fig. 9C).

To assess morphological podocyte damage, the filtration slit density (FSD) using the podocyte exact morphology measurement procedure (PEMP) method[210] was used (Fig. 9D). In brief, kidney slices were stained for the slit diaphragm (SD) protein nephrin and analyzed by high-resolution microscopy. For analyzing the FSD, the capillary area within a glomerulus was encircled, the SD length within the encircled area was determined by the nephrin signal. The FSD values were then calculated from the ratio of SD length and capillary area. In the BTBR *ob/ob* model of DN, FSD remained unaltered, with nephrin meanders appearing comparable to those observed in control kidney slices of littermate control mice (Fig. 9D). However, in both the ADR model of toxic podocyte injury and the $THSD7A^+$-MN model of immune-mediated

injury, FSD was significantly decreased in comparison to their respective controls. Accordingly, high-resolution confocal microscopy of the nephrin pattern revealed broadening and disruption of nephrin meanders compared to control mice, indicating severe structural damage to the filtration barrier in these podocyte injury models (Fig. 9D). Given this, we next examined whether the observed alterations in FSD affected the abundance of cytoplasmic $TSG101^+$ vesicles within podocytes, as TSG101 serves as marker of a wide range of EV types and therefore TSG101 was used to normalize protein abundance in the EV analyses and its protein levels. High-resolution confocal microscopy confirmed that the presence of $TSG101^+$ vesicles remained consistent in podocyte across all three injury models. No observable differences were detected in the abundance of cytoplasmic $TSG101^+$ vesicles between control littermates and diseased mice, nor among the three distinct forms of podocyte injury, metabolic, toxic, or antibody-mediated, all of which were characterized by established proteinuria and the latter two also with an altered FSD (Fig. 9E).

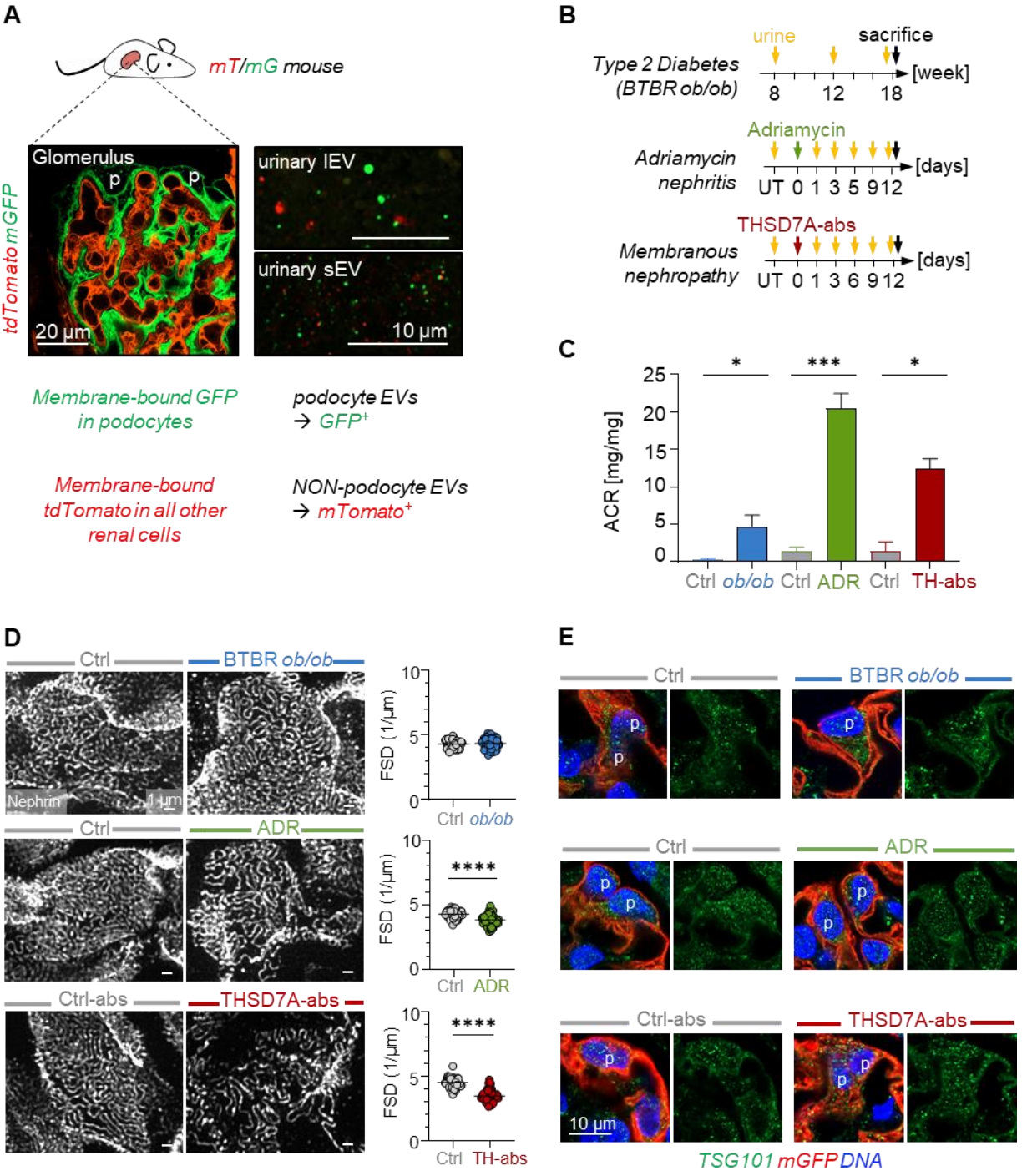

Figure 9: Tracking podocyte-derived urinary EV release and morphological changes in podocyte injury models. A) Confocal image of a representative cleared kidney section, and of isolated urinary vesicles derived from *mT/mG* reporter mice, which express membrane-bound GFP (green) specifically in podocytes and membrane-bound tdTomato (red) in all other cells, allowing the distinction between GFP$^+$(green) and Tomato$^+$(red) vesicles in large and small urinary EVs. **B)** Scheme of the experimental setup for examined podocyte injury models. **C)** Urinary Albumin-Creatinine Ratio (ACR, mg/mg) in different models: BTBR *ob/ob* mice (blue, weeks 18–20), adriamycin-induced injury (green, day 12), and THSD7A autoantibody-induced membranous nephropathy (red, day 12). ACR values for BTBR *ob/ob* data are pooled from two independent experiments (N = 7 per group), for ADR-treated mice pooled from two independent experiments (N > 9 per group), while THSD7A$^+$-MN mice represent pooled data from one experiment (N > 5 per group). **D)** Morphological analysis of injured podocytes. The **P**odocyte **E**xact **M**orphology Measurement **P**rocedure (PEMP) was used to assess filtration slit density (FSD) across the used podocyte injury models. Data represent pooled values from one experiment (N > 3 per group). **E)** Confocal analysis of kidney sections derived from all three mouse models, stained for TSG101 (green), mGFP (red) and DNA (blue). All data are presented as mean ± SEM; *p < 0.05, ***p < 0.001, ****p < 0.0001 (Mann-Whitney U-test).

4.1.3 Increased podocyte-derived EVs in THSD7A$^+$-MN

To investigate whether podocyte damage affects the quantity of podocyte-derived urinary large and small EV, both fractions were isolated from 18- and 20-week-old BTBR *ob/ob* mice in a volume adapted manner and GFP (podocyte-derived) and tdTomato (non-podocyte-derived) signals were assessed via immunoblotting. The relative abundance of podocyte-derived (GFP$^+$) uEVs to control was determined through densitometric analysis of the GFP-to-tdTomato ratio of each individual urine normalized to TSG101. Although 18- and 20 week-old BTBR *ob/ob* mice exhibiting an obesity, hyperglycemia, and albuminuria, the ratio of GFP to tdTomato in lEVs and sEVs did not significantly differ from that of control littermates (Fig. 10A). Additionally, no significant correlation was found between the relative GFP to tdTomato ratio and severity of proteinuria (albumin-to-creatinine ratio, ACR) (Fig. 10B), indicating that podocyte-specific uEV secretion was not significantly impacted in clinically manifested DN.
Similar findings were observed in the case of podocyte damage caused by adriamycin. During an observation period of 12 days, urine samples were taken on day 1, 3, 5, 9 and 12 after disease induction and isolated lEVs and sEVs were analyzed. Immunoblot signals for GFP and tdTomato were normalized to TSG101 and calculated as a percentage of untreated (UT) controls, shown on the left y-axis in the graphs (Fig. 10C). No significant increase in podocyte-derived EV secretion was observed over the 12-day observation period, despite a strong increase in ACR compared to control mice (right y-axis, orange line). Spearman correlation analysis did not show a relation between proteinuria and podocyte-derived EV release as can be appreciated in Fig. 10D. In contrast, the THSD7A antibody-mediated MN model displayed a marked increase in podocyte-derived EVs in both lEV and sEV populations over the 12-day disease course. EVs were processed and analyzed in the same manner as the samples from the ADR mice. The relative GFP to dtTomato ratio (plotted on the left y-axis in Fig. 10E) demonstrated a significant and progressive increase in podocyte-derived EV secretion. Notably, ACR (plotted in orange on the right y-axis) mirrored the increase in podocyte-derived EVs, suggesting a strong link between podocyte damage and vesicle release in the MN model. Further analysis confirmed a positive correlation between the relative GFP-to-tdTomato ratio and ACR in both lEV and sEV fractions (Fig. 10F). This indicates that in THSD7A$^+$-MN, podocyte injury leads to an active and progressive release of urinary EVs, with a tendency to larger EVs originating from podocytes, a phenomenon not observed in DN or ADR models.

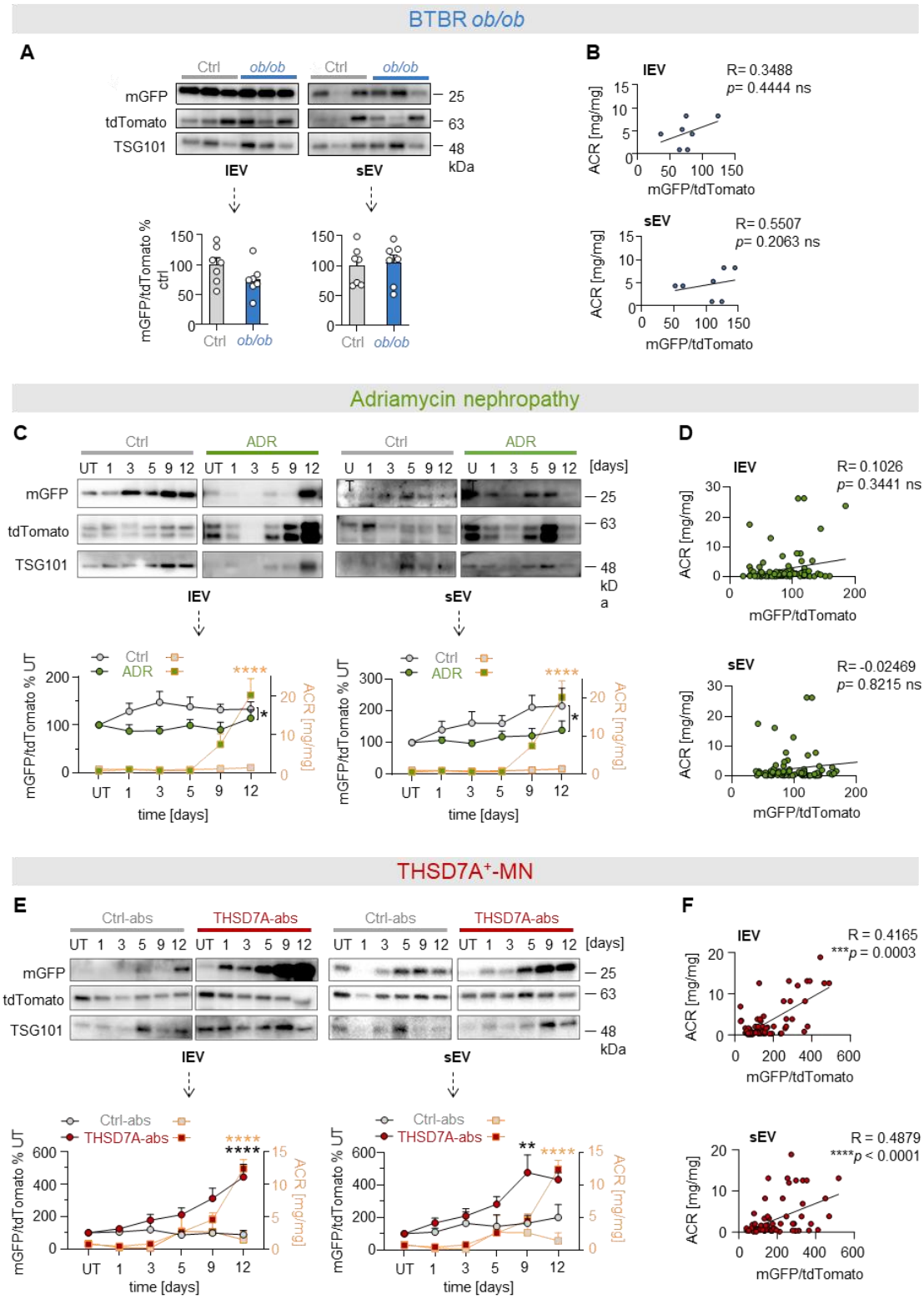

Figure 10: Podocyte-derived uEV abundance in different types of podocyte injury. A, C, E) Representive immunoblots of 2 × 10⁴ large and small uEVs analyzed for mGFP and tdTomato protein abundance in **A)** BTBR *ob/ob*, **C)** Adriamycin and **E)** THSD7A⁺-MN mice. Corresponding graphs show relative mGFP/tdTomato ratio, normalized to TSG101 levels, plotted on the left y-axis (round symbols), while corresponding ACR values are plotted on the right y-axis (square symbols). **B, D, F)** Spearman correlation of ACR (mg/mg) to mGFP/tdTomato ratio in **B)** BTBR *ob/ob*, **D)** Adriamycin and **F)** THSD7A⁺-MN mice. Only THSD7A⁺-MN mice showed a significant correlation in large (R = 0.4165) or small (R = 0.4879) urinary EVs. BTBR *ob/ob* pooled from two independent experiments (N = 7 per group), mean ± SEM; *p < 0.05 (Mann-Whitney U-test). ADR pooled data from two independent experiments (N > 9 per group) and THSD7A⁺-MN pooled values from one experiment (N > 5 per group) both presented as mean ± SEM; ****p < 0.0001, ***p < 0.001 and **p < 0.01, analyzed using two-way ANOVA with Tukey's multiple comparison test.

4.1.4 Ubiquitin proteasomal proteins are present in uEVs in a disease specific manner

The next investigation examined whether the proteostatic state of podocytes in mice is reflected in the UPS protein content found within urinary lEVs and sEVs. This approach aimed to determine whether changes in UPS proteins directly mirror disease status, providing a non-invasive source for protein-based biochemical analysis. To address this, the two nephrotic models of podocyte injury inducible in BALB/c mice, ADR nephropathy and THSD7A-associated MN were employed. These models were chosen due to previously reported proteasomal disturbances in MN and the suitability of the ADR model as a comparable experimental system.

First, it was examined whether or not the extent of proteostatic changes occurring in glomeruli especially in podocytes was similar between the THSD7A$^+$-MN and ADR mouse models. In order to visualize the accumulation of aggrieved proteins, proteasome substrates (K48-polyubiquitin, Fig. 11A, B) and oxidatively modified proteins (8-oxo guanine, Fig. 11C, D) were stained in day 12 kidney sections. There was a difference in the strength of the signal for K48-polyubiquitin and 8-oxo guanine mostly found in podocytes, whereas mesangial and glomerular endothelial cells showed lower abundance of these proteins under both adriamycin nephropathy and THSD7A$^+$-MN experimental conditions. An increased signal for K48-pUB and 8-oxo guanine was observed in podocytes of THSD7A-antibody injected mice compared to those injected with control rabbit IgG (white arrows Fig. 11B, D). Both markers for damaged proteins in podocytes of ADR mice showed a slight but not significant increase in their intensity compared to control mice (Fig. 11A, C). To quantify K48-polyubiquitinated proteasome substrates and the immunoproteasomal subunit Lmp7, immunoblots of total glomerular lysates derived from day 12 sacrificed THSD7A$^+$-MN, ADR and corresponding control mice were performed. Glomerular lysates of adriamycin and PBS control mice exhibit comparable amounts of K48-pUB and Lmp7 (Fig. 11E), while THSD7A$^+$-MN mice showed a significant increase of K48-pUB proteins and Lmp7 compared to unspecific rabbit IgG injected control mice (Fig. 11F). The deubiquitinating enzyme UCH-L1, which is induced and *de novo* expressed upon podocyte injury[151] was significantly increased in both podocyte injury models compared to their respective controls (Fig. 11E, F). In summary, these findings indicate that podocyte proteostasis is differentially impacted in mice with antibody-mediated THSD7A$^+$-MN and toxic ADR nephropathy.

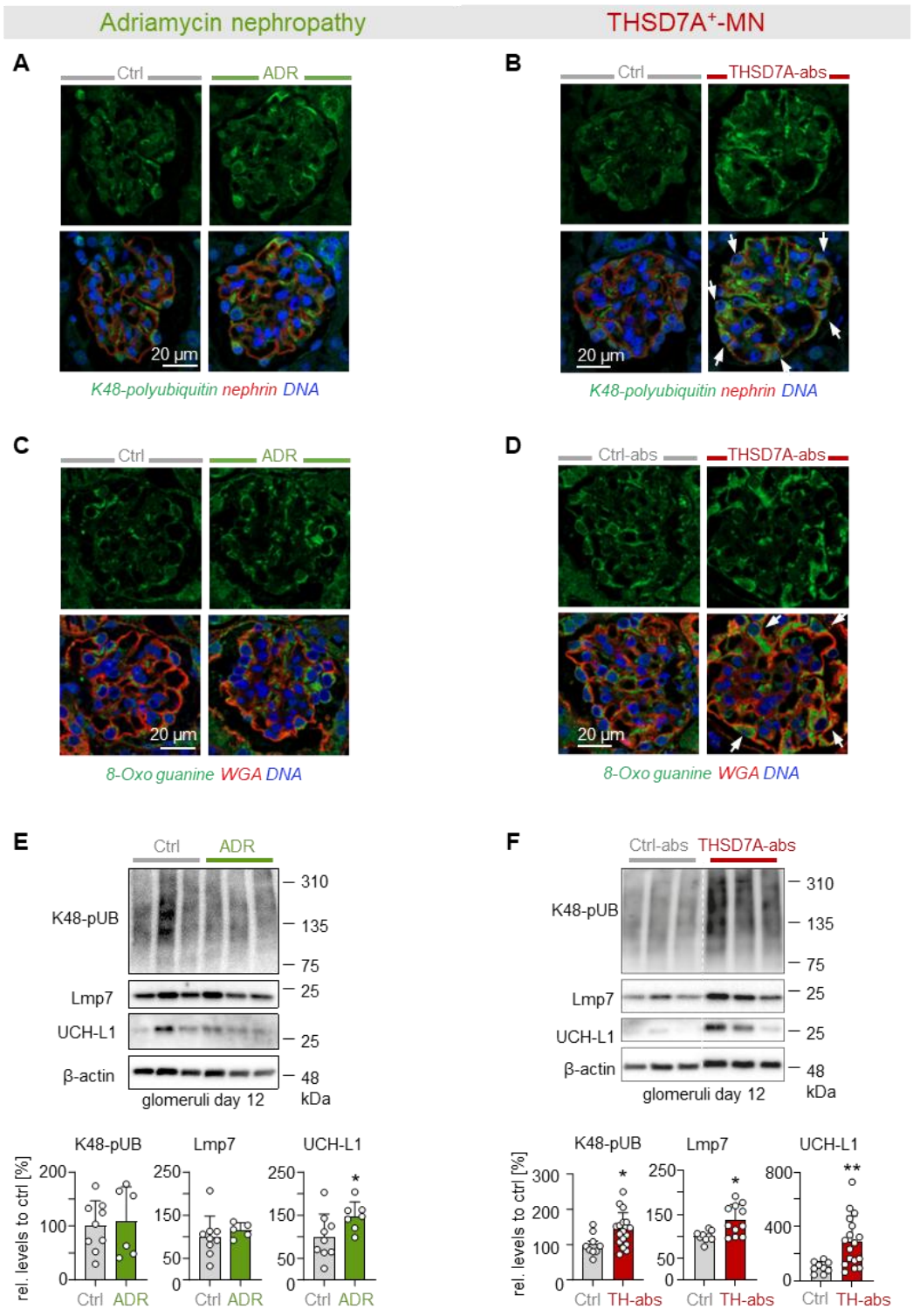

Figure 11: Proteostatic alterations in glomeruli of mice with ADR nephropathy and THSD7A⁺-MN. BALB/c mice were treated either with Adriamycin (ADR, green) and PBS as control (Ctrl, grey) or injected with rbTHSD7A-abs (TH-abs, red) and unspecific rbIgG as control (Ctrl-abs, grey). Confocal images of immunofluorescence stainings of glomeruli on day 12 was performed to examine (**A, B**) the proteasome substrate K48-polyubiquitin (green), Nephrin (red), and DNA (blue), and (**C, D**) oxidative-modified proteins (8-oxo guanine, green), wheat germ agglutinin (WGA, red), and DNA (blue). White arrows highlight podocytes in THSD7A⁺-MN mice showing an enhanced fluorescent signal for K48-pUB and 8-oxo guanine. (**E, F**) Immunoblot analyses to quantify proteasome substrates, including K48-pUB, immunoproteasome subunit Lmp7, and deubiquitinating enzyme UCH-L1 in day 12 glomerular lysates. The graphs show densitometric quantification, normalized to β-actin of the same membrane. Data are presented as mean ± SEM and expressed as % change relative to control. Statistical significance is indicated as $*p < 0.05$, $**p < 0.01$, using the Mann-Whitney U test. ADR: Pooled data from 3 independent experiments (N > 5 per group). THSD7A⁺-MN: Pooled data from 3 independent experiments (N > 9 per group).

Based on these findings, it was further investigated if the proteostatic discrepancies seen in podocytes were also reflected in released urinary EVs. Therefore, the abundance of K48-pUB, Lmp7 and UCH-L1 was analyzed by immunoblotting of lEVs and sEVs isolated from 100 µl urine. Urine samples were collected before the induction of nephrotic syndrome (UT = untreated) and on the following days 1, 3, 5, 9 and 12 after disease induction on day 0. For analysis and comparison of immunoblot signals, the protein of interest (POI) signal was normalized to the vesicle marker TSG101. Lmp7, UCH-L1 and K48-pUB were found in the urinary lEVs and sEVs of ADR mice (Fig. 12A). When compared to control mice, K48-pUB levels showed no significant change throughout the course of disease. In contrast, the abundance of UPS proteins increased slightly for Lmp7 and strongly for UCH-L1 in lEVs and sEVs during the course of the disease (Fig. 12B). Both vesicle size groups were analyzed as a pooled group because in the previous experiments, no significant differences in the protein abundance in lEVs and sEVs were seen. Further, immunofluorescence stainings from day 12 glomeruli of these mice for K48-pUB, UCH-L1 and Lmp7 revealed an increase in UCH-L1 expression but no differences for K48-pUB and Lmp7 (Fig. 12D). Additionally, no significant correlation was found between the abundance of UPS proteins in urinary EVs and their corresponding levels in glomerular tissue, as demonstrated by spearman correlation analyses (Fig. 12C). For the correlation, the mean fluorescence intensity (MFI) of each POI was quantified per glomerular area in the respective immunofluorescence stainings (Fig. 12D) and correlated to the normalized EV immunoblot signal intensities calculated as a percentage to control, pooled from days 9 and 12.

Same analyses as in ADR mice were done in the THSD7A^{+}-MN model. Immunoblot results revealed a striking increase of K48-polyubiquitinated proteins, Lmp7, and UCH-L1 abundance in lEVs and sEVs, in contrast to the ADR mice (Fig. 12E, F). Similarly, immunofluorescence stainings on day 12 mouse kidneys showed an increase in K48-pUB, UCH-L1 and Lmp7 expression (Fig. 12H). Furthermore, a substantial correlation between the abundances of UPS proteins in uEVs and the MFI in kidney sections could be observed in the THSD7A^{+}-MN compared to control mice (Fig. 12G).

These findings in two different mouse models of podocyte injury leading to nephrotic syndrome suggest that the abundance of UPS proteins within urinary EVs can be a reflection of the state within glomeruli, which is particular to the underlying disease.

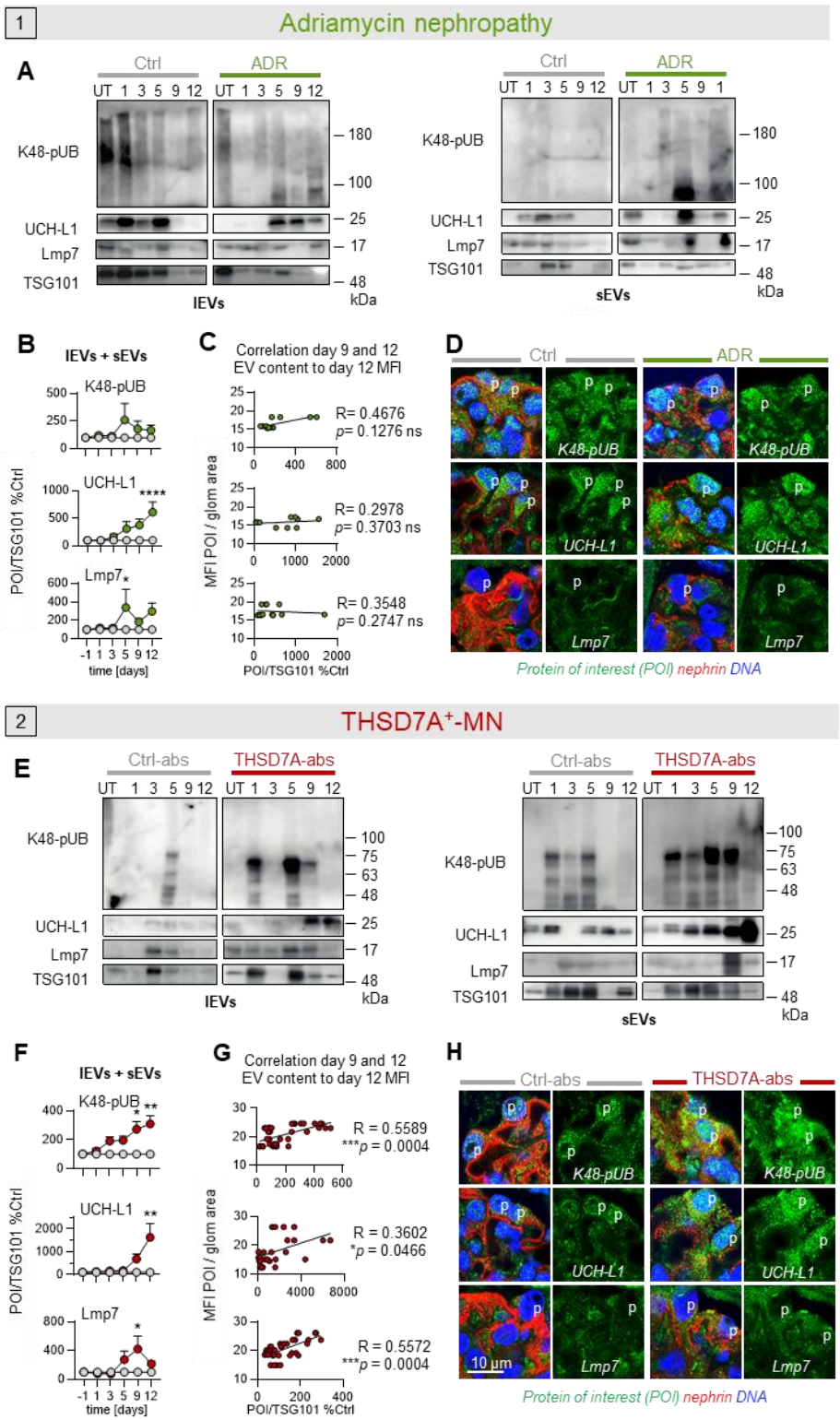

Figure 12: Podocyte proteostasis disruption in THSD7A⁺-MN is mirrored in altered ubiquitin-proteasomal protein levels in urinary EVs. Large (lEVs) and small EVs (sEVs) were enriched from 100µl urine samples collected on days -1, 1, 3, 5, 9, and 12. Mice received either 1) Adriamycin (ADR, green) or PBS (Ctrl, grey) or 2) THSD7A-abs (red) or non-specific rabbit IgG (Ctrl-abs, grey). **A, E)** Protein levels of K48-pUB, UCH-L1, Lmp7, and the vesicle marker TSG101 in enriched urinary vesicles were analyzed via immunoblot, with representative time courses shown for one mouse per group. **B, F)** Graphs display protein abundance in lEVs and sEVs, normalized to TSG101 and expressed as mean ± SEM relative to controls at each time point. **C, G)** Spearman correlation plots show the relationship between K48-pUB, UCH-L1, and Lmp7 levels in EVs (day 9 and 12) and mean fluorescence intensity (MFI) per glomerular area (% of control) on the x-axis and y-axis, respectively. **D, H)** Immunofluorescence images from day 12 illustrate glomerular staining of proteins of interest, with p indicating podocytes. Data pooled from three independent experiments (N > 7 per group). Mean ± SEM; *p < 0.05, **p < 0.01, ****p < 0.0001, two-way ANOVA with Tukey's multiple comparisons test.

4.1.5 Establishing a human podocyte-specific EV isolation method using GLEPP1 immunoprecipitation

To evaluate the clinical relevance of our experimental findings that urinary EVs reflect the protein status in mouse glomeruli, we next examined in patients with glomerular injuries whether the abundance of proteins of interest within podocyte-derived urinary EVs reflect the histological expression levels within podocytes of the same patients.

An isolation method for podocyte-specific EVs from human urine was developed, with the intention of enabling a podocyte-specific evaluation of the proteostatic condition in patients. Therefore, an immunoprecipitation approach was chosen by targeting GLEPP1, a podocyte specific membrane protein tyrosine phosphatase (PTPase) with a large extracellular domain including eight fibronectin type III-like repeats, a hydrophobic transmembrane region, and a single PTPase domain[211]. Immunofluorescence stainings in cryosections of human kidney demonstrates the specific binding of the anti-GLEPP1 antibody that was used for the pulldown of podocyte-derived EVs only in podocytes (Fig. 13A). In a first step, the purity of isolated EVs via GLEPP1 immunoprecipitation (IP) in comparison to the total EV fraction (input) was proven. In brief, GLEPP1 antibodies were covalently coupled to tosylactivated magnetic beads, and subsequently incubated with total urinary EVs (input=I), isolated from healthy urine donors or from cell culture medium of HEK cells as negative control which do not express the podocyte-specific proteins GLEPP1 and Nephrin. The input total EV- (I), wash- (W) and eluted GLEPP1$^+$ EV (E)- fractions were subjected to immunoblot validation, which revealed that urinary as well as HEK-cell derived total EVs contained general EV markers like TSG101 and AnnexinA1, and were positive for α-Actinin-4 (Fig. 13C). Furthermore, only the urinary EVs are shown to be positive for the podocyte protein Nephrin. The use of GLEPP1-coupled beads to enrich podocyte-specific EVs (E) was successful within the human uEVs as depicted by the immunoblot detection of all analyzed proteins. Within the HEK cell EVs, the use of GLEPP1-coupled beads resulted in the enrichment of only low amounts of EVs, demonstrating a precise and specific immunopreciption approach of human podocyte-specific uEVs (Fig. 13C). Additionally, the enrichment of a homogenous EV population from human urine via GLEPP1-coupled beads was shown by electron microscopic analysis of GLEPP1$^+$ EVs and total EVs (input) enriched from healthy human urine in comparison to the respective HEK cell EV fractions. Only a few unspecifically bound EVs were found in the HEK cell preparation, whereas the urinary GLEPP1$^+$ EV fraction revealed a high abundance of EVs (Fig. 13B). In general, the size of HEK EVs was shown to be smaller than the size of human urinary EVs, as evidenced by the NTA measurement. Further the GLEPP1$^+$ EV population (E) was overall more homogenous in size compared to the total EV fraction (I) (Fig. 13D). In conclusion, these results confirm the enrichment of podocyte-derived EVs from healthy human urine by using GLEPP1 as target protein.

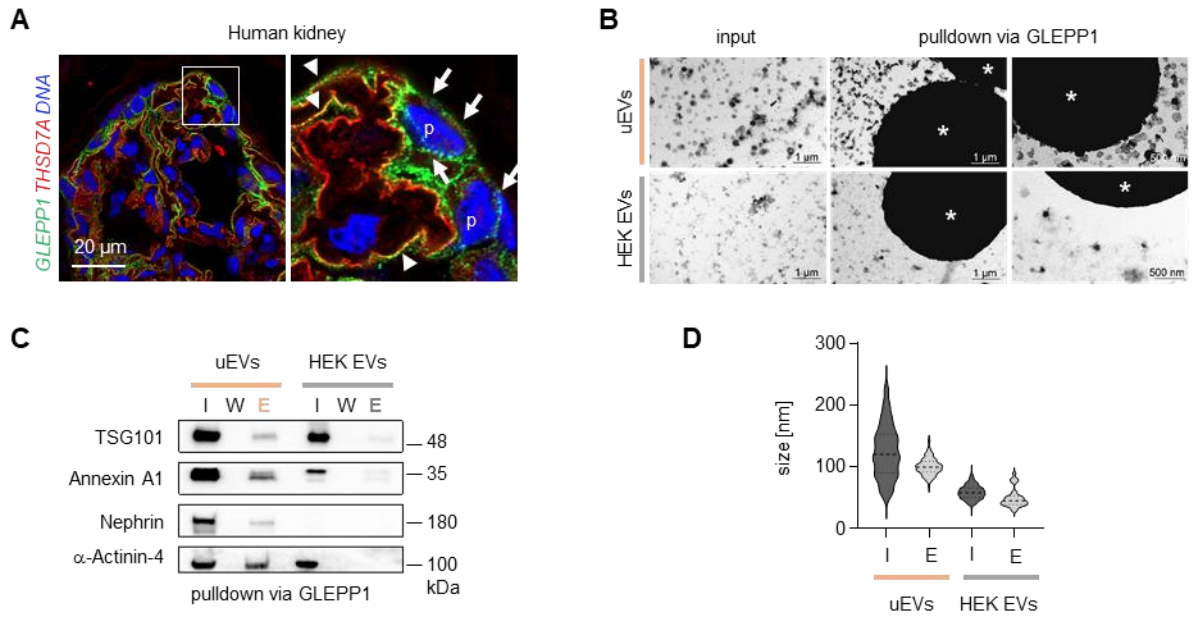

Figure 13: GLEPP1 pulldown enables enrichment of podocyte-derived uEVs from human urine. A) Immunofluorescence staining of a human kidney cryosection for GLEPP1 (green), THSD7A (red), and DNA (blue). Arrows indicate apical membrane expression, while arrowheads highlight GLEPP1 localization at foot processes. **B-D)** Characterization of EVs enriched via GLEPP1 pulldown from healthy human urine (uEVs) and human embryonic kidney (HEK) cell medium (HEK-EVs). **B)** Electron microscopy comparing GLEPP1$^+$ EVs with total EVs from urine and HEK cells; asterisks mark magnetic beads used for enrichment. **C)** Immunoblot analysis of vesicle markers (TSG101, Annexin A1) and podocyte markers (Nephrin, α-Actinin 4) in GLEPP1$^+$-EV lysates. I = total EV input, W = wash fraction, E = GLEPP1$^+$ EV eluate. **D)** Nanoparticle tracking analysis (NTA) of EV size distribution.

4.1.6 Human urinary podocyte-derived EVs mirror podocyte proteostasis alterations

The next step involved investigating whether UPS proteins could be detected in EVs derived from podocytes in nephrotic patients, and whether their abundance reflected the proteostatic condition of the podocytes. For this purpose, urine samples were collected from patients diagnosed with THSD7A$^+$-MN, PLA$_2$R1$^+$-MN, FSGS, and DN on the day of admission for a diagnostic kidney biopsy. Initially, immunofluorescence staining for K48-linked polyubiquitin (K48-pUB) was performed on the corresponding kidney biopsies. All patient samples exhibited K48-pUB signals, albeit with varying intensities (Fig. 14A). The THSD7A$^+$-MN and DN patient biopsies exhibited the strongest K48-pUB fluorescent signal in the glomerulus, especially in podocytes, while the biopsies from the PLA$_2$R1$^+$-MN and FSGS patients showed a lower fluorescent signal for K48-pUB in the immunofluorescence analysis. Urinary GLEPP1$^+$ EVs were then isolated by magnetic bead immunoprecipitation from total urinary EVs and the presence of proteasomal (K48-pUB, UCH-L1, LMP7), podocyte (Nephrin, α-Actinin-4 and THSD7A) and vesicle markers (Flotilin, Annexin A1, TSG101) was confirmed by immunoblot (Fig. 14B). Strikingly, vesicle marker detection was low in the GLEPP1$^+$ EV fraction from the PLA$_2$R$^+$-MN and DN patient, compared to the THSD7A$^+$-MN and FSGS patients, suggesting a higher podocyte-derived EV amount in the urine of the FTHSD7A$^+$-MN and FSGS patients.

The podocyte proteins Nephrin and α-Actinin-4 revealed an almost comparable abundance within the GLEPP1⁺ EV fraction among the patients, whereas the abundance of THSD7A protein was increased within the GLEPP1⁺-EV fraction from the THSD7A⁺-MN patient. UPS protein detection revealed the presence of K48-pUB, UCH-L1 and LMP7 in GLEPP1⁺ EVs of all four patients. While THSD7A⁺-MN, PLA_2R1^+-MN and DN patients showed comparable protein amounts of these UPS players, the FSGS patient showed a lower amount, especially in the immunoproteasome subunit LMP7 signal (Fig. 14B). The mean fluorescence intensity (MFI) of K48-pUB within podocytes per podocyte area was measured in the biopsy immunofluorescence stainings of the patients and correlated to the respective amount of K48-pUB in GLEPP1⁺ EVs, analyzed by immunoblot after normalization to TSG101. The stacked graphs illustrate the comparable abundance of K48-pUB proteins in GLEPP1⁺ EVs (WB) to the mean fluorescent intensity of K48-pUB per podocyte area in the patient biopsies (Fig. 14C). To assess whether this method reliably reflects proteostatic conditions across various types of

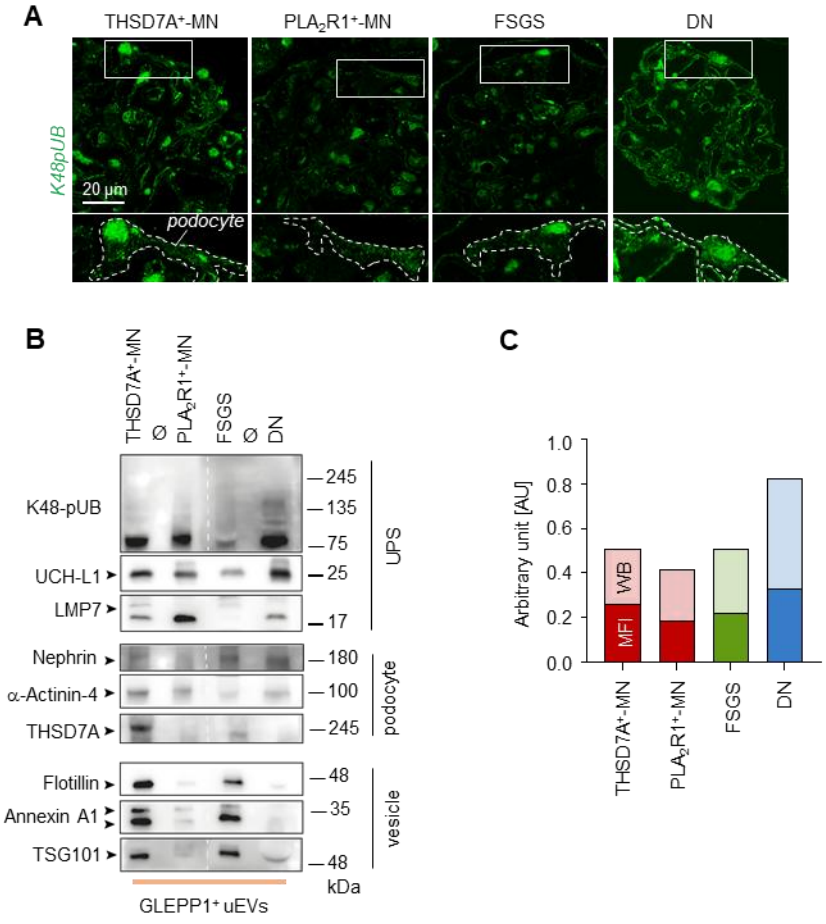

Figure 14: Non-invasive assessment of podocyte proteostasis alterations in nephrotic patients via GLEPP1⁺ urinary EVs. A) Immunofluorescence staining of kidney biopsies from patients with THSD7A⁺-MN, PLA_2R1^+-MN, FSGS, and DN, highlighting K48-pUB (green). Dashed lines outline podocyte contours. **B)** GLEPP1⁺-EVs immunoprecipitated from patient urine were analyzed by immunoblotting for UPS proteins (K48-pUB, UCH-L1, LMP7), podocyte markers (Nephrin, α-Actinin 4, THSD7A), and vesicular proteins (Flotillin, Annexin A1, TSG101). **C)** Stacked bar graphs compare mean fluorescence intensity (MFI) of K48-pUB in podocytes from biopsies with corresponding K48-pUB levels in GLEPP1⁺-EVs via Western blot (WB) analysis (AU = arbitrary units). Notably, K48-pUB levels in podocytes align with those detected in GLEPP1⁺-EVs within individual patients.

glomerular injury, further analysis with an expanded patient cohort is needed, as the current experiment primarily demonstrates technical feasibility.

4.2 Ability of vesicle formation in podocytes and dynamics of urinary EV release in experimental MN

4.2.1 Podocyte membrane alterations in early THSD7A$^+$-MN.

To investigate membrane alterations indicative of vesicle formation and EV release in THSD7A$^+$-MN, the *mT/mG* mouse model was utilized to track podocyte derived. Mice were injected with rbTHSD7A-abs or unspecific rbIgG as a control and sacrificed at 1 hour and on days 1, 2, and 3 after disease induction. Isolated glomeruli and kidney sections of control and THSD7A$^+$-MN mice of each timepoint were analyzed by immunoblot for plasma membrane and vesicle-associated proteins, like Annexin A1, 14-3-3 and flotillin. A key finding was the pronounced glomerular abundance of Annexin A1 from day 1 onward. This Ca^{2+}-dependent phospholipid-binding protein is known for its role in membrane stabilization and repair[220]. In contrast, other vesicle-associated proteins, including 14-3-3, CD9, and TSG101, showed only modest glomerular increases, while flotillin levels remained unchanged (Fig. 15A). Immunofluorescence staining in day 3 kidney slices revealed significantly increased Annexin A1 expression at the podocyte plasma membrane and along filamentous membrane extensions protruding into the urinary space. Notably, these extensions colocalized with the GFP-tagged membrane in *mT/mG* THSD7A$^+$-MN mice (Fig. 15B), strongly indicating their involvement in podocyte-derived EV release. The increased membrane presence of Annexin A1 in podocytes could suggest an adaptive response to membrane stress following immune-mediated damage, necessitating the stabilization and repair of the affected regions.

Given the critical role of oxidative stress in MN pathogenesis, it was hypothesized that plasma membrane domains exposed to the autoantibody-antigen interaction might be particularly vulnerable to vesicle formation due to oxidative stress-induced lipid peroxidation. To explore this, the abundance of 4-hydroxynonenal (4-HNE), a well-established marker of lipid peroxidation was determined. ELISA quantification revealed a significant increase in 4-HNE levels within the glomeruli of THSD7A$^+$-MN mice compared to controls throughout disease progression (Fig. 15C). Furthermore, immunofluorescence analysis of 4-HNE stained kidney sections on day 3 revealed that oxidative damage was primarily localized to the glomerular filtration barrier and podocyte plasma membrane (Fig. 15D), highlighting a direct link between immune-mediated injury and oxidative stress in MN pathogenesis.

Collectively, these findings provide compelling evidence that autoantibody binding to THSD7A triggers early and significant changes in podocyte plasma membrane protein localizations and lipid peroxidation, that could be associated with structural damage and vesicle formation.

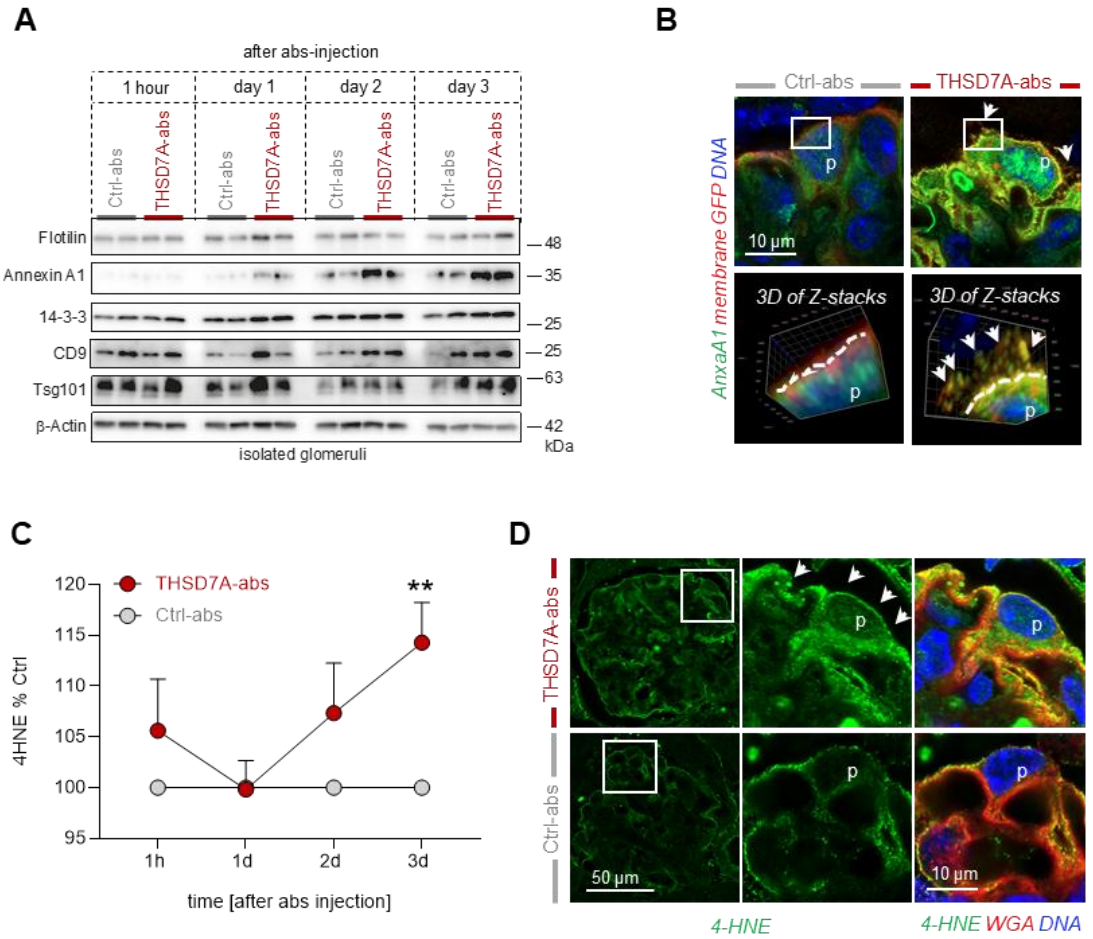

Figure 15: Glomerular and podocyte membrane alterations in initial THSD7A⁺-MN. *mT/mG* mice in the BALB/c background were injected with rbTHSD7A-abs or unspecific control rbIgG (Ctrl-abs) and sacrificed 1 hour and on day 1, 2, 3 after disease induction. **A)** Glomerular lysates were analyzed by immunoblotting for membrane and vesicle associated proteins. **B)** Immunofluorescence staining in kindney sections for Annexin A1 (AnxA1, green) and DNA (blue) together with the membrane bound GFP signal (red). Note the strong upregulated Annexin A1 at the podocyte (p) membrane in colocalization with GFP and the formation of membrane extensions into the urinary space (white arrows). Cut out shows a 3D reconstruction of the podocyte membrane. **C)** Glomerular lysates were analyzed by ELISA for 4-hydroxynonenal (4-HNE) abundance. Relative levels within THSD7A⁺-MN glomeruli were calculated as % change of control glomeruli, N = 6. **D)** Immunofluorescence staining to 4-HNE (green), wheat germ agglutinine (WGA, red) and DNA (blue) in day 3 kidney sections. White arrows highlight strong 4-HNE expression at the podocyte membrane of the THSD7A⁺-MN mouse.

4.2.2 Injected anti-THSD7A antibodies trigger podocyte vesicle formation and are released in exopher-like vesicles in experimental MN

To further investigate in more detail the morphological plasma membrane alterations seen in the THSD7A⁺-MN mice, kidneys of BALB/c mice from day 1 and 7 after antibody injection were examined using electron microscopy with immunogold labeling for rbIgG (detecting injected rbTHSD7A-abs or control rbIgG-abs) and the THSD7A protein. To preserve membrane

structures, the kidneys were *in vivo* fixed using a specialized technique designed to "freeze" membrane processes. Transmission electron microscopy (TEM) analysis of immunogold-labeled rbTHSD7A antibodies on day 1 revealed extensive subepithelial deposition in THSD7A^{+}-MN kidneys (black arrowheads, Fig. 16A), along with a few gold particles localized to the apical (urinary) side of the podocytes (orange arrowheads, Fig. 16A). In contrast, only a few non-specific control antibodies were detected in control kidneys at the glomerular basement membrane (GBM) on day 1 (Fig. 16A).

By day 7, THSD7A^{+}-MN kidneys exhibited a striking accumulation of gold-labeled rbTHSD7A antibodies (orange arrowheads) in the urinary space. These aggregates extended from the apical surface of podocyte cell bodies, as well as from major and foot processes (Fig. 16B). Notably, the subepithelial antibody localization seen on day 1 (black arrowheads) had largely

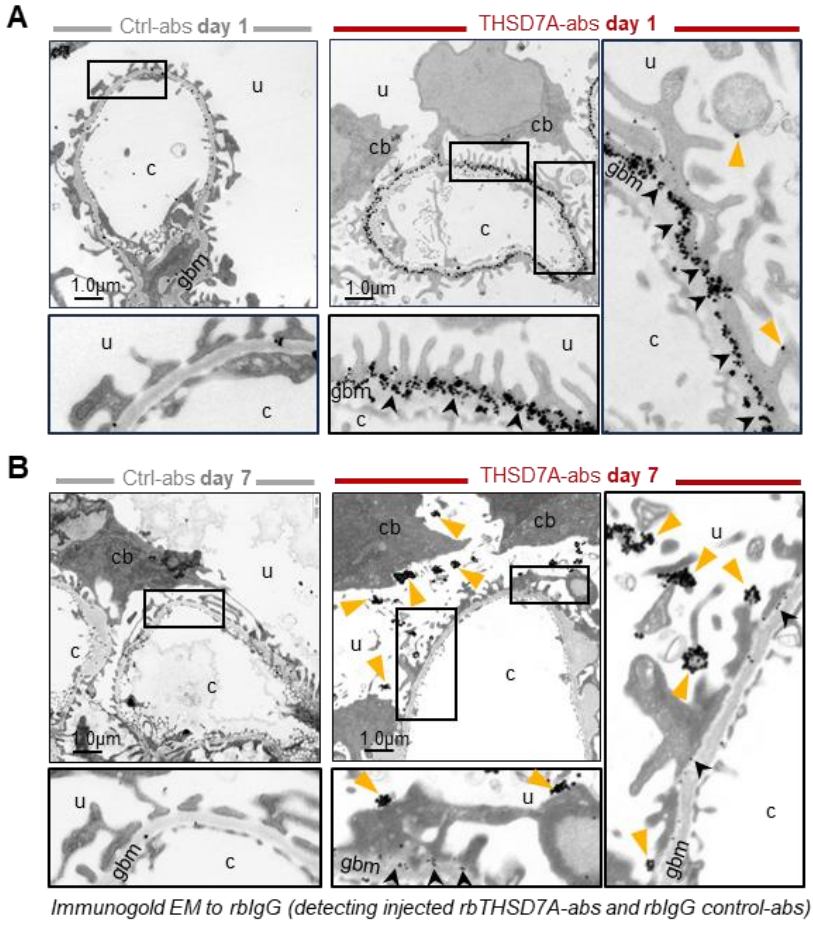

Figure 16: Immunogold EM reveals shifted localization of rbTHSD7A antibodies at early and late stages of THSD7A^{+}-MN. THSD7A^{+}-MN was induced in BALB/c mice by injecting rbTHSD7A antibodies and non-specific rabbit IgG as a control. Kidneys were collected on day 1 and 7 post-injection and fixed via in vivo perfusion to preserve membrane structures for ultrastructural analysis of antibody distribution. **A)** On day 1, rbTHSD7A-abs were primarily detected in the subepithelial space of podocytes (black arrowheads), with only a few gold-labeled antibodies present on the apical side of foot processes (orange arrowheads). In control mice, minimal non-specific rabbit IgG was observed in the glomerular basement membrane (GBM). **B)** By day 7, rbTHSD7A-abs had accumulated on apical membrane extensions from podocyte foot processes, major processes, and the cell body, forming aggregates extending into the urinary space (orange arrowheads). Only a few antibodies remained in the subepithelial space (black arrowheads), while control antibodies were nearly absent from podocytes and the GBM. Abbreviations: cb = cell body, u = urinary space, c = capillary space, gbm = glomerular basement membrane.

disappeared. In control kidneys, gold particles were scarce, with nearly no antibody presence detected in podocytes, the subepithelial space, or the GBM.

To further investigate the structure and formation of these vesicular antibody-bound aggregates, additional kidney sections from day 7 were analyzed. TEM immunogold labeling for rbIgG confirmed the initial observations, revealing gold-labeled, mulberry-like structures extending from the apical side of podocytes into the urinary space (Fig. 17A).

To confirm the specificity of antibody binding within these vesicular structures, additional immunogold labeling for the THSD7A antigen was performed. As expected, TEM images of day 7 THSD7A^{+}-MN kidneys revealed gold-labeled membrane extensions (orange arrows) arising from podocytes, mirroring the previous immunogold EM findings for the rbTHSD7A antibody gold labeling. Moreover, gold aggregates were observed along elongated membrane structures adhering to the proximal tubular brush border (bb) at the urinary pole of the glomerulus (blue arrow) (Fig. 17B).

Ultrastructural analysis using scanning electron microscopy (SEM) further highlights the striking formation of membrane extensions in THSD7A^{+}-MN mice. On day 1, control mice exhibited a smooth podocyte surface, whereas podocytes in THSD7A antibody-injected mice began to develope short membrane protrusions (Fig. 17C). By day 7, SEM analysis revealed a significant increase in both the number and length of these elongated membrane extensions. These structures originated from podocyte foot processes, major processes, and the cell body, often terminating in distinct distal bulges. In close-up views, white arrows indicate the membrane extensions emerging from podocytes, while orange arrowheads highlight the vesicular bulge structures at their tips. In contrast, rbIgG control mice maintained a smooth podocyte surface with no membrane formations even on day 7 (Fig. 17D).

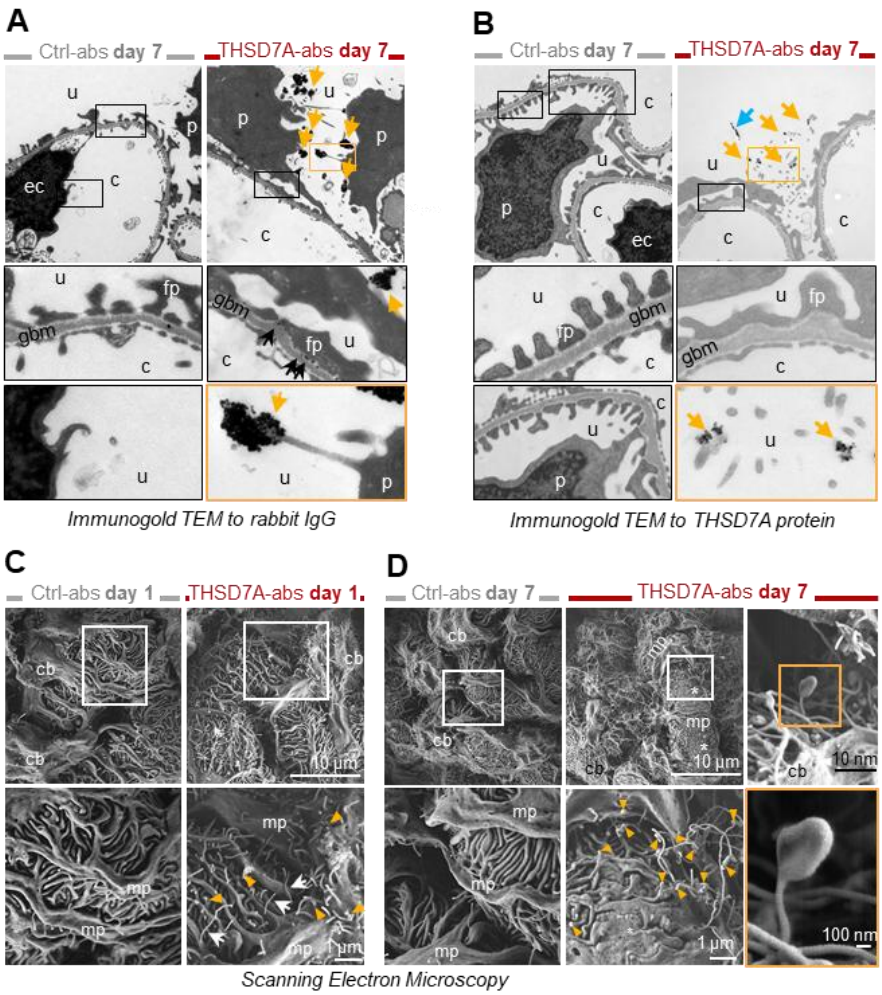

Figure 17: EM analyses reveal THSD7A antibodies trigger podocyte antigen-antibody aggregate formation with vesicular extensions into urinary space.
BALB/c mice were injected with rbTHSD7A antibodies (or abs) for MN induction and unspecific rbIgG as control. Vesicle formation in kidneys was analyzed by EM on day 1 and 7. **A)** Transmission EM (TEM) to rbIgG shows gold-labeled rbIgG aggregates in the urinary space, connected to podocyte cell body by long membrane extensions (orange arrows). Close-ups highlight subepithelial gold deposits (black arrows) and urinary gold aggregates (orange arrows). **B)** TEM to THSD7A reveals gold-labeled THSD7A aggregates in the urinary space (orange arrows), along filamentous structures (blue arrows). **C)** Membrane extensions (white arrows) with distal bulges (orange arrowheads) emerging from podocyte foot and major processes, and the cell body in a THSD7A$^+$-MN kidney on day 1. **D)** By day 7, extensions increased in numbers and large protrusions with distal bulges (orange arrowheads) are visible on the urinary side of podocyte processes and cell bodies. Control mice show a few shorter extensions, mainly from the cell body and without significant bulge formation. Areas of foot process effacement are marked with asterisks. Abbreviations: u = urinary space, c = capillary lumen, gbm = glomerular basement membrane, p = podocyte nucleus, ec = endothelial cell nucleus, mp = major process; fp = foot process.

To further investigate if the formed vesicles with the bound rbTHSD7A-abs and rbIgG control-abs are released from the podocyte into the urine, BALB/c and *mT/mG* mice in the BALB/c background were injected with rbTHSD7A-abs to induce THSD7A$^+$-MN or with non-specific control rbIgG antibodies. Urine was collected before and at various time points after antibody injection throughout the disease course. EVs were isolated and analyzed for podocyte-derived rbIgG-positive EVs (mGFP$^+$/rbIgG$^+$) by ImageStream® analysis, using an anti-rabbit cy5 antibody for detecting the injected rbTHSD7A-abs or rbIgG control-abs.

Over the course of the disease, a substantial increase in podocyte-derived uEVs (mGFP⁺) in THSD7A⁺-MN mice compared to controls was observed, as shown in Fig. 18A, graph 1. In contrast, the number of non-podocyte-derived uEVs (tdTomato⁺) remained unchanged (Fig. 18A, graph 2). These findings align with the prior shown immunoblot quantification results (Fig. 10), where it was shown that THSD7A⁺-MN podocyte injury led to an active and progressive release of urinary EVs, with a tendency for larger EVs originating from podocytes. Notably, the injected rbTHSD7A antibody could be detect on the vesicles and was almost exclusively present in EVs generated by podocytes (mGFP⁺/ rbIgG⁺), with a significant increase over time in THSD7A⁺-MN mice (Fig. 18B, graph 1). In contrast, rbIgG⁺ EVs derived from non-podocyte cells (tdTomato⁺/ rbIgG⁺) were scarce, with no notable differences between the disease and control groups (Fig. 18B, graph 2). Representative ImageStream® plots from day -1 (untreated) and day 10 in control and THSD7A⁺-MN mice are shown.

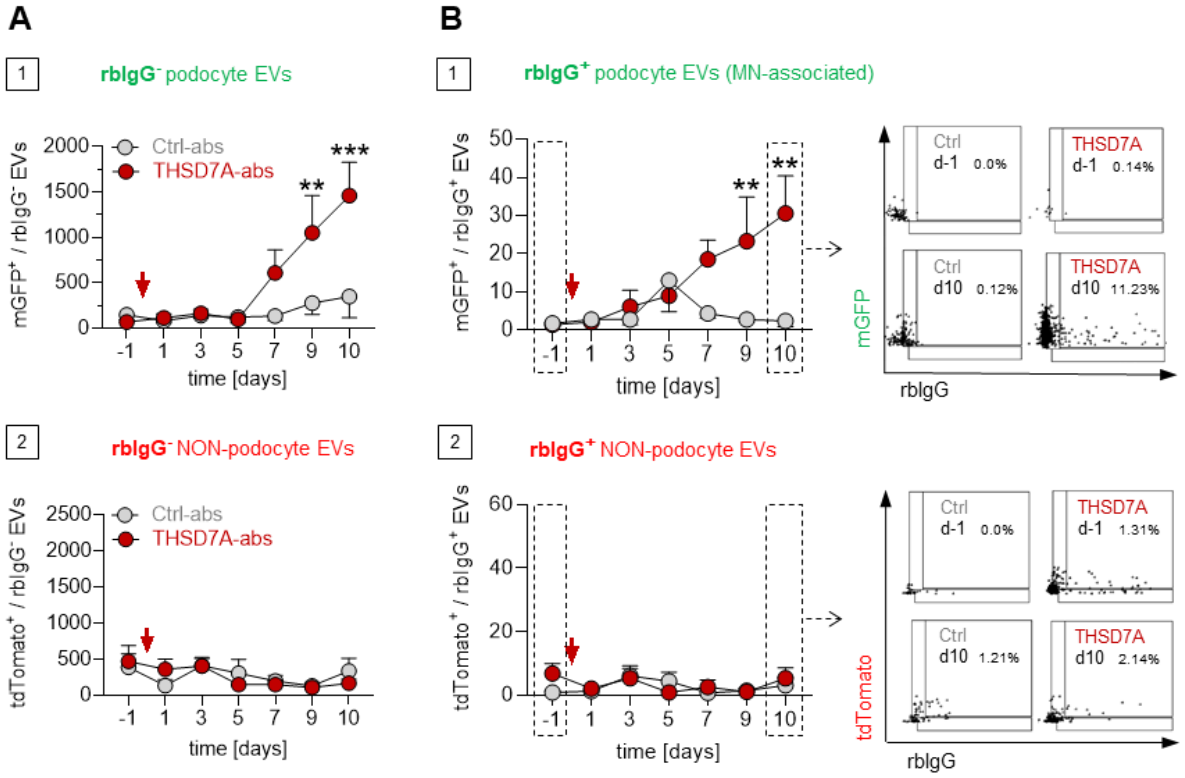

Figure 18: Injected rbTHSD7A-abs are present on the surface of podocyte-derived EVs in THSD7A⁺-MN mice. THSD7A⁺-MN was induced in *mT/mG* mice by injecting rbTHSD7A-abs, with non-specific rbIgG as a control. Urine was collected before and after disease induction, and urinary EVs were analyzed using ImageStream® to assess EV quantity and antibody presence. Podocyte-derived EVs were identified by GFP fluorescence, while non-podocyte EVs displayed tdTomato fluorescence. Injected rbTHSD7A and rbIgG antibodies were detected using a cy5 anti-rbIgG secondary antibody. **A)** Graphs 1 and 2 show the number of rabbit IgG-negative EVs from podocytes (1) and non-podocytes (2), revealing a significant increase in podocyte EVs in THSD7A⁺-MN mice (THSD7A-abs, dark red) compared to controls (Ctrl-abs, grey), while non-podocyte EVs remained unchanged. **B)** Graphs 1 and 2 track rbIgG⁺ EVs over time, showing a significant increase in rabbit antibody-positive podocyte EVs (mGFP⁺/ rbIgG⁺/) in THSD7A⁺-MN mice (dark red), whereas non-podocyte EVs (tdTomato⁺/ rbIgG⁺) (graph 1) remained low and unchanged between groups (graph 2). Representative ImageStream® plots from day -1 and day 10 for control and THSD7A⁺-MN mice are displayed.

All previously described findings suggest a vesicle-dependent mechanism for handling the antibody-antigen complexes and proteasomal disturbances in the progression of membranous nephropathy by the podocytes. These include 1) a significant increase in antibody-bound podocyte-derived EVs in THSD7A$^+$-MN mice (Figs. 10 and 18), 2) the presence of proteins related to the ubiquitin-proteasome system in murine EVs, with elevated levels of K48 poly-ubiquitinated proteins, the proteasomal subunit LMP7, and the deubiquitinating enzyme UCH-L1 (Figs. 11 and 12). This coincides with an increased of oxidated podocyte membrane as well as accumulation of damaged proteins in glomeruli (Figs. 11, 12 and 15), suggesting proteotoxic stress in podocytes, and 3) morphological analysis showing the formation of elongated membrane protrusions and vesicular bulges containing bound antibodies and antigen in the urinary space (Figs. 16 and 17).

From their morphologic and molecular setup, these structures closely resemble a specific vesicle subtype known as exophers. Exophers are a recently identified type of extracellular vesicle discovered in *Caenorhabditis elegans*[185]. In *C. elegans*, exophers emerge through a distinct budding process from the plasma membrane, forming elongated nanotubules that can expand to a distal diameter of up to 4 µm[212]. These structures primarily serve as a cellular clearance mechanism, facilitating the removal of proteotoxic protein aggregates from neurons, and were recently also shown in murine cardiomyocytes[213]. Notably, exopher production is upregulated under conditions of cellular stress, particularly when proteasomal function is impaired[187, 212].
Given the structural (elongated nanotubules from the plasma membrane), functional (aggregate removal), and stress-induced formation similarities, the MN-associated urinary EVs with the bound antibody, are in the following now referred to as exopher-like vesicles (ELVs). Further detailed analyses of these vesicles were conducted to better understand their role in MN pathology.

4.2.3 Proteasome function affects release of MN-associated exopher-like vesicles

In *C. elegans*, exopher biogenesis increases under cellular stress, particularly when proteasomal function is impaired[187, 212]. To explore whether the release of MN-associated exopher-like vesicles (ELVs) into the urine depends on proteasome activity and if this is influenced by proteotoxic stress, THSD7A$^+$-MN was induced in *mT/mG* reporter mice, which were divided into three experimental groups. The first group served as the standard THSD7A$^+$-MN model, the second group received daily treatment with the proteasomal inhibitor epoximicin starting on day 7 after antibody injection to achieve proteasomal inhibition, and the third group received vehicle injections from day 7 onward as control. The experimental design, including treatment groups and urine collection time points, is illustrated in Fig. 19A.

Isolated total EVs from collected urines were monitored for ELV (rbIgG$^+$ EVs) abundance over the disease course in all treatment groups using ImageStream® analysis. Simultaneously, albuminuria was measured to track podocyte injury severity together with ELV release dynamics. In THSD7A$^+$-MN mice, ELVs appeared in urine as early as day 1 post-induction, peaking on day 3 (Fig. 19B, panel 1, left y-axis, red circles). Albuminuria was detectable from day 1, progressively worsening over time, reaching ~90 g/g albumin per creatinine by day 10 (Fig. 19B, panel 1, right y-axis, orange squares). While ELV release initially surged, it later declined as disease progression continued, whereas albuminuria worsened (Fig. 19B panel 1).

To assess the impact of proteasomal inhibition on ELV dynamics, rbIgG$^+$ EV abundance was normalized and shown as relative percentage to vehicle-treated THSD7A$^+$-MN mice. The red squares/dashed line represent vehicle-treated mice, while blue circles indicate proteasome-inhibited animals (Fig. 19B, panel 2, left y-axis). Albuminuria relative to vehicle-treated THSD7A$^+$-MN mice is shown on the right y-axis (orange squares).

Proteasomal inhibition with epoxomicin, initiated on day 7, resulted in a rapid and significant increase in ELV release (~70%), compared to vehicle-treated THSD7A$^+$-MN mice. Concurrently, albuminuria decreased in proteasome-inhibited THSD7A$^+$-MN mice (Fig. 19B, panel 2). By day 10, ELV abundance returned to levels comparable to vehicle-treated animals, while at the same time albuminuria worsened.

Super-resolution microscopy of optically cleared kidney sections (day 10) visualized ELV formation and release in the two treatment groups. Podocytes were identified by their GFP expression (green), and bound rbTHSD7A antibody was detected with a secondary anti-rabbit antibody (red). THSD7A antibody accumulation was present in both treatment groups, proteasome-inhibited THSD7A$^+$-MN mice exhibited significantly larger and more numerous glomerular aggregates in the urinary space. ELVs were observed in the urinary space, characterized by long mGFP$^+$ membrane extensions originating from podocyte cell bodies, with large distal rbTHSD7A-ab aggregates (Fig. 19C). Additionally, ImageStream® analyses of urine from epoxomicin treated THSD7A$^+$-MN mice confirmed podocytes as the primary source of ELVs under proteotoxic stress. Podocyte-derived EVs (mGFP$^+$) with bound antibody (rbIgG$^+$) corresponding to ELVs, increased significantly after starting proteasomal inhibition on day 7 compared to vehicle treated THSD7A$^+$-MN mice. Representative ImageStream® plots from day 9 are shown (Fig. 19D). In contrast, podocyte-derived EVs without bound antibody (mGFP$^+$/rbIgG$^-$), as well as non-podocyte EVs from proteasomal inhibited mice showed only minimal changes in EV abundance compared to THSD7A$^+$-MN (Fig. 19D). Hence, ELVs are almost exclusively released by podocytes, their abundance is strongly increased under proteasomal inhibition and seems to influence the course of albuminuria in THSD7A$^+$-MN.

To rule out the possibility that ELV release declined in late disease stages due to a loss of circulating THSD7A antibodies, immunoblot analysis of serum collected on day 10 was performed to detect the injected rbTHSD7A-abs and rbIgG control-abs. For this, immunoblots loaded with HEK cell-expressed THSD7A or PLA_2R1 lysates were incubated with a $THSD7A^+$-MN or an epoxomicin treated $THSD7A^+$-MN mouse serum as the primary antibody, followed by a secondary anti-rabbit-HRP antibody. The resulting immunoblots (Fig. 19E) confirmed persistent circulating rbTHSD7A-specific antibody in both vehicle- and proteasome-inhibited mice sera, indicating that declining ELV release was independent of reduced antibody availability in the serum of $THSD7A^+$-MN mice.

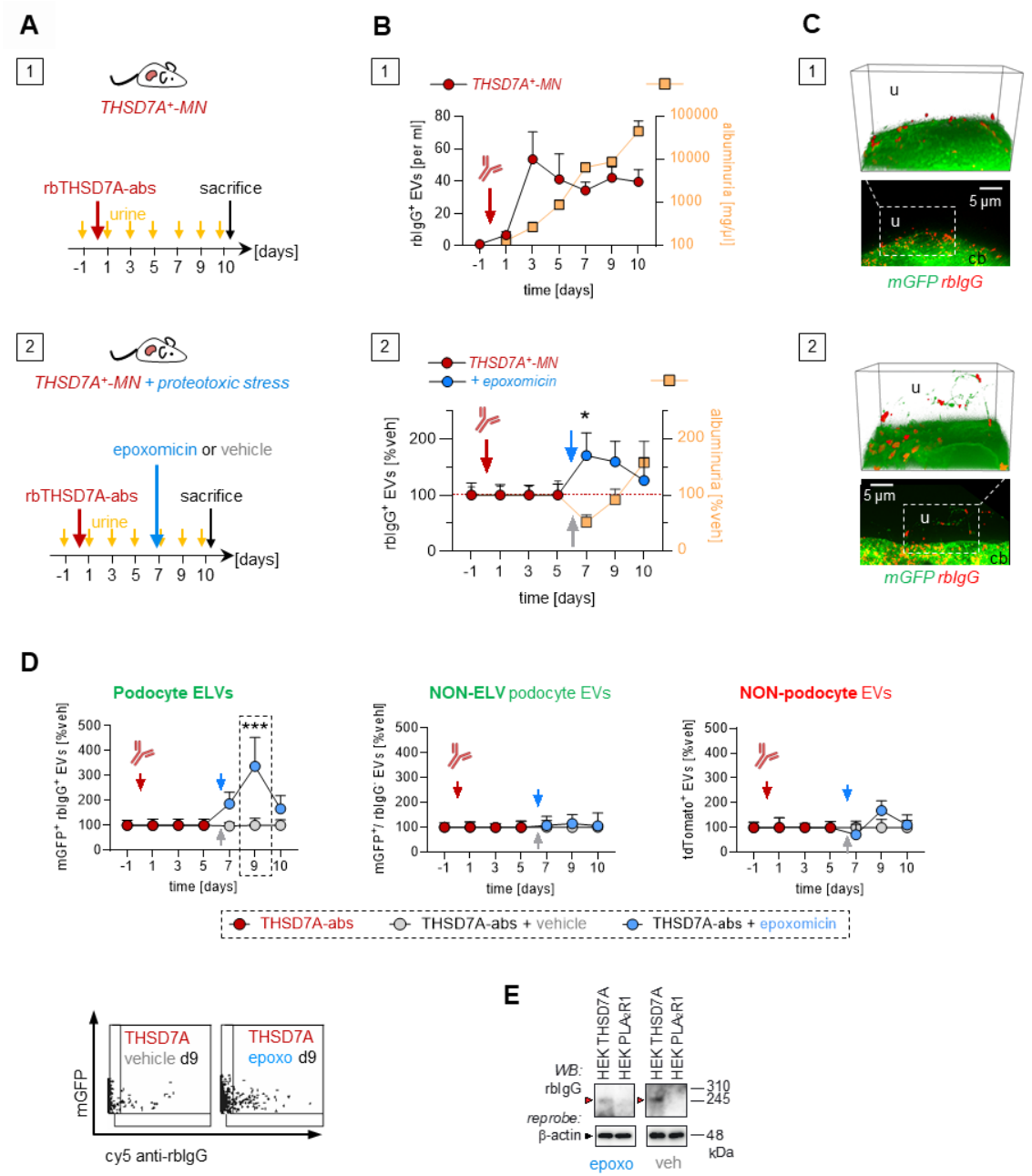

Figure 19: Proteasomal inhibition modulates urinary ELV release in experimental THSD7A⁺-MN. A) Experimental setup**:** Induction of THSD7A⁺-MN (**panel 1**) and THSD7A⁺-MN with proteasomal inhibition (**panel 2**). in *mT/mG* reporter mice on day 0 by administering rbTHSD7A-abs (dark red arrow) and epoxomicin or vehicle daily from day 7 on after disease induction. Urine was collected over time, and on day 10 the mice were sacrificed. **B)** Urinary rbIgG⁺-EV abundance was assessed from 10^9 total EVs using ImageStream® analysis, alongside albuminuria measurements. **Panel 1:** Graph shows urinary ELV abundance (rbIgG⁺-EVs; particles/ml; left y-axis) in THSD7A⁺-MN mice (dark red circles) and albuminuria (right y-axis, orange squares) over time. **Panel 2:** Mice received either epoxomicin or vehicle as control (daily from day 7 on). Graph shows urinary ELV release (left y-axis, colored circles) and albuminuria (right y-axis, orange squares) relative to vehicle-treated THSD7A⁺-MN mice (dashed lines at 100%). Data pooled from three experiments (N > 9 per group), mean ± SEM; *p < 0.05, 2-way ANOVA with Tukey's post-test for multiple comparisons. **C)** Kidney slices from *mT/mG* reporter mice, which express membrane-bound GFP (mGFP, green) in podocytes, were optically cleared and stained for bound rbTHSD7A-abs (red). 3D-reconstructed z-stacks show the podocyte cell body (cb) plasma membrane; u = glomerular urinary space. **D)** Quantification of EV-subpopulation release in response to epoxomicin treatment relative to vehicle-THSD7A⁺-MN *mT/mG* mice. **Left panel**: relative release of MN-associated ELVs from podocytes with representative Image Stream plots shown from day 9. **Middle panel**: relative release of podocyte EVs without bound rbIgG (non-ELV podocyte EVs) and **right panel**: relative release of non-podocyte EVs (mTomato⁺ EVs). Mean ± SEM, N = 7 per group, pooled data from 2 independent experiments, ***p ≤ 0.001, 2-way ANOVA with Tukey`s post-test for multiple comparisons test. **E)** Circulating rbTHSD7A-abs are still detectable in the day 10 serum of epoxomicin and vehicle treated mice. Serum was 1:2 diluted and used as primary antibody on HEK cell lysate containing human THSD7A or human PLA_2R1 protein (as negative control). Representative immunoblots are shown.

4.2.4 Extent of ELV release correlates with glomerular immuncomplex accumulation

To assess whether the increased ELV release in THSD7A^{+}-MN has protective role for podocytes, correlation analyses in epoxomicin-treated mice were performed. Albuminuria (g/µl) and urinary ELV abundance (particles/ml) were pooled from days 9 and 10, revealing a weak inverse correlation between urinary ELV release and albuminuria (r = 0.35) (Fig. 20A, panel 1). Additionally, the amount of THSD7A protein and rbIgG deposited within glomeruli was analyzed by immunoblot (Fig. 20B). Calculations of total glomerular THSD7A and rbIgG abundance was accomplished using both, the soluble and insoluble glomerular fraction of 200 glomeruli, to detect the cytosolic as well as the membrane-bound aggregated proteins. For this, glomeruli were first lysed with TPER to generate the soluble fraction. To subsequently gain the unsoluble fraction, a second lysis step of the TPER pellet was performed with urea (Fig. 20B). Densitometry of THSD7A and rbIgG heavy chain (HC) immunoblot signal was done, to obtain the respective protein abundance per glomerulus in an arbitrary unit (A.U.). These data were correlated to released urinary ELVs from day 9 and 10 and showed a significant inverse correlation between urinary ELV release and glomerular THSD7A (r = -0.51) as well as rbIgG (r = -0.54) amounts. Higher urinary ELV release was associated with lower glomerular antigen/autoantibody deposition (Fig. 20A, panels 2 and 3).

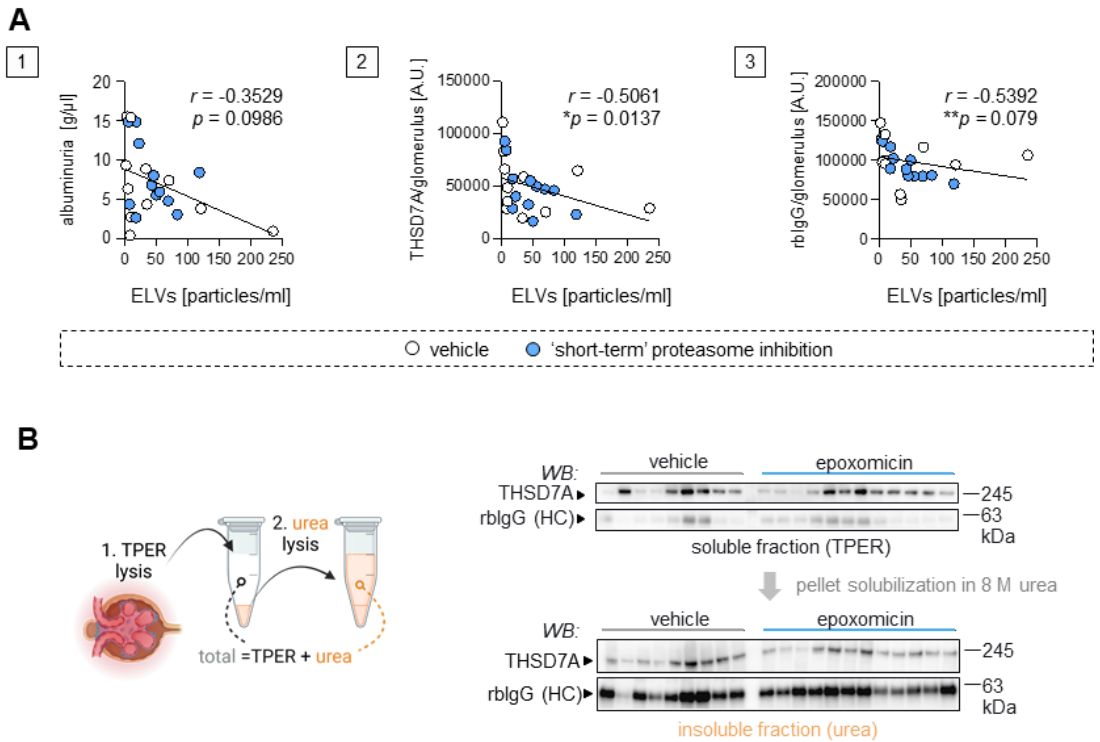

Figure 20: Glomerular antigen burden correlates with urinary ELV abundance. A) Spearman's correlation analysis of **panel 1:** albuminuria (g/µl) and **panels 2 and 3:** total glomerular THSD7A (2) and rbIgG (3) protein abundance vs. corresponding urinary ELV abundance (particles/ml) at the time of sacrifice. **B)** Overview of the principal workflow for glomerular fraction analyses. Glomeruli were isolated, counted, and processed into soluble (TPER) and insoluble (urea) fractions (200 glomeruli per mouse). These fractions were separated via reducing SDS-PAGE, followed by immunoblotting on the same membrane to assess THSD7A and rbIgG heavy chain (HC) protein abundance.

In conclusion, rbTHSD7A-ab exposure induces significant urinary ELV (mGFP$^+$/rbIgG$^+$ EVs) release by podocytes, a process that is rapidly enhanced by proteasome inhibition but diminishes with prolonged inhibition. Correlation analyses suggest that ELV release helps reduce antigen/antibody accumulation in glomeruli, implying that a balanced ELV formation and release may have a protective function in experimental MN.

4.3 Exopher-like vesicles in human membranous nephropathy

To validate the identification of the ELVs and assess their pathological significance in human membranous nephropathy, investigations were extended to biopsy and urine samples from patients in order to carry out a comprehensive analysis of the extracellular urine vesicles using modern molecular methods (expression of a characteristic set of EV markers), content (abundance of cell-specific and disease-associated proteins, presence of organelles), and dynamic criteria (enhanced release by proteotoxic stress, reuptake by cells along the nephron).

4.3.1 ELVs are the pathobiological correlate of glomerular urinary space aggregates in human MN.

Diagnostic kidney biopsies from a 62-year-old male THSD7A$^+$-MN patient and from a 20-year-old female PLA$_2$R1$^+$-MN patient revealed antigen-positive aggregates within the glomerular urinary space, attached to podocytes via membrane extensions (WGA membrane staining), as observed by confocal microscopy (Fig. 21A, B, orange and red arrows). These structures closely resemble the ELV formations seen in the THSD7A$^+$-MN mouse model described before. Immunofluorescence stainings confirmed that these antigen aggregates were strongly positive for human IgG4 (huIgG4), the primary autoantibody IgG subtype, indicating their role as disease-associated immune complexes. Notably, antigen-huIgG4 colocalization was more pronounced in the glomerular urinary space than in the subepithelial podocyte region (Fig. 21C, D, panels 1).

Further analysis of patient biopsies demonstrated the release of huIgG4$^+$ aggregates into the urine, and their uptake along the nephron by distal (dtc) and proximal tubular epithelial cells (ptc). They were also detected adhering to the tubular brush border forming a distinct "starry night" phenotype, a hallmark characteristic of exophers described in *C. elegans* (Fig. 21 C, D, panels 2). These histological findings suggest glomerular release of antigen/autoantibody aggregates into the urine.

To further validate these histological findings, urinary extracellular vesicles from the two MN patient urines were enriched and analyzed by confocal microscopy. Among the isolated uEVs, a subset of large (~5-8 µm) vesicles exhibited strong colocalization of the MN-associated

antigens THSD7A or PLA_2R1 and huIgG4 antibody. Additionally, these vesicles were positive for the extracellular vesicle marker 14-3-3 (Fig. 21C, D, panels 3). These findings suggest that the patient's glomerular huIgG4$^+$ antigen aggregates correspond to MN-associated exopher-like vesicles (huIgG4$^+$ EVs) in the urine.

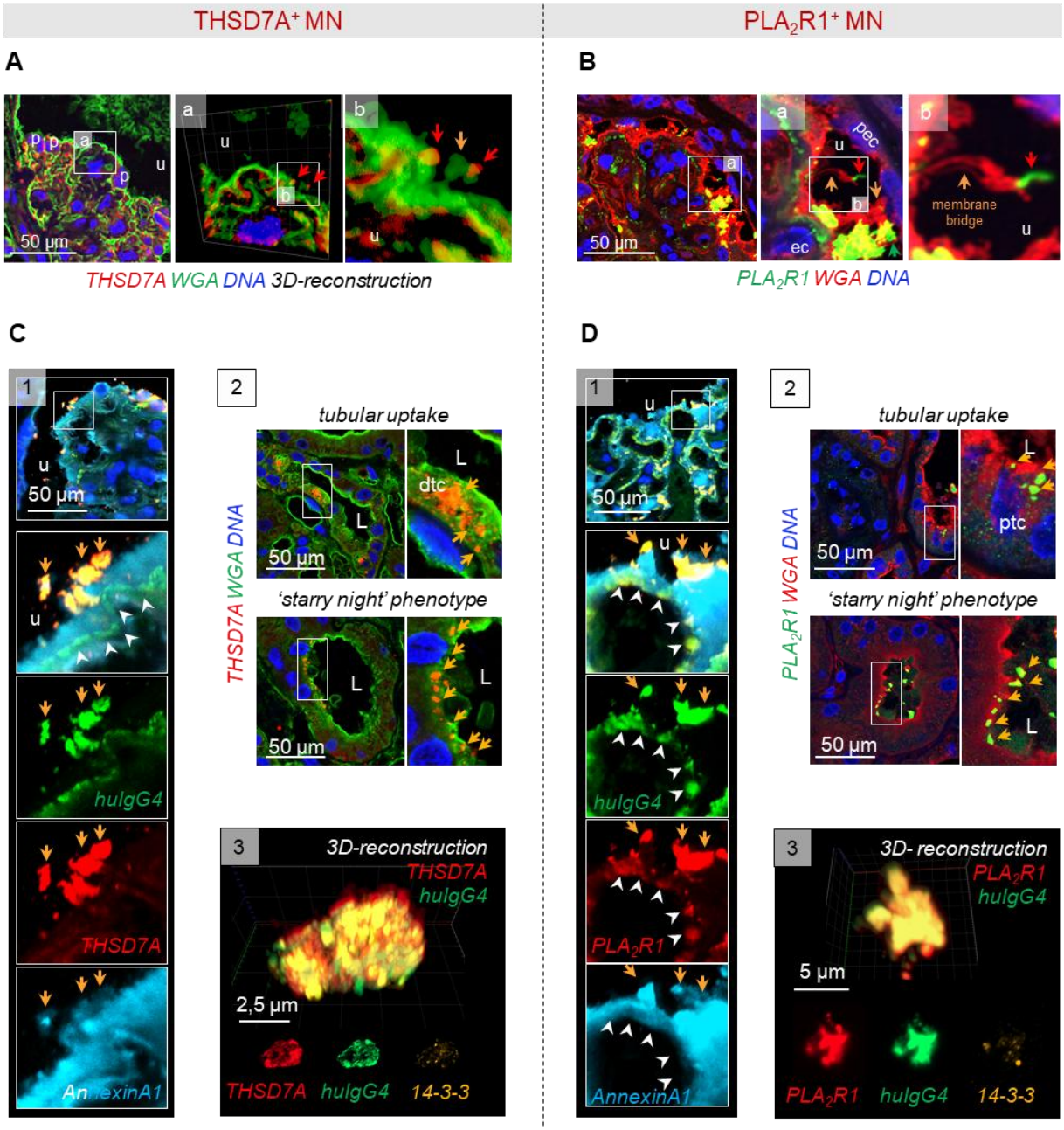

Figure 21: The diagnostic biopsies and urines collected from a THSD7A⁺-MN and PLA₂R1⁺-MN patient were evaluated for the presence of exopher-like vesicles (ELVs). A, B) High-resolution confocal micrographs to the antigens **A)** THSD7A (red), **B)** PLA₂R1 (green) and wheat germ agglutinin (green, WGA, demarcates plasma membrane) and DNA (blue). Urinary space THSD7A and PLA₂R1 aggregates (red arrows) exhibit a WGA⁺ membrane connection (orange arrow) to podocytes (p). **C, D)** Glomerular and urinary **C)** THSD7A⁺ and **D)** PLA₂R1⁺ aggregates are huIgG4⁺. **Panel 1:** Confocal analyses demonstrate that THSD7A (red) colocalizes with huIgG4 (green) in urinary space aggregates (orange arrows). White arrowheads highlight huIgG4 in the subepithelial space. **Panel 2:** Antigen aggregates (orange arrows) are taken up by tubular cells, dtc = distal tubular cell and found within the tubular lumen (L) adherent to the apical membrane as 'starry night' phenotype. **Panel 3:** 3D-reconstructed confocal z-stack of a urinary ELV (from diagnostic urines) stained for antigen (red), huIgG4 (green) and the vesicle marker 14-3-3 (orange). Lower row exhibits individual channels in one plane.

4.3.2 Characterization of MN patient ELVs

ImageStream® analyses of total urinary EVs were performed to investigate the abundance of ELVs (huIgG4$^+$ uEVs) in MN patient compared to healthy control urines. Labeling with Membrite594, a membrane dye used as general EV marker, and huIgG4 antibody revealed that in MN patients ELVs were highly abundant in comparison to healthy urinary EVs, marking them as disease-associated. Approximately 30% of total EVs were huIgG4-positive, compared to only ~2.5% in control urine samples (Fig. 22 A, E).

To characterize these vesicles in greater detail, we developed an immunoprecipitation (IP) method to enrich and isolate ELVs from total urinary EVs. HuIgG4-antibodies were coupled to magnetic beads and total uEVs (input = in) from MN patients and healthy controls were added. After incubation the bead-uEV mixture were separated on a magnet and the supernatant containing not bound uEVs, thus huIgG4-depleted EV fraction (R = rest EVs) was collected, and the bead-bound huIgG4$^+$-enriched EV fraction (E = ELVs) were eluted. The input (I), rest EV (R) and ELV (E) fractions of the huIgG4 IP were further analyzed. Nanoparticle tracking analysis (NTA) revealed that the mean size of enriched ELVs was approximately 580 nm in the THSD7A$^+$-MN patient and 450 nm in the PLA_2R1^+-MN patient (Fig. 22B, F), identifying them as a particularly larger uEV subset. Immunoblot analysis of the IP fractions confirmed the presence of MN-specific antigens and key plasma membrane-derived EV markers, including Annexin A1, 14-3-3, and Flotillin, as well as CD63 and CD9 as endosomal derived EV markers (Fig. 22C, G).

Direct transmission electron microscopy (TEM) with immunogold labeling for huIgG4 identified both small and large EVs with either round or irregular morphology in the huIgG4$^+$ fraction (ELVs) from both MN patients. In contrast, the huIgG4-depleted EV fraction (R = rest EVs) primarily contained non-labeled, small, and regularly shaped vesicles (Fig. 22D, H). These findings strongly suggest that ELVs represent a key pathobiological feature of MN, serving as a mechanism for immune complex clearance. The presence of MN-specific antigen-huIgG4 aggregates within large urinary vesicles, their adherence to tubular structures, and their molecular composition highlight the potential role of exopher-like vesicles in disease progression.

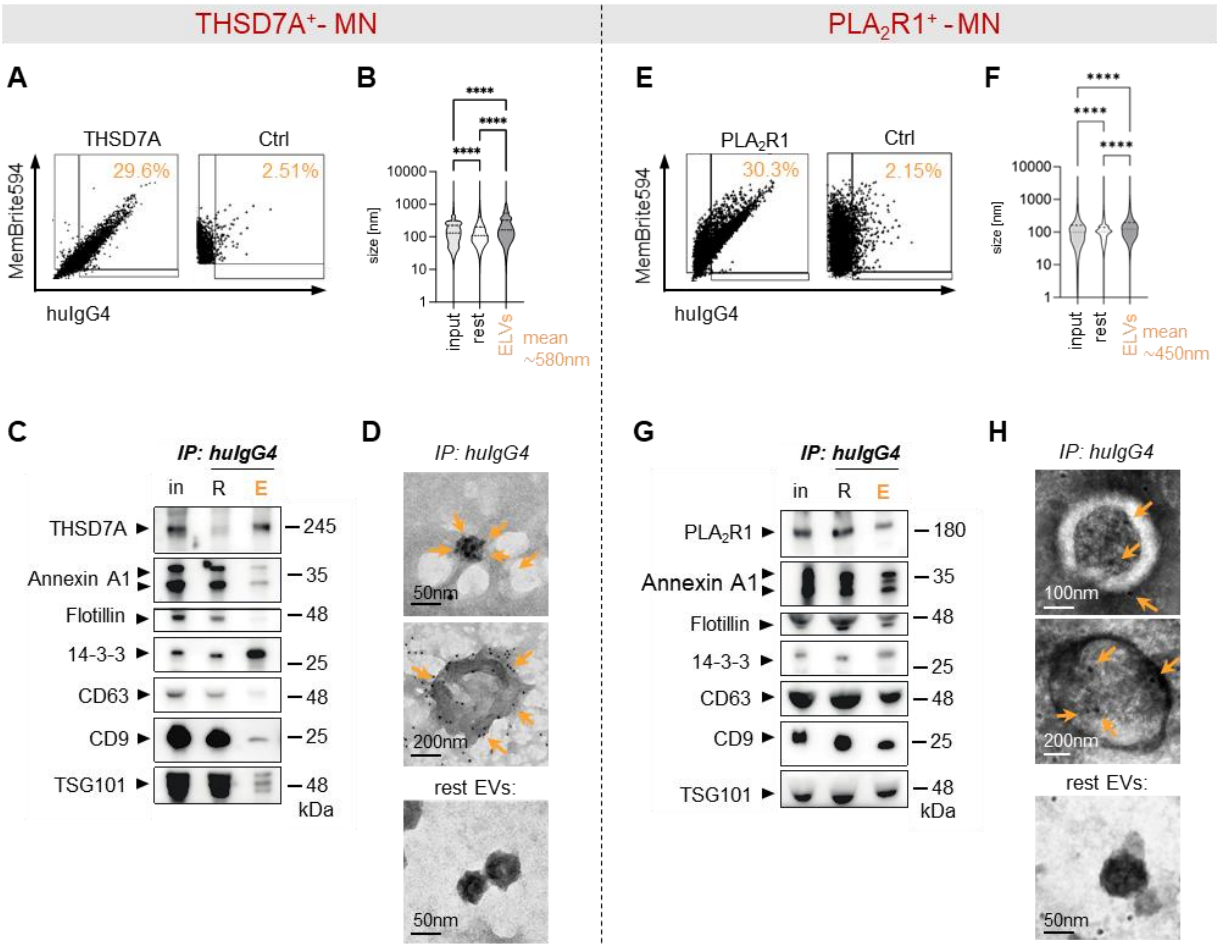

Figure 22: ELV characterization in a THSD7A$^+$ and PLA$_2$R1$^+$-MN patient. A, E) ImageStream® quantification of % urinary ELVs from 10^9 MemBrite594$^+$ EVs in combination with huIgG4 of **A)** THSD7A and **E)** PLA$_2$R1 patient in comparison to healthy control EVs. **B, F)** ELVs (E) from a **B)** THSD7A and **F)** PLA$_2$R1 patient were enriched by huIgG4 pulldown from 10^9 urinary EVs (input = in) and with the rest fraction analyzed for the size distibution by nanoparticle tracking analysis (NTA). **C, G)** ELVs (E) were enriched by huIgG4 pulldown from 10^6 urinary EVs (input = in) and analyzed for the abundance of **C)** THSD7A or **G)** PLA$_2$R1 as MN antigens and of vesicle markers by reducing immunoblot in comparison to the rest EV fraction (R). **D, H)** ELVs (E) of both MN patients were enriched by huIgG4 pulldown from 10^9 urinary EVs. Immunogold TEM to huIgG in the ELV-enriched fractions compared to the respective rest EVs of both patients. Orange arrows point towards specifically bound gold.

4.3.2.1 14-3-3 as a second key marker for huIgG4$^+$ MN-associated ELVs

Strikingly, the immunofluorescence and immunoblot analyses revealed that the 14-3-3 protein was highly abundant and recurrent in ELVs. Given that 14-3-3 has been identified as a key factor in exopher formation in *C. elegans* neurons[212], it was next investigated whether this protein could serve as a reliable marker, alongside huIgG4, for distinguishing our MN-associated ELVs from total uEVs.

To test this, immunoprecipitation of uEVs using either 14-3-3 or huIgG4 antibodies conjugated to beads were conducted from three MN patients and the bead-bound ELV enriched fractions were analyzed via immunoblotting. The protein composition of the 14-3-3 and huIgG4-enriched vesicles was remarkably similar, with both containing an abundance of vesicular, proteasomal, and podocyte-associated proteins (Fig. 23A). Only slight differences in the THSD7A, Nephrin and LMP7 signal could be seen. Furthermore, immunofluorescence imaging demonstrated strong colocalization of 14-3-3 with MN antigen THSD7A and PLA_2R1 aggregates at the podocyte membrane and within the glomerular urinary space (Fig. 23B). Based on these findings, 14-3-3 protein can serve as a robust secondary marker for identifying MN-associated ELVs.

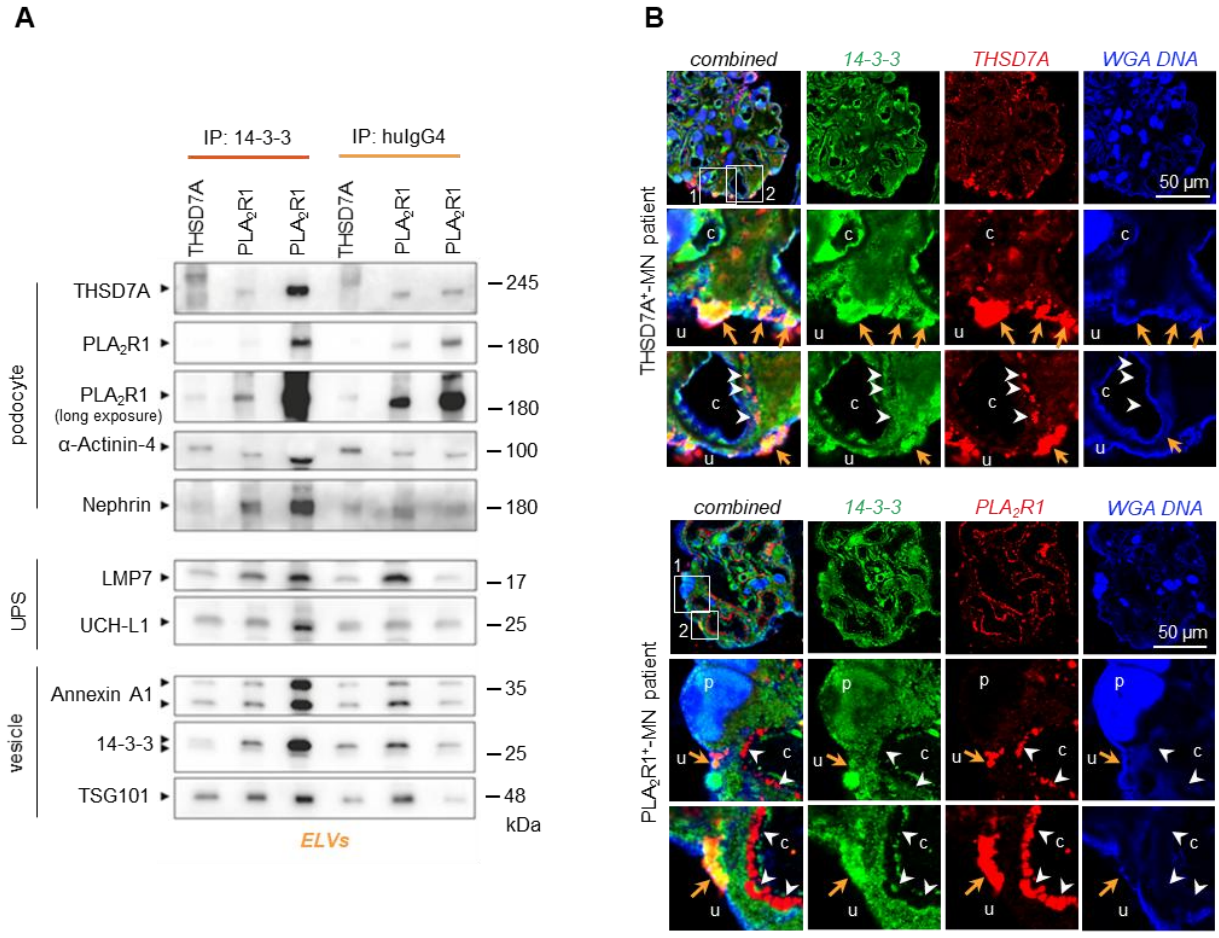

Figure 23: 14-3-3 represents a surrogate marker for huIgG4$^+$-EVs. A) EVs enriched via huIgG4-pulldown or via 14-3-3-pulldown from the urine of 3 MN patients (THSD7A$^+$-MN patient P1 urine collection 4 (U4); PLA_2R1^+-MN patients P4 and P11) were compared for the abundance of podocyte proteins, proteasomal proteins and vesicular marker proteins. In both cases, 10^4 total particles from the pulldowns were loaded. Note the comparable protein abundance in individual patients within the huIgG4$^+$ EV fraction and 14-3-3$^+$ EV fraction with slight differences for THSD7A, Nephrin and LMP7. **B)** Confocal analyses of the subcellular localization of 14-3-3 (green) in relation to the MN antigens (red) and the plasma membrane (Wheat germ agglutinin WGA, dark blue), DNA (dark blue) in the diagnostic biopsy of a THSD7A$^+$- and PLA_2R1^+-MN patient. Note the strong co-localization of 14-3-3 with urinary side antigen aggregates in both patients (orange arrows). White arrowheads = subepithelial aggregates; c = capillary lumen, u = glomerular urinary space, p = podocyte nucleus.

4.3.2.2 MN-associated ELVs exhibit unique characteristics distinguishing them from nephrotic non-MN patient uEVs

To determine whether the ELVs identified in THSD7A$^+$- and PLA$_2$R1$^+$-MN patients are unique to MN or shared across other nephrotic conditions, they were compared to urinary extracellular vesicles (uEVs) from nephrotic non-MN patients. The study included a second follow-up urine sample from the THSD7A$^+$-MN patient, two additional PLA$_2$R1$^+$-MN patients, and nephrotic patients diagnosed with Minimal change disease (MCD), primary focal segmental glomerulosclerosis (FSGS), IgA nephritis (IgAN), and tubulo-toxic kidney injury.

Total uEVs were isolated from all patient groups and analyzed by immunofluorescence and ImageStream® for their vesicular characteristics (Fig. 24A). Staining against the general EV marker Membrite594, the proposed ELV markers huIgG4 and 14-3-3, and plasma membrane-derived EV markers such as Annexin A1 and CD63/81 were performed. Both analyses confirmed successful isolation of uEVs in all patient groups. Immunofluorescence staining revealed distinct differences in vesicle marker distribution, suggesting variations in cellular origin or release mechanisms. Especially the plasma membrane associated protein Annexin A1 were more abundant in the MN patients compared to non-MN patient, as well as the presence of 14-3-3 protein that was stronger in the MN and MCD patient uEVs. Notably, the surface pattern of 14-3-3 and huIgG4 differed between MN and nephrotic non-MN patients, with MN patients exhibiting a more and larger aggregate-like pattern. ImageStream® analyses supported this observation as the abundance of huIgG4$^+$/14-3-3$^+$ EVs as percent of total uEVs varied among patient groups. While nephrotic primary FSGS (1.22%), IgAN (5.8%) and tubulo-toxic kidney injury (0.64%) patients exhibited a low percentage, the THSD7A$^+$-MN (35.4%) and PLA$_2$R1$^+$-MN (12.56%), as well as the MCD (25.8%) patient had a higher percentage of huIgG4$^+$/14-3-3$^+$ EVs.

4.3.3 Disease-causing autoantibodies are bound to ELVs

To determine whether the huIgG4 bound to the ELVs represents the pathogenic MN-associated autoantibody a protocol to elute the antibodies from the enriched urinary patient ELVs was developed. The eluted antibodies were then used as primary antibodies in subsequent immunoblot analyses of human glomerular lysates and lysates from HEK cells overexpressing THSD7A or PLA$_2$R1. Binding of eluted antibodies to the respective antigen was visualized by probing with a secondary HRP-coupled anti-huIgG4 antibody. Immunoblots incubated with immunoglobulins eluted from huIgG4$^+$ EVs of THSD7A- or PLA$_2$R1-associated MN patients showed a strong reactivity to THSD7A or PLA$_2$R1 proteins in both glomerular and HEK cells lysates, confirming their identity as pathogenic MN autoantibodies bound to urinary ELVs (Fig. 24B). In contrast, antibodies eluted from huIgG4$^+$ EVs of nephrotic non-MN patients

showed no specific reactivity to either human glomerular proteins or to HEK cell-expressed THSD7A or PLA_2R1 proteins (Fig. 24B).

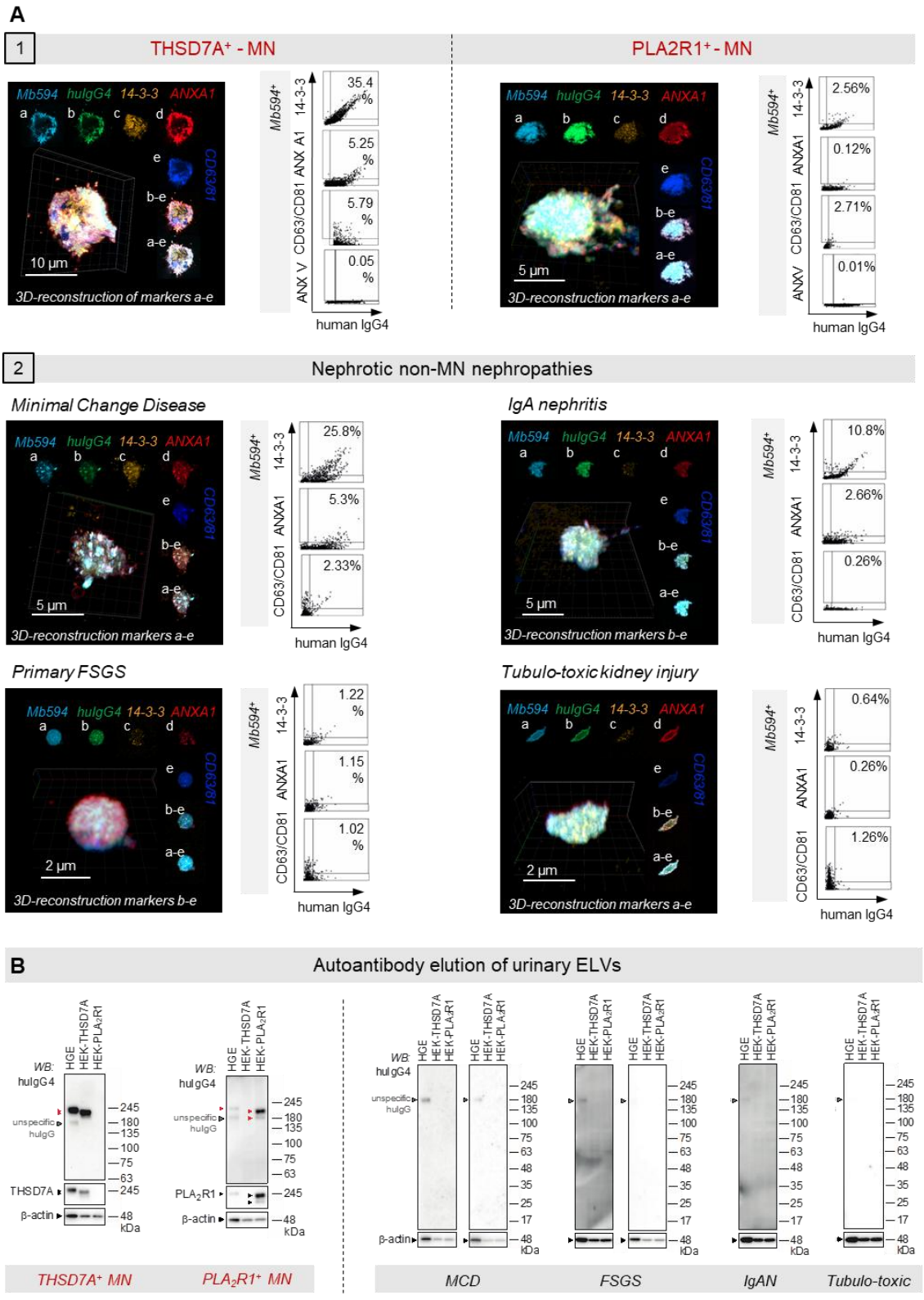

Figure 24: Comparison of urinary EV fractions in MN versus nephrotic non-MN patients. The urinary EVs from nephrotic urines of THSD7A$^+$ and PLA$_2$R1$^+$-MN, Minimal Change Disease (MCD), primary FSGS, IgA nephritis (IgAN) and tubulo-toxic kidney injury patients were characterized. **A) Panel 1:** Vesicle Marker Expression. 3D-reconstructed confocal z-stack of an ELV demonstrates the expression of key vesicle markers: 14-3-3 (orange), Annexin A1 (red), CD63/CD81 (blue), and MemBrite594 (light blue) marking the plasma membrane. The huIgG4 antibody is indicated in green. Individual channels in one plane (a-e) are displayed for clarity. **Panel 2:** Quantification of marker distribution by Image Stream analysis on MemBrite594$^+$ huIgG4$^+$ EVs. In the MCD and IgAN patients, 14-3-3 was identified as an abundant marker, whereas it was absent in the primary FSGS and tubulo-toxic patient samples. **B)** Antibodies eluted from the patient ELVs were tested for reactivity against proteins present in human glomerular extract (HGE) and HEK cells transfected with PLA$_2$R1 or THSD7A.

4.3.4 Podocyte-specific markers and higher UPS protein abundance in ELVs from MN patients compared to non-MN patients

Further immunoblotting analyses of huIgG4⁺ EVs from MN patients revealed the presence of vesicular proteins such as 14-3-3, Annexin A1, CD63/81, Flotillin, and TSG101, (Fig. 25A, B, panels 1), corroborating the findings observed in ImageStream® analysis. Immunoblot (Fig. 25A, B, panels 1) and immunofluorescence (Fig. 25A,B, panels 2) assays also revealed the abundant expression of podocyte proteins, including THSD7A, PLA_2R1, Nephrin, Podocin and α-Actinin 4, with notable presence exclusively in THSD7A⁺- and PLA_2R1^+-MN patients, compared to non-MN controls. While huIgG4⁺-EVs from nephrotic non-MN patients contained few or no podocyte proteins, the huIgG4⁺-EVs from MCD patients displayed significant amounts of Nephrin. Overall these findings strongly support the hypothesis that in MN, podocytes release specific antigen⁺/autoantibody⁺ EVs.

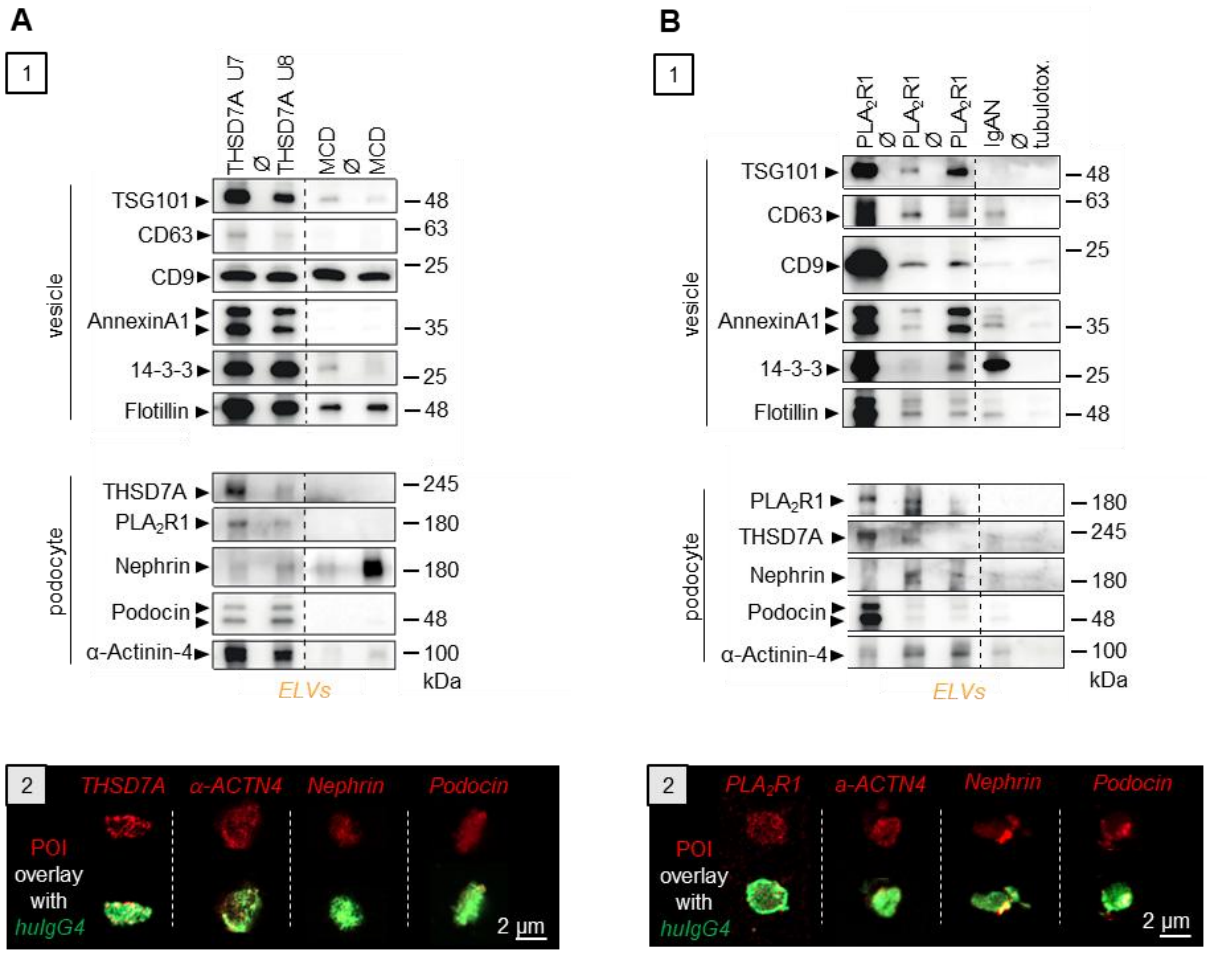

Figure 25: ELVs from MN patients carry podocyte proteins. A, B) Panel 1: Immunoblot analysis to vesicle markers and podocyte specific proteins in enriched ELVs via huIgG4 immunoprecipitation from **A)** THSD7A⁺-MN urines U7 and U8 in comparison to two nephrotic minimal change disease (MCD) patients and from **B)** the diagnostic urines of the 3 PLA_2R1^+-MN patients in comparison to a nephrotic IgAN patient and the tubulo-toxic kidney injury patient. **Panel 2:** Confocal analyses demonstrate expression of podocyte-specific proteins (protein of interest (POI) in red) within huIgG4⁺ (green) ELVs of the **A)** THSD7A and **B)** PLA_2R1 patients.

Additionally, reflecting the experimental mouse data, which indicated an increase in proteins associated with the ubiquitin-proteasome system in THSD7A^{+}-MN mice, the UPS-related content of ELVs in MN patients was investigated. Interestingly, high levels of K48-polyubiquitinated proteins (indicating proteasomal substrates), UCH-L1 (a deubiquitinating enzyme, upregulated in MN), and the immunoproteasome subunit LMP7 were found in ELVs isolated from five MN patient urines. Along with UPS proteins, disease-associated markers such as complement components (C1q, C5b9), mitochondrial proteins (Mitofusin 2, ATPB), and lysosomal membrane proteins (LIMP2, LAMP2) were also detected in these vesicles by immunoblot (Fig. 26A, B, panels 1) and immunofluorescence (Fig. 26A, B, panels 2). In contrast, huIgG4^{+}-EVs from nephrotic non-MN patients displayed significantly lower levels of these disease-associated proteins, albeit the same amounts of vesicles were loaded.

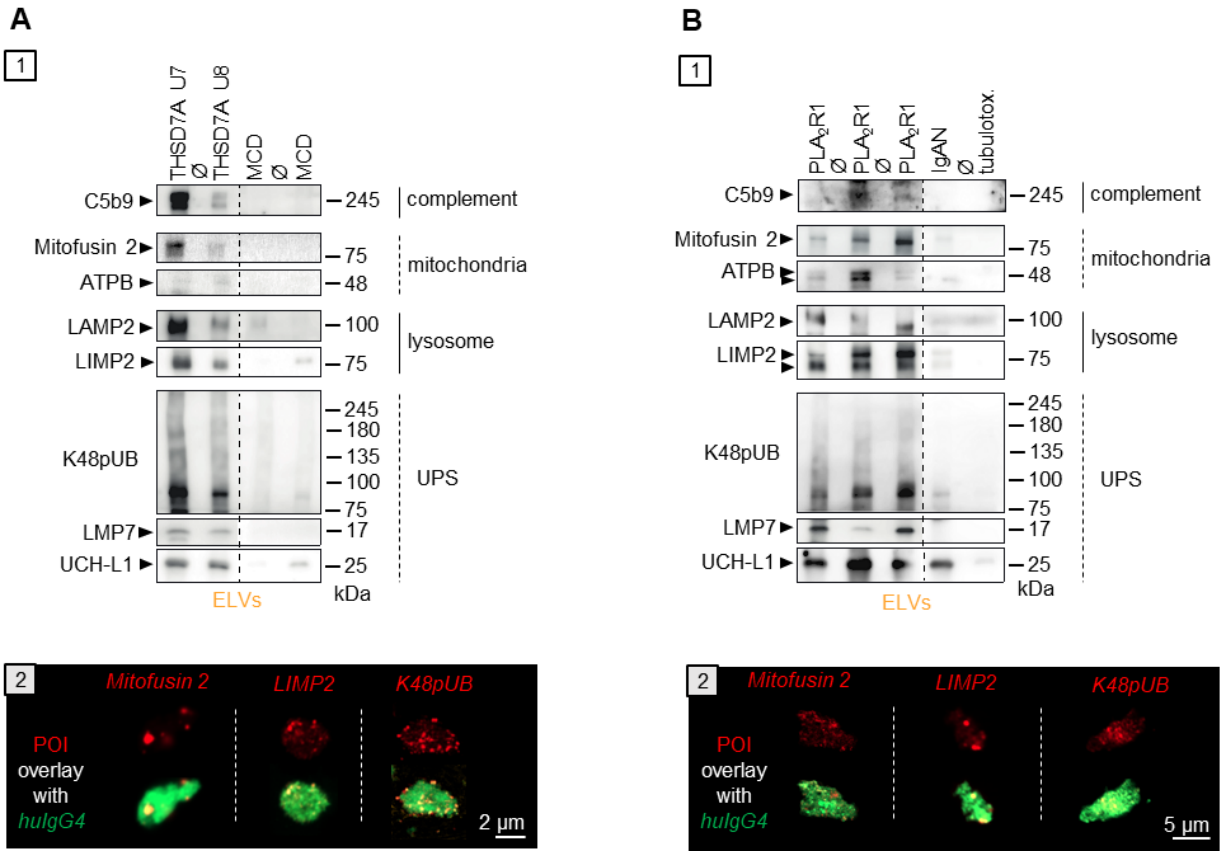

Figure 26: Urinary ELVs enriched from urines of THSD7A$^+$- and PLA$_2$R1$^+$-MN patients contain disease-associated proteins. Urinary ELVs enriched from diagnostic urine samples of a THSD7A$^+$- and three PLA$_2$R1$^+$-MN patients were analyzed in comparison to MCD, IgAN and tubulo-toxic injury patients for the presence of disease-associated proteins. **A**) Immunoblot detection of disease-associated proteins belonging to the complement cascade (C5b9, membrane attack complex), mitochondria (membrane proteins Mitofusin 2 and ATP synthase ATPB), lysosomes (membrane proteins LAMP2 and LIMP2), and the ubiquitin proteasome system (UPS: K48-polyubiquitinated proteins, the proteolytic β-subunit LMP7, the deubiquitinating enzyme UCH-L1) in enriched ELVs from the diagnostic urines of the 4 MN patients in comparison to the nephrotic non-MN patients. **B**) Confocal analyses demonstrate expression of Mitofusin 2, LIMP2, or K48pUB (all proteins of interest (POI) in red) within urinary huIgG4$^+$ (green) ELVs of the THSD7A$^+$ and PLA$_2$R1$^+$-MN patients.

So far, the investigations identified glomerular antigen$^+$/autoantibody$^+$ aggregrates at the urinary podocyte membrane in THSD7A$^+$- and PLA$_2$R1$^+$-MN patients, which are released and reuptaken along the nephron or excreted within the urine as ELVs containing podocyte and disease-associated proteins and the disease-causing autoantibodies. The urinary ELVs identified in MN-patients were unique in respect to their appearance and content compared to urinary huIgG4$^+$-EVs from nephrotic non-MN patients.

4.4 Non-invasive ELV monitoring in MN patients

4.4.1 ELV release in a relapsing THSD7A$^+$-MN patient

Since ELVs are released through the urine, this provides an easily accessible material for a non-invasive molecular analysis of patients for diagnostic and prognostic approaches or longitudinal disease monitoring. In this study a prospective analysis to monitor the release of ELVs in a 62-year-old male THSD7A$^+$-MN patient was conducted over 2.5 years, providing insight into the potential of ELVs for non-invasive molecular analyses. At his initial clinical visit, the patient presented with severe nephrotic syndrome, marked by edema, significant weight gain (5 kg), elevated serum lipids (triglycerides 310 mg/dL, cholesterol 442 mg/dL), and a decreased serum albumin (12.4 g/L). Urine analysis revealed massive proteinuria (14852 g/L), although renal function remained normal (creatinine 0.8 mg/dL, BUN 54 mg/dL, eGFR >90 ml/min). A kidney biopsy was performed, confirming a diagnosis of THSD7A$^+$-MN (stage 1 Ehrenreich and Churg), showing glomerular thickening and fine glomerular positivity for huIgG4 (Fig. 27, panel 3) and THSD7A aggregates (Fig. 27, panel 4), which were located in the subepithelial space, but much more prominent in the urinary space (orange arrows) and to a much lesser extent also inside parietal epithelial cells (red arrows). Additionally, ultrastructural analysis confirmed the GBM thickening and foot processes effacement and revealed formation of long membrane extensions derived from major and foot processes (Fig. 27, panel 5 white arrows).

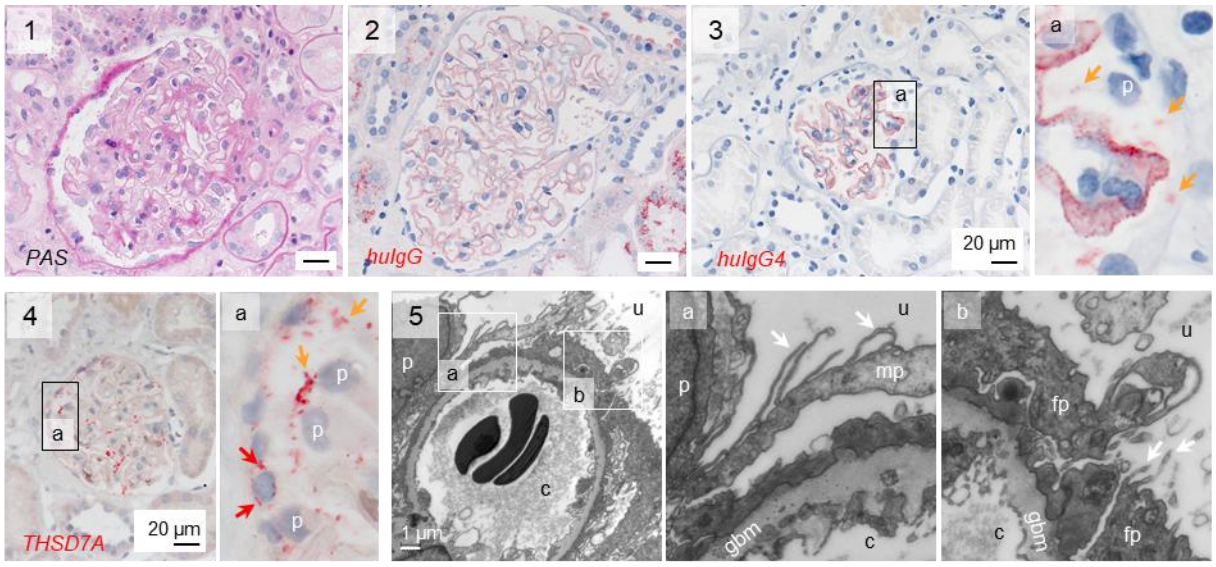

Figure 27: Nephropathological diagnosis of the THSD7A$^+$-MN patient. Micrographs from the nephropathological diagnosis (19/05/2021) of the patient encompassing light microscopy with **panel 1:** PAS staining for general morphology; immunohistochemistry to **panel 2**: huIgG, **panel 3:** huIgG4, and **panel 4:** THSD7A. Orange arrows highlight aggregates within the urinary space, red arrows show aggregates within parietal epithelial cells. **Panel 5:** Transmission EM; white arrows highlight membrane extensions from major (**panel 5a**) and FPs (**panel 5b**), p = podocyte, gbm = glomerular basement membrane, fp = foot process, mp = major process, u = urinary space, c = capillary space.

The patient was immediately started on the treatment for MN but despite multiple immunosuppressive treatment regimens, including rituximab and cyclophosphamide, the patient experienced a progressive decline in renal function (eGFR 33 ml/min, KDIGO G4A3 in 01/2023), accompanied by episodes of cerebral infarctions (09/2021 and 10/2022) and symptomatic COVID-19 infection. The clinical course, along with serum THSD7A autoantibody (sTHSD7A-ab) titers (red line) and proteinuria (blue line), is shown in Fig. 28. Treatment timepoints are indicated with black arrows and a significant increase of B-cells, as the autoantibody-producing cells, is highlighted by a green arrow. The clinical course was typical for a therapy resistant neprotic syndrome. To investigate whether urinary ELV release dynamics mirrored the patient's clinical course and could explain therapy resistance, ELVs were analyzed from the patient's urine at multiple time points during disease progression.

ELV abundance was assessed using ImageStream®, immunoblotting for huIgG4, and mass spectrometry to profile the ELV proteome and affected signaling pathways in injured podocytes. We collected urine samples over 2.5 years, including the diagnostic urine (U1) and seven additional samples (U2-U8), collecting dates are indicated in yellow within the timeline. Notably, ImageStream® analysis revealed a progressive decrease in urinary ELV release, even when serum THSD7A autoantibody titers remained high during the first three urine collections (U1-U3) (Fig. 28 panel 1). Albeit sTHSD7A-ab titers of 1:160 in U1-U3, the percentage of released ELVs within 10^9 total EVs dropped from ~35% in the diagnostic U1 urine (05/2021) within 1.5 years to ~3% in U3 (10/2022), but the patient still showed heavy symptoms with edema and high proteinuria of ~20 g/g creatinine. From early 2023 onward, with renewed rituximab treatment, the patient was negative for serum THSD7A-abs, proteinuria decreased, and ELV release remained low (<1%) with a slight increase to ~4% at U7 (June 2023), coinciding with a recovery of $CD19^+$ B-cells (2%; 14/µl) (Fig. 28, panel 1).

ELV-bound antibodies from each urine sample were eluted to search for the presence of huIgG4 anti-THSD7A autoantibodies (Fig. 28 panel 2) by immunoblot analysis. Human podocyte mock (THSD7A negative) cells and THSD7A overexpressing cell lysates were used as samples to confirm the presence of autoantibodies. Surprisingly, immunoblotting revealed detection of THSD7A protein using the eluted antibodies from all urine samples, even when the patient's serum THSD7A-abs were negative in U4 and U6-U8 (Fig. 28 panel 2).

In the proteomic analysis, key pathways supporting our hypothesis that podocyte ELV formation is induced in stressed podocytes upon autoantibody binding in membranous nephropathy were investigated. The Fig. 28 panel 3 presents a selection of relevant pathways based on proteins identified in ELV fractions, with the total number of proteins (N) detected across all eight urine samples. Only proteins identified with at least two peptides and a Q-value < 0.001 were included in the analysis. P-values indicate the statistical significance of pathway enrichment for selected functions. Circles represent identified proteins assigned to each

category, along with the number of proteins annotated within that category (recall rate). The analysis strongly confirmed the vesicular origin of these ELVs, as evidenced by the enrichment of extracellular vesicle markers, vesicular lumen proteins, and plasma membrane-associated proteins in all eight urine samples. Further, disease-associated pathways (highlighted in ochre) were examined and observed a substantial presence of immunoglobulin complex proteins in the ELV fractions. Additionally, numerous proteins linked to cellular stress responses, such as heat shock proteins and chaperones, as well as components of the classical complement system and proteolytic pathways (lysosome and proteasome) were identified. Notably, ubiquitins, proteasomal subunits, and UCH-L1 were detected, aligning with the previous described findings of increased proteasomal protein abundance in THSD7A^{+}-MN mice and MN patients (see Figs. 12 and 26).

Supporting the notion of vesicle formation from podocytes, the analysis revealed proteins involved in actin cytoskeletal regulation—particularly those driving filopodia formation (e.g., CD15[214], Filamin A, B, C, Arp2/3), as well as proteins related to cell-cell interactions and podocyte-specific markers such as THSD7A, Podocin, and Podocalyxin. In summary, the proteome of the eight urine samples exhibited a similar pattern, with only minor variations in protein distribution or abundance across related pathways. The proteomic study revealed a compelling molecular signature of podocyte injury, captured in ELVs released into the urine of the THSD7A^{+}-MN patient over the disease course.

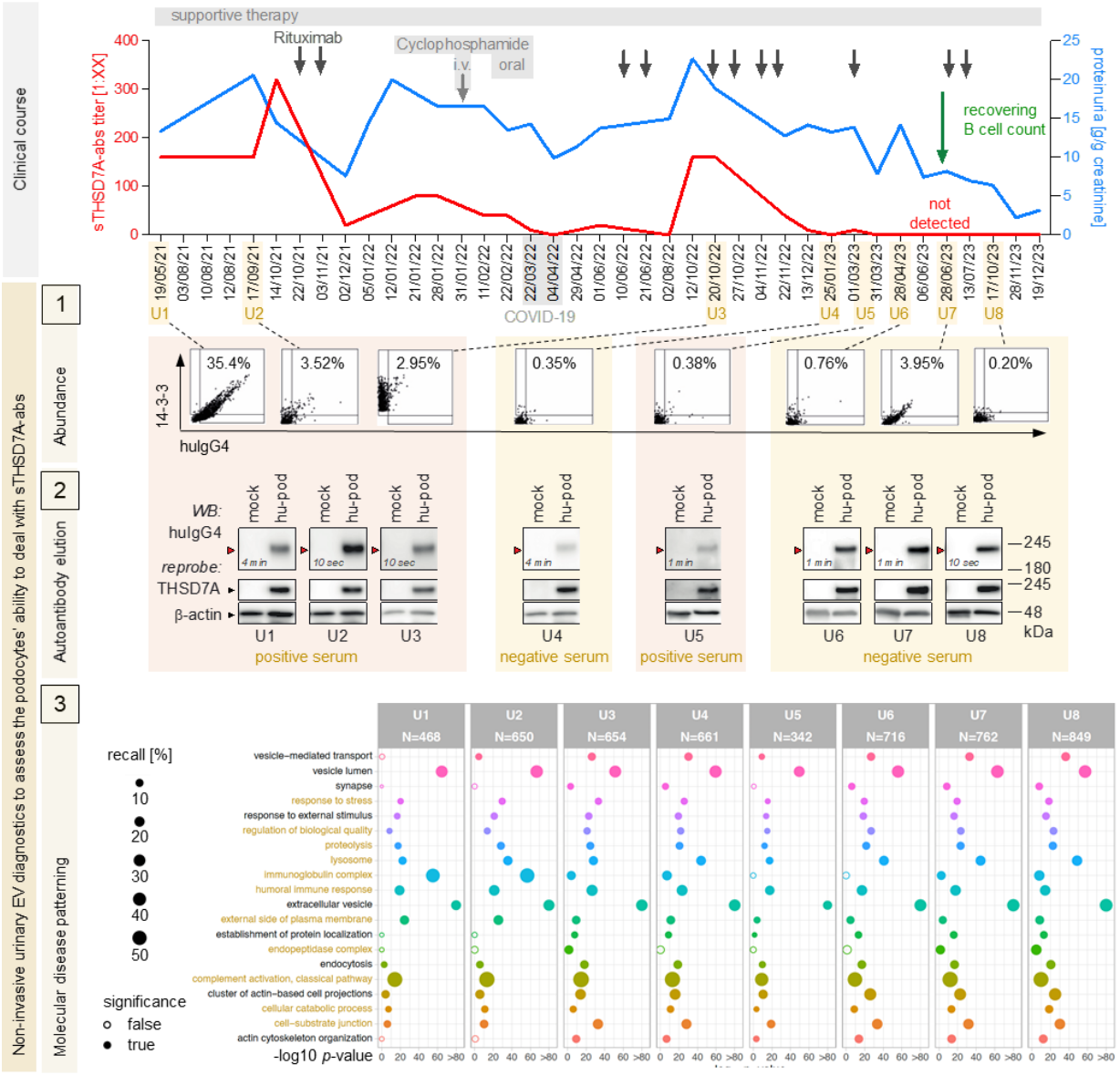

Figure 28: Longitudinal analysis of urinary ELV release and its characteristics over 2.5 years in a THSD7A$^+$-MN patient. The graph illustrates serum THSD7A autoantibody titers (red curve, left y-axis) and the urinary protein-to-creatinine ratio (blue curve, right y-axis). Key clinical interventions and the occurrence of a COVID-19 infection are annotated. **Panel 1:** ImageStream® plots display the proportion of huIgG4$^+$ and 14-3-3$^+$ ELVs in urine, expressed as a percentage of ELVs among 10^9 total extracellular vesicles (EVs). **Panel 2:** Reactivity analysis of huIgG4 antibodies eluted from 10^9 ELVs against THSD7A protein. "hu-pod" represents human podocytes overexpressing THSD7A, while "mock" denotes podocytes without THSD7A expression. Membranes were reprobed for THSD7A and β-actin to verify expression levels and protein loading. The exposure times for the huIgG4 signal are specified, with all blots derived from a single membrane exposed simultaneously. Notably, THSD7A autoantibodies bound to ELVs were consistently detected in urine samples, despite a negative sTHSD7A autoantibody titer. **Panel 3:** Proteomic molecular disease patterning of ELVs isolated from U1-U8. For pathway analysis, only proteins identified with ≥ 2 peptides with a Q-value < 0.001 were used. Graph displays the p-values corresponding to the significance of pathway enrichment of selected functions. P-values below 1E-80 were capped; recall rate = proteins identified and assigned to category / number of proteins that are annotated to the category. Pathways reflecting ELV-specific processes are highlighted in ochre. Clinical data of the THSD7A$^+$-MN patient is provided in table S1. A total list of identified proteins can be found on PRIDE (see method section for details).

4.4.2 Prospectively analysis of a PLA_2R1^+-MN patient with a remitting disease course

A second MN patient was prospectively evaluated, who showed a remitting disease course in comparison to the relapsing $THSD7A^+$-MN patient. This 20-year-old female was diagnosed with PLA_2R1^+-MN (stage I-III, Ehrenreich and Churg) in October 2021. Diagnosis was established using the current gold standard diagnostic nephropathologic analysis and confirmation of the presence of serum PLA_2R1 antibodies ($sPLA_2R1$-abs). Her clinical course over two years is shown in Fig. 29. The x-axis marks the time points of clinical blood and urine assessments, while the left y-axis represents serum PLA_2R1 antibody titers in relative units (RE)/ml (red line). Proteinuria (g/g creatinine) is depicted as a blue line over the disease course. At diagnosis (10/2021), the patient presented with edema and severe proteinuria (~14 g/g creatinine), comparable to the $THSD7A^+$-MN patient. Initial serum analysis showed a PLA_2R1-ab titer of 92 RE/ml, which increased over time, peaking at ~140 RE/ml in January 2022. Interestingly, despite this rise, proteinuria had already started to decrease (~8 g/g creatinine).

Treatment with cyclosporin A was initiated, leading to a rapid decline in $sPLA_2R1$-abs (~10 RE/ml by April 2022) and a further reduction in protein loss (~3 g/g creatinine). However, a slight increase in serum PLA_2R1-ab titers was observed one month later, prompting two rounds of rituximab treatment. This intervention resulted in a sustained negative serum antibody titer from August 2022 onward, along with stabilized proteinuria (~2 g/g creatinine), achieving clinical remission.

To further investigate ELV abundance and autoantibody presence, ImageStream® analysis and immunoblot detection were performed, following the same approach used for the $THSD7A^+$-MN patient. Diagnostic urine collected in October 2021 was used to isolate total EVs, revealing an ELV abundance of ~9%, marked by huIgG4 and 14-3-3 proteins. Immunoblot analysis also confirmed the presence of PLA_2R1 autoantibodies in eluted ELVs. However, in a follow-up urine sample collected two years later (10/2023), ELVs accounted for only ~0.7% of total EVs, and no bound PLA_2R1 autoantibodies were detectable by immunoblot, strongly supporting the patient's immunologic remission, as reflected by the negative serum PLA_2R1-ab titer.

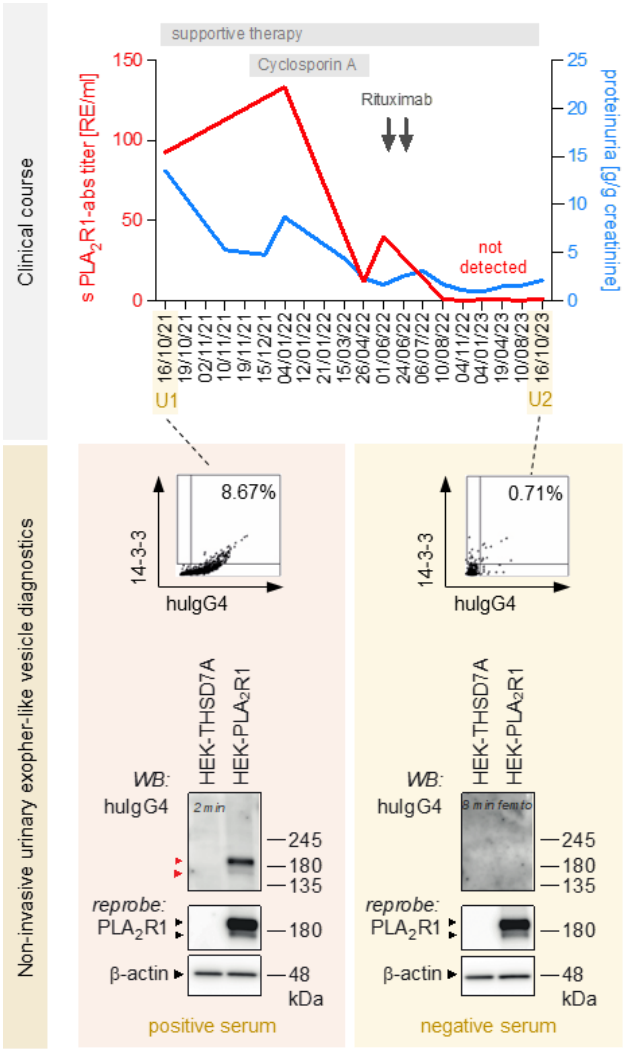

Figure 29: Longitudinal analysis of a 22-year-old female patient with PLA_2R1^+-MN. The graph illustrates the patient's clinical course, diagnosed on 16/10/2021, specifically tracking serum PLA_2R1 autoantibody titers (red curve; left y-axis) and the urinary protein-to-creatinine ratio (blue curve; right y-axis). Key clinical interventions are marked along the timeline. Diagnostic (U1) and follow-up (U2) urine samples were collected for further analysis. Image Stream analysis quantifies the percentage of $huIgG4^{+}/14\text{-}3\text{-}3^{+}$ ELVs within 10^9 $MB594^{+}$ urinary EVs. Immunoblotting assesses the specific reactivity of ELV-eluted huIgG4 against $huPLA_2R1$ or huTHSD7A in HEK cell lysates. Reprobes confirm PLA_2R1 expression and loading control, with exposure times for the huIgG4 signal noted. Notably, PLA_2R1 autoantibodies are clearly detected in U1 but are absent in U2. Clinical data of the patient is provided in table S1.

To summarize, the comparative monitoring of these two MN patients, each with distinct disease trajectories, treatment responses, and outcomes, supports the following key insights: 1) elimination of autoantibodies from the serum and glomeruli via ELV formation and release may influence the disease course, 2) ELV enrichment is a highly sensitive and non-invasive approach for detecting and monitoring MN autoantibodies and 3) enriched ELVs hold great potential as a valuable biological resource for podocyte molecular analyses.

4.4.3 Urine-based ELV autoantibody detection improves sensitivity and accuracy in MN diagnostics

The consistent detection of ELV-bound autoantibodies in the urine of our longitudinally studied patients prompted us to explore their potential as a non-invasive diagnostic tool for membranous nephropathy, particularly in cases where serum autoantibody titers are negative. To evaluate this approach, we analyzed nephrotic urine samples from a prospectively collected cohort of 18 MN patients, whose diagnoses were confirmed through clinical assessments and detailed nephropathological analyses.

For each patient, ELV fractions were isolated from urine, and eluted autoantibodies were used as primary antibodies in immunoblots to detect HEK cell-expressed THSD7A or PLA_2R1 proteins. The heatmap in Fig. 30 panel 1 visualizes the positivity (red) and negativity (blue) of the 18 patients across the two current 'gold standard' diagnostic methods, the antigen accumulation in kidney biopsy samples and proof of serum autoantibody titers.

According to the heatmap, 11 patients were diagnosed with PLA_2R1^+-associated MN, while one patient (P1) presented with $THSD7A^+$-MN and another (P18) was identified with $Nell1^+$-associated MN. The remaining five patients (P13–P17) were categorized as PLA_2R1- and THSD7A-negative MN due to the absence of serum autoantibody titers and a lack of enhanced glomerular antigen expression in their kidney biopsies.

Among the 12 patients classified as having 'expected' antibody profiles, serum autoantibodies for PLA_2R1 or THSD7A were detectable in nine. However, three patients (P13–P15) were serum-negative despite showing enhanced PLA_2R1 expression in their kidney biopsies, suggesting local autoantibody retention within the glomerulus, a phenomenon which is described as a "glomerular autoantibody sink"[215, 216]. This mechanism may explain why certain autoantibodies remain undetectable in the bloodstream while still contributing to disease pathology.

The most striking finding came from the non-invasive ELV autoantibody detection assay. When ELV eluted autoantibodies applied to immunoblot analyses, all 12 patients with expected antibody profiles, including the three who were serum-negative, tested positive for autoantibodies (Fig. 30 panel 2). This demonstrates the high sensitivity of ELV-bound autoantibody detection compared to the traditional pathological and serum-based methods. Furthermore, among the five patients initially classified as PLA_2R1- and THSD7A-negative MN, three (P13–P15) displayed detectable levels of ELV-bound PLA_2R1 autoantibodies in their urine, as confirmed by immunoblotting. This highlights the potential of exopher-like vesicle-based assays to uncover previously undiagnosed cases of PLA_2R1-associated MN.

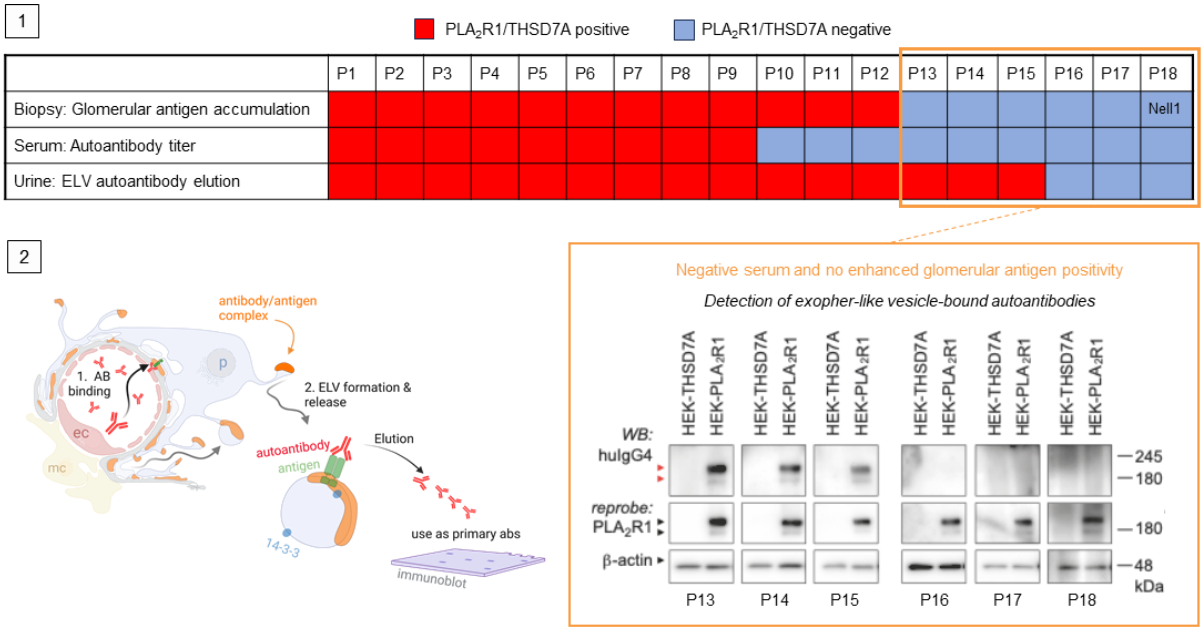

Figure 30: Detection of ELV-bound autoantibodies in 18 prospectively collected urine samples from nephrotic patients with MN. Panel 1: A heatmap visualizing glomerular PLA_2R1/THSD7A positivity and serum PLA_2R1/THSD7A autoantibody presence at diagnosis. Red boxes denote positive findings, while blue boxes indicate negative results. **Panel 2:** Schematic overview of basic podocyte ELV formation and autoantibody elution for non-invasive immunoblot detection. Scheme created with Biorender. Immunoblot assessment showing ELV-eluted autoantibodies targeting PLA_2R1 or THSD7A (red box = present, blue box = absent). Three patients (P13, P14, P15) displayed ELV-bound anti-PLA_2R1 autoantibodies despite negative PLA_2R1 results in standard diagnostic assays.

The findings from longitudinal and prospective studies provide compelling evidence that urine-based detection of ELV-bound autoantibodies represents a powerful and non-invasive diagnostic and potentially prognostic tool for membranous nephropathy. This method significantly improves the sensitivity of MN diagnosis, especially in cases where serum autoantibodies are undetectable or when traditional diagnostic approaches fail to provide clear results. By directly tracking the presence of pathogenic autoantibodies in urine, it's possible to gain a more accurate and dynamic assessment of immunologic disease activity in real-time.

Building on the described findings, a novel vesicle-associated pathomechanism in MN is proposed, centered on the controlled formation and release of podocyte-derived exopher-like vesicles (ELVs) in response to circulating autoantibody binding and antigen accumulation at the podocyte plasma membrane. This process plays a crucial role in reducing glomerular antigen and autoantibody burden.

As summarized in Fig. 31, urinary space antigen/autoantibody aggregates (orange arrows in panel 1) that are found in glomeruli of $THSD7A^+$- and PLA_2R1^+-MN patient biopsies in comparison to a healthy control, are released in exopher-like vesicles. The glomerular autoantibody burden is displayed by Fig. 31 panel 2: (1) the extent of circulating autoantibody binding to subepithelial THSD7A and (2) the podocyte's ability to clear these immune complexes via ELV formation and (3) ELV release into urine. Released ELVs contain antigen-bound autoantibodies, 14-3-3 as an EV marker, disease-associated proteins, mitochondrial

and lysosomal proteins, as well as proteins of the degradative machinery and (4) ELVs may be taken up by nephron cells or excreted within the urine. Mechanistically, ELV formation displaces autoantibody-bound antigens from the subepithelial space to the apical membranes of podocyte foot processes and cell bodies (Fig. 31, panels 3 and 4). This process begins with autoantibody binding to an antigen like THSD7A at the podocytes foot processes (1). THSD7A/autoantibody complexes either accumulate subepithelially (2a, classical model, black arrowheads in immunogold EM images) or translocate toward the urinary side via ELV formation (2b, the new proposed model of this study, orange arrows). The ELVs extend as stalked vesicles (2c) (Fig. 31, panel 4).

From the obtained results it can be proposed that ELVs released into the urine correlate with the antigen/autoantibody aggregates observed in glomeruli. This process helps to clear the glomerular immune complex load, and appears to be a protective response in MN. By monitoring the release and fate of these exopher-like vesicles, a more accurate tracking of MN disease activity, especially in cases with negative serum autoantibody titers can be achieved.

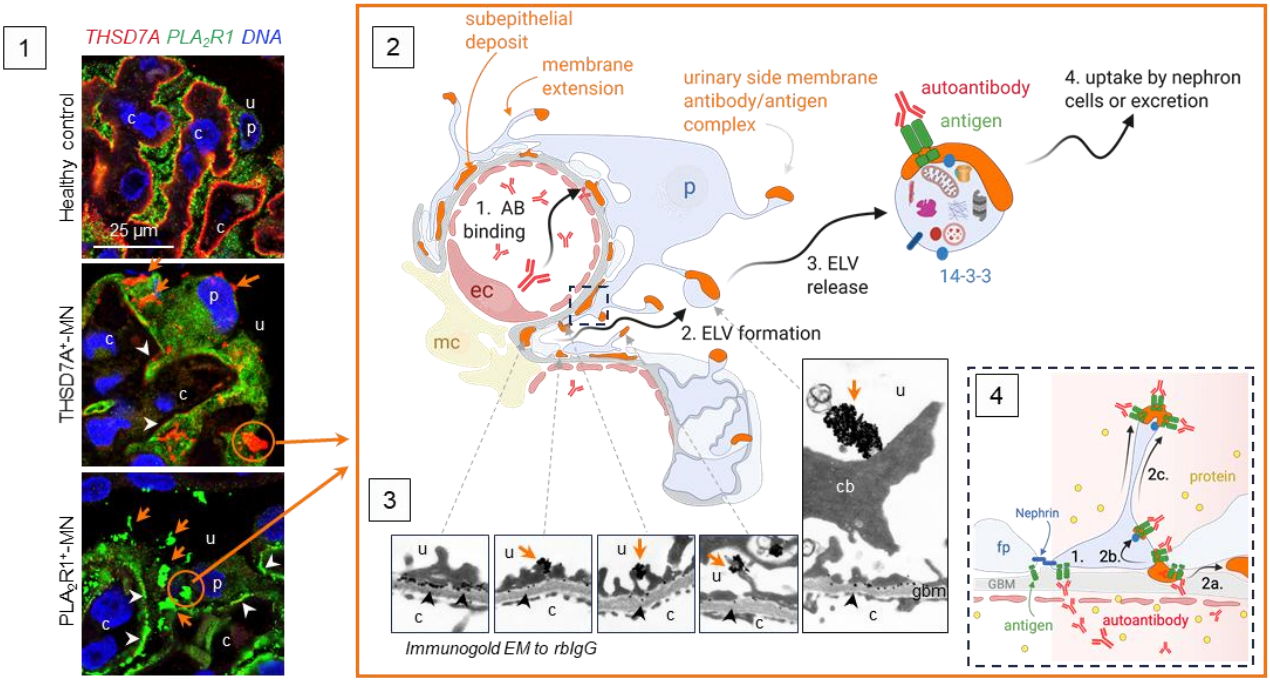

Figure 31: Scheme summarizing the concept of autoantibody fate using THSD7A as model antigen. Panel 1: Immunofluorescence staining of MN antigens THSD7A (red) and PLA_2R1 (green) in patient biopsies reveals urinary space aggregates (orange arrows), which arise from ELV formation. White arrowheads indicate subepithelial aggregates. **Panel 2:** The glomerular autoantibody burden is influenced by several factors: (1) the level of circulating autoantibodies that bind subepithelially to THSD7A, (2) the ability of podocytes to eliminate these autoantibodies via ELV formation, and (3) the subsequent ELV release into urine. These ELVs contain THSD7A bound to autoantibodies, 14-3-3 as an EV marker, disease-associated and foot process (FP) proteins, dysfunctional mitochondria, and degradative components. (4) ELVs can either be taken up by nephron cells or excreted to the urine. **Panels 3, 4:** ELV formation involves autoantibody-mediated THSD7A crosslinking in the subepithelial space. (1) THSD7A/autoantibody complexes form subepithelially, following either (2a) the classical concept, where black arrowheads in immunogold EM micrographs highlight rbIgG binding, or (2b) the newly proposed mechanism, where THSD7A/autoantibody complexes translocate toward the urinary side (orange arrows in immunogold EM images). (2c) These complexes extend as stalked vesicles. Abbreviations: ec = endothelial cell, mc = mesangial cell, p = podocyte, GBM = glomerular basement membrane, fp = foot process, c = capillary lumen, u = urinary space, cb = cell body.

5 Discussion

Membranous nephropathy (MN) remains a major cause of nephrotic syndrome and a leading contributor to end-stage renal disease[90, 91]. While significant advances have been made in identifying disease-associated antigens[99, 111-113], the precise mechanisms underlying the characteristic histopathological changes with the formation of pathognomonic antigen-autoantibody aggregates in MN[97, 98] and their role in disease progression remain incompletely understood. The study provides new insights into podocyte vesicular dynamics, highlighting the critical role of extracellular vesicle formation and membrane blebbing in response to immune-mediated stress. Podocyte injury plays a pivotal role in MN-disease progression, with disturbances in proteostasis and dysregulation of the ubiquitin-proteasome system (UPS) leading to protein accumulation and cellular stress, being key contributors[45, 46, 49]. Traditionally, these alterations have been assessed through invasive biopsy samples, which provide only limited insight into disease progression. Emerging evidence suggests that podocytes release extracellular vesicles, including large EVs (lEVs) and small EVs (sEVs), as a response to stress[158, 159]. This led us to explore urinary EVs as a non-invasive biomarker for evaluating podocyte proteostasis in various experimental models of podocyte injury.

EVs are heterogenous in size, content, and biogenesis. They are broadly categorized into small EVs (typically < 200 nm) and large EVs (> 200 nm), which arise through distinct cellular pathways: sEVs primarily originate from the endosomal system, whereas lEVs are typically formed by direct outward budding of the plasma membrane[217, 218]. These differences in biogenesis influence their molecular cargo, surface markers, and potentially their function in intercellular communication and disease processes[219, 220]. Therefore, discriminating between lEVs and sEVs may represent a crucial point for accurate content analysis and functional interpretation, especially in complex biofluids like urine, which contain mixed EV populations. This study investigated urinary EVs (uEVs) from mouse and human urine and found that UPS proteins were present in both lEVs and sEVs, but with no significant differences in abundance between healthy and disease conditions. While EVs have traditionally been classified by size, this approach does not necessarily reflect distinct biological functions, as many EV subtypes share overlapping biogenesis pathways and cargo compositions. The findings of this study support this limitation, indicating that urinary lEVs and sEVs cannot be reliably distinguished as functionally separate populations based on size alone. Despite overlapping cargo, their differing cellular origins or molecular surface differences may be a more informative and biologically meaningful strategy, particularly for understanding disease mechanisms and improving the specificity of EV-based biomarkers or therapeutic applications[160, 167]. To address this, the present study extended the analysis beyond size-based EV classification by identifying the dynamics and characterizing podocyte-derived urinary EVs (p-uEVs) in comparison to non-podocyte-derived EVs across different podocyte injury models, including

THSD7A-antibody-induced MN, Adriamycin nephropathy and diabetic nephropathy. One of the most intriguing aspects of our study was the differential release of podocyte-derived urinary EVs in response to different forms of injury. While metabolic (diabetic nephropathy) and toxic (Adriamycin nephropathy) podocyte injuries, did not significantly alter p-uEV release, THSD7A antibody-mediated injury, resulted in a marked increase in the secretion of both small and large EVs. These models differ in their pathogenic mechanisms: DN is characterized by hyperglycemia and chronic metabolic stress that progressively damage podocytes[30, 62, 221], whereas Adriamycin nephropathy involves direct podocyte cytotoxicity[131, 135]. In contrast, THSD7A-associated MN involves the deposition of subepithelial immune complexes formed as a consequence of a specific autoantibody targeting of podocyte antigens[106, 194]. This suggests that the selective increase in vesicle release observed in antibody-mediated membranous nephropathy (MN) is specifically triggered by the formation and accumulation of immune complexes within the glomerular filtration barrier, leading to its damage. This may reflect an active attempt by podocytes to release pathogenic immune deposits or damaged membrane components via EV shedding, potentially as part of a clearance mechanism to preserve the glomerular filter function, as previous studies described immunoglobulin and immune complex abundance within microparticles in other diseases[222, 223].

The study further compared glomerular ubiquitin proteasomal system protein dynamics in THSD7A$^+$-MN and adriamycin nephropathy and assessed whether urinary EV content reflects podocyte proteostasis. Studies using rat and mouse models of chronic podocyte injury have revealed that while injured podocytes upregulate the immunoproteasome, its enzymatic function becomes impaired[45]. This impairment leads to the accumulation of K48-linked polyubiquitinated proteins, which are typically destined for degradation but fail to be efficiently processed[45, 46]. In the context of Adriamycin treatment, disturbances in the UPS with a decreased proteasomal activity and accumulation of polyubiquitinated proteins are described for mouse cardiomyocytes[224, 225] and skeletal muscles[226]. In the presented study experiments, despite comparable proteinuria levels, THSD7A$^+$-MN mice exhibited more severe proteostasis alterations, including accumulation of oxidatively modified proteins, proteasome substrates, and immunoproteasome subunit Lmp7, which goes along with the findings of Beeken et al. in the anti-podocyte nephritis model of MN. Interestingly, in THSD7A$^+$-MN and Adriamycin mice, urinary EV content analyzed by immunoblotting to UCH-L1, K48-pUB and Lmp7 correlated with the glomerular protein levels assessed by immunofluorescence, but to a stronger extend in the MN mice. This finding further underscores the potentially disease-specific nature of the podocyte response in THSD7A-MN. To test the feasibility of assessing UPS protein abundance and enzymatic activity in nephrotic patients, we used p-uEVs isolated via GLEPP1 pulldown. As the GLEPP1 protein is only and primarily expressed at the apical membrane of podocytes[211], it is a suitable protein to target the podocyte-derived EVs in the

immunoprecipitation. Urine samples from patients diagnosed with THSD7A$^+$-MN, PLA$_2$R1$^+$-MN, FSGS, and DN on the day of kidney biopsy were selected to align with the previously studied murine models of podocyte injury, as human FSGS is comparable to the murine Adriamycin induced glomerular damage[133, 134]. Notably, K48-pUB within GLEPP1$^+$-EVs correlated with the podocyte K48-pUB mean fluorescence intensity in the corresponding patient biopsies. These findings suggest that urinary p-uEV content reflects divers podocyte injury patterns. However, while this experiment demonstrates the technical feasibility of assessing the UPS status in p-uEV of patients, future investigations in larger prospective and longitudinal patient cohorts are necessary to validate the observation, if this approach can reliably mirror the podocyte distinct pathophysiological mechanism. Besides evaluating UPS abundance, it remains crucial to determine whether UPS function itself is altered in injured podocyte and whether these changes can be measured and are mirrored in p-uEVs, reflecting the severity of podocyte injury and the prospective clinical outcome.

However, a challenge in the presented EV analyses and as a general concern in the EV field, technical and normalization factors may influence findings and warrant further investigation[170, 202]. As accessible biomaterial, EVs are inherently challenging due to their molecular and structural heterogeneity[227]. While EVs can be categorized based on size, density, biogenesis, or isolation methods, their overlapping characteristics, such as marker expression, composition, and function, complicate their precise classification[170]. A major obstacle in EV research is the lack of a universally standardized isolation protocol. The choice of isolation technique, including ultracentrifugation, size exclusion chromatography, ultrafiltration, density-gradient centrifugation, and immunoprecipitation, depends on the intended downstream analysis and specific research or clinical needs. This variability affects purity, yield, and composition of the EV populations and significantly impacts characterization, biomarker identification, and reproducibility, posing challenges for both fundamental research and clinical applications[170, 177, 202, 227].

The study further found a strong link between immune-mediated podocyte injury and oxidative stress, as shown by the abundance and elevated levels of 4-hydroxynonenal (4-HNE), a well-established marker of lipid peroxidation in podocytes[228]. The link between peroxidated lipids and glomerular diseases was already described in rats with passive Heymann nephritis (model for membranous nephropathy) and in human kidneys of different glomerular diseases. An increase of oxidative modified lipids in glomeruli, especially at cell membranes and the GBM were described[229, 230]. In the present study this link was also observed in the passive THSD7A antibody-mediated MN model. 4-HNE was significantly elevated in THSD7A$^+$-MN mice, particularly at the glomerular filtration barrier and podocyte plasma membrane. This suggests that regions of autoantibody-antigen interaction are highly susceptible to oxidative damage, potentially driving vesicle formation as a means of expelling peroxidized lipids and damaged

proteins. Notably, 4-HNE levels peaked early in disease progression indicating a transient but critical oxidative burst that may shape the initial phase of podocyte injury. Another key observation was the early and sustained upregulation of Annexin A1 in podocytes, a protein involved in Ca^{2+}-dependent membrane stabilization and repair[231, 232]. Annexin A1 is also described as an EV marker, primarily in EVs formed at and released from plasma membrane[233]. This study showed that the Annexin A1 levels were markedly elevated from day 1 of disease induction, suggesting an immediate response to immune complex deposition. Immunofluorescence analysis further confirmed its localization to podocyte plasma membranes and filamentous extensions protruding into the urinary space, structures that colocalized with membrane-tagged GFP in *mT/mG* $THSD7A^{+}$-MN mice. These findings strongly imply that Annexin A1 plays a role in stabilizing membrane regions undergoing active remodeling and vesiculation in experimental membranous nephropathy. The formation of membrane extensions appears to be an adaptive cellular strategy, potentially facilitating the controlled release of damaged membrane components, preserving podocyte function and integrity in the face of ongoing immune-mediated stress.

Building on these findings, this study characterized in more depth MN-patient biopsies and their corresponding p-uEVs and identified them as a novel EV subtype termed exopher-like vesicles (ELVs), as they are morphologically and functional remiscient of exophers. Exophers represent an EV subtype first described in neurons of *C.elegans*[185]. In *C.elegans*, large exophers were formed by neurons when chaperon expression, autophagy or the proteasome were inhibited. Exophers carried protein aggregates and organelles. Notably, neurons under proteotoxic stress that exhibited an increased exopher release had a better cellular function in comparison to neurons without exopher release[185]. Hence, the formation of exophers in *C. elegans* neurons was proposed as a neuroprotective mechanism, and to function as a constitute component of proteostasis control, which might contribute to pathogenesis in neurodegenerative disease when exopher formation is diminished[185]. Exopher formation has since the also been described in *C. elegans* body wall muscle cells where the exopher release and uptake from neighboring cells stimulates reproductive capacity[190] and in murine cardiomyocytes[189], where they function as well as a stress-response mechanism to expel toxic components when cardiomyocyte proteostasis and organelle function are compromised[185, 187, 188].

The presented data in this study indicate that MN-associated ELVs fulfill important exopher criteria, including 1) the extrusion from apical membranes, 2) the expression of general EV markers, like Annexin A1, 14-3-3 and Flotilin, 3) the content of cellular dysfunctional organelles like mitochondria and protein aggregates, 4) the reuptake by neighboring cells along the nephron and 5) the enhanced extrusion from podocytes in the setting of proteotoxic stress. In particular, the observed enhanced ELV-formation and release into the urine under proteasomal

inhibition in mice resembles the described proteotoxic stress dynamics of exopher formation in *C.elegans* neurons and murine cardiomyocytes, and underscores that ELV formation represents an important functional mechanism to maintain cellular proteostasis. These aspects confirm ELVs as an exopher-related EV type. Moreover, MN-associated ELVs harbour the antigen and pathognomonic autoantibody (huIgG4$^+$), as a defining feature of MN. The study further identified the ubiquitously expressed 14-3-3 chaperone-like protein as an ELV-discerning protein, highly abundant in patient and experimental EVs. 14-3-3 is involved in *C. elegans* exopher-formation[191]. Further, 14-3-3 is a plasma membrane-localizing protein[234-236] that participates in aggresome formation and plasma membrane budding in response to proteotoxic stress[191]. Given these functions, 14-3-3 may contribute to the release of podocyte-derived EVs under stress conditions. The role of 14-3-3 in podocyte ELV-genesis may be further linked to its known interactions with the foot process protein synaptopodin. Synaptopodin acts as an actin-regulating protein essential for podocyte stability in its interaction with 14-3-3. The interaction with 14-3-3 protects synaptopodin from cathepsin L-mediated degradation. Synaptopodin interaction with 14-3-3 is altered upon dephosphorylation by the phosphatase calcineurin. It is thought that activation of calcineurin in podocytes leads to synaptopodin degradation, contributing to proteinuria[237]. The immunosuppressant cyclosporin A, used in the treatment of MN patient[238], inhibits calcineurin-mediated dephosphorylation of synaptopodin and is thus thought to mediate its anti-proteinuric properties. Overall, the discovered MN-associated ELVs in this study represent a unique form of huIgG4$^+$/14-3-3$^+$ EVs. Immunofluorescence staining and immunoblot analyses confirmed vesicle marker abundance, but showing a different distribution to nephrotic non-MN patient huIgG4$^+$-EVs. The podocyte origin was confirmed with the abundance of podocyte markers, like THSD7A, PLA_2R1, Nephrin, Podocin, α-Actinin-4 and importantly, also proteins regulated in MN disease like complement, mitochondrial, lysosomal and ubiquitin proteasomal proteins were highly abundant in the ELVs of MN patients, making them distinguishable from other nephrotic non-MN urinary huIgG4$^+$ EVs, as they show differences in the molecular protein composition.

The presence of podocyte-specific and proteotoxic stress markers within the discovered ELVs in addition to the finding that both experimental models of MN as well as MN patient samples display accumulated proteasome substrates, indicating alterations in proteasomal degradation pathways[45, 50, 151], supports the idea that ELV-genesis may serve as a protective mechanism to mitigate immune-mediated damage from the podocytes. This underscores their relevance to MN pathophysiology. This hypothesis is supported by the findings of Sachs et al., where in mice with proteasome inhibition, proteasome substrates accumulated predominantly in podocytes, whereas other glomerular cells remained largely unaffected, highlighting their limited ability to maintain proteostasis under such stress. While podocytes could compensate

for autophagy or lysosomal dysfunction by upregulating proteasome activity, the reverse compensation failed. As a result, proteostasis was specifically disturbed in podocytes. Notably, it was seen that IgG accumulated at the slit diaphragm, resembling early immune complex deposition in membranous nephropathy. This demonstrated that proteasomal activity in podocytes is essential for preventing immunoglobulin accumulation and maintaining a proper endocytic membrane protein recycling activity[50]. Given its mechanistic significance, targeting ELV genesis through proteasome modulation presents a possible therapeutic avenue. Based on the findings, ELV genesis can be considered as a responsive mechanism to compensate for a degradative impairment promoting the clearance of disease-associated protein accumulations from podocytes. In this context, ELV production serves as a protective mechanism during proteostasis disruption by extruding immune complexes through the podocyte plasma membrane and releasing them into the urinary space. This function aligns with the observation that urinary ELV release inversely correlated with glomerular antigen/autoantibody deposition in experimental THSD7A$^+$-MN. Podocytes may actively contribute to the reduction of the glomerular burden of immune deposits and clearance from protein accumulations, thereby preserving podocyte function. However, when ELV-genesis becomes excessive or dysregulated, such as under conditions of proteasomal impairment, it may contribute to podocyte exhaustion and disease progression, ultimately exacerbating proteinuria. This was observed in the disease course in treated THSD7A$^+$-MN mice. One possible explanation for this podocyte exhaustion is that highly abundant ELV release could lead to a substantial loss of plasma membrane, thereby reducing the surface area of the podocyte foot processes (FP). Such reduction is reflected in FP effacement, a diagnostic hallmark of MN[50]. To evaluate and quantify this morphological damage to the podocyte membrane, the filtration slit density (FSD) was measured using the podocyte exact morphology measurement procedure (PEMP) method[210] in mouse models of podocyte injury. The slit diaphragm (SD) protein nephrin were stained and analyzed by high-resolution microscopy. FSD was calculated as the ratio of SD length (based on nephrin signal) to capillary area within a glomerulus. In THSD7A$^+$-MN mice, FSD was reduced (Fig. 9), indicating a loss of foot process surface area consistent with effacement. This raises the possibility that differences in the ability of podocytes to repair their plasma membranes could influence the extent of injury resulting form excessive vesicle shedding. Supporting this hypothesis, it is known that in mammalian cells, the fusion of lysosome membranes with the plasma membrane (lysosomal exocytosis) represents one major repair mechanism[239, 240]. Lysosomes are abundant and enlarged in injured podocytes of rodents[45, 241] and of nephrotic patients, especially Limp2$^+$ lysosomes[242, 243]. Limp2$^+$ lysosomes could represent a lysosomal population that is prone to fuse to and thus replenish the podocyte plasma membrane. In this study, in day 7 THSD7A$^+$-MN mice immunogold EMs to rbIgG membrane whorls adjacent to podocyte foot and major

processes were seen within the urinary space (Fig. S1), which in other cellular systems indicate lysosomal exocytosis[239]. The FP vesicles and membrane whorls were free of gold, showing that they originated in a parallel but distinct process from gold-labeled ELVs. Further investigations are required, to prove if lysosomal exocytosis is functionally present and compensates for the podocyte membrane loss arising from ELV release. Potentially the ELV release is a protective process but contributes to podocyte injury if excessive, emphasizing the need for a balance between EV release and membrane repair for podocyte homeostasis.

From a clinical perspective, the analysis of urinary ELV holds a significant diagnostic and prognostic potential. Since ELVs detach from podocytes to the urine by translocating antigen-antibody complexes from the FP base to the urinary side, they are easily and non-invasively accessible within the urine. The clinical potential of ELVs comprises disease monitoring, as the quantitative ELV abundance and autoantibody presence in urinary ELVs offers a fine-tuned assessment of MN activity as presented with the longitudinal studies of two MN patients. The described comparative monitoring of the relapsing THSD7A$^+$-MN patient and the remitting PLA$_2$R1$^+$-MN patient with distinct disease trajectories and treatment responses revealed key insights: 1) Alterations in ELV genesis, such as reduced formation at the podocyte FP membrane or reduced urinary release, were associated with a non-remitting clinical course in the THSD7A$^+$-MN patient. In contrast, the PLA$_2$R1$^+$-MN patient with sustained ELV release showed better treatment response, suggesting that enhancing this process could have therapeutic potential. 2) ELV enrichment is a highly sensitive and non-invasive approach for detecting and tracking MN autoantibodies. This technique could be particularly valuable in cases where serum autoantibody levels do not correlate with disease activity. 3) Enriched ELVs represent a valuable biological resource for molecular analyses of podocyte pathology. By isolating and characterizing podocyte-derived ELVs, it is possible to gain deeper insights into MN-specific molecular signatures and identify novel therapeutic targets.

To further assess the functionality and sensitivity of the proposed non-invasive approach for detecting and tracking MN autoantibodies, the presence of ELV-bound autoantibody was analyzed in 18 MN patients and compared to the current gold standard diagnostics (nephropathology of a biopsy combined with serum autoantibody titer abundance). With this non-invasive approach, autoantibodies in 12 THSD7A$^+$/PLA$_2$R1$^+$-MN patients could be confirmed. Strikingly, autoantibodies in ELVs to PLA$_2$R1 could be detected in three out of five patients that were originally diagnosed with THSD7A$^-$/PLA$_2$R1$^-$ secondary MN, as biopsy and serum titer diagnostics proofed negative. This could be due to the described phenomenon of passive entrapment of circulating immune complexes within the GBM[244], showing the advantage of ELV autoantibody in the diagnostic in patients with low or undetectable serum autoantibody titers and/or unclear histopathological diagnostic biopsies. In addition, ELV enrichment could enable the discovery of novel MN-specific autoantibodies or the diagnosis of

other glomerular pathologies such as minimal change disease (MCD). The latter is underpinned by the discovery of MCD-associated autoantibodies against the slit diaphragm protein nephrin[245].

Taken together, in contrast to conventional autoantibody detection within the patients' serum and kidney biopsy, urinary ELV-bound autoantibody qualification provides a direct, non-invasive window into ongoing disease, not only for initial diagnosis. It also enables disease monitoring under therapy and might therefore be a tool for the prediction of therapeutical success and/or disease outcome. The ability of podocytes to overcome disease-causing autoantibodies by releasing ELVs in the urine can be analyzed directly with the presented method. Further, the molecular imprint of the disease can be investigated using this new, non-invasive diagnostic approach. These findings underscore that podocytes are actively engaged in a sophisticated response to immune-mediated stress involving selective membrane remodeling, oxidative stress adaptation, resulting in the ELV-mediated immuncomplex clearance. However, ELV genesis may also contribute to disease progression by facilitating glomerular antigen spreading. A hint for this could be the presence of secondary autoantibodies in MN patient to the dysfunctional UCH-L1 protein[151]. In MN, oxidative stress induces the deubiquitinase UCH-L1 in podocytes, where a non-functional form disrupts proteasome activity, leading to toxic protein accumulation in podocytes. MN patients with poor outcome exhibit autoantibodies with preferential reactivity to non-functional UCH-L1[151]. In line with the findings of this study, it can be speculated that the increased UCH-L1 protein is packed into ELVs, released into the urine and taken up by for example tubular cells along the nephron. This glomerular release of functional or unfunctional proteins may trigger the production of "secondary" autoantibodies in MN patients. Further, excessive circulating primary (THSD7A, PLA_2R1) and secondary (i.e. to UCH-L1) autoantibodies may overwhelm the ELV-based clearance system, contributing to disease progression through excessive plasma membrane loss and therapy resistance.

The balance between autoantibody titer, ELV formation and release likely determines podocyte fate and treatment response. Whether these processes can be therapeutically modulated to improve patient outcomes remains an open question, but the potential for targeting ELV genesis and proteostasis pathways in MN is an exciting avenue for future research. Future research should focus on validating these findings through: (1) the correlation of glomerular antigen and IgG deposition patterns with clinical outcomes in larger MN patient cohorts, (2) prospectively measuring urinary ELV abundance alongside autoantibody serum titers to track disease progression, and (3) by further characterizing ELV protein content and autoantibody binding to identify novel biomarkers and autoantigens. These efforts will pave the way for personalized diagnostics and targeted therapies in MN and related glomerular diseases.

6 References

1. Segerer, K.W., C., *Niere und Ableitende Harnwege*, ed. T. Luescher. 2014: Springer Berlin.
2. Silbernagl, S. and F. Lang, *Color atlas of pathophysiology*. 2nd ed. Thieme flexibook. 2010, Stuttgart ; New York: Thieme, p 433.
3. Munger, K., *The Renal Circulations and Glomerular Ultrafiltration*, in *Brenner and Rector's The Kidney*. 2011, Elsevier. p. 95-137.
4. Stein, J.H. and S.Z. Fadem, *The renal circulation.* JAMA, 1978. **239**(13): p. 1308-12.
5. O'Brien, F. *Overview of Kidney Filtering Disorders*. 2023 2023/08 [cited 2023; Available from: https://www.msdmanuals.com/home/kidney-and-urinary-tract-disorders/kidney-filtering-disorders/overview-of-kidney-filtering-disorders.
6. Scott, R.P. and S.E. Quaggin, *Review series: The cell biology of renal filtration.* J Cell Biol, 2015. **209**(2): p. 199-210.
7. Barrett, K.E., et al., *Renal Function & Micturition*, in *Ganong's Review of Medical Physiology, 25e*. 2018, McGraw-Hill Education: New York, NY.
8. Lacombe, C., et al., *Peritubular cells are the site of erythropoietin synthesis in the murine hypoxic kidney.* J Clin Invest, 1988. **81**(2): p. 620-3.
9. Fisher, J.W., *Erythropoietin: physiology and pharmacology update.* Exp Biol Med (Maywood), 2003. **228**(1): p. 1-14.
10. Persson, P.B., *Renin: origin, secretion and synthesis.* J Physiol, 2003. **552**(Pt 3): p. 667-71.
11. Williams, S., K. Malatesta, and K. Norris, *Vitamin D and chronic kidney disease.* Ethn Dis, 2009. **19**(4 Suppl 5): p. S5-8-11.
12. D'Agati, V.D., et al., *Pathologic classification of focal segmental glomerulosclerosis: a working proposal.* Am J Kidney Dis, 2004. **43**(2): p. 368-82.
13. Taal, M.W., B.M. Brenner, and F.C. Rector, *Brenner & Rector's the kidney*. 9th ed. 2012, Philadelphia, PA: Elsevier/Saunders.
14. Puelles, V.G., et al., *Glomerular number and size variability and risk for kidney disease.* Curr Opin Nephrol Hypertens, 2011. **20**(1): p. 7-15.
15. Hjalmarsson, C., B.R. Johansson, and B. Haraldsson, *Electron microscopic evaluation of the endothelial surface layer of glomerular capillaries.* Microvasc Res, 2004. **67**(1): p. 9-17.
16. Chang, R.L., et al., *Permselectivity of the glomerular capillary wall: III. Restricted transport of polyanions.* Kidney Int, 1975. **8**(4): p. 212-8.
17. Peti-Peterdi, J. and A. Sipos, *A high-powered view of the filtration barrier.* J Am Soc Nephrol, 2010. **21**(11): p. 1835-41.
18. Rostgaard, J. and K. Qvortrup, *Sieve plugs in fenestrae of glomerular capillaries--site of the filtration barrier?* Cells Tissues Organs, 2002. **170**(2-3): p. 132-8.
19. Byron, A., et al., *Glomerular cell cross-talk influences composition and assembly of extracellular matrix.* J Am Soc Nephrol, 2014. **25**(5): p. 953-66.
20. Abrahamson, D.R., *Role of the podocyte (and glomerular endothelium) in building the GBM.* Semin Nephrol, 2012. **32**(4): p. 342-9.
21. Abrahamson, D.R., *Structure and development of the glomerular capillary wall and basement membrane.* Am J Physiol, 1987. **253**(5 Pt 2): p. F783-94.
22. Pavenstadt, H., W. Kriz, and M. Kretzler, *Cell biology of the glomerular podocyte.* Physiol Rev, 2003. **83**(1): p. 253-307.
23. Greka, A. and P. Mundel, *Cell biology and pathology of podocytes.* Annu Rev Physiol, 2012. **74**: p. 299-323.
24. Simons, M., B. Hartleben, and T.B. Huber, *Podocyte polarity signalling.* Curr Opin Nephrol Hypertens, 2009. **18**(4): p. 324-30.

25. Kerjaschki, D., *Caught flat-footed: podocyte damage and the molecular bases of focal glomerulosclerosis.* J Clin Invest, 2001. **108**(11): p. 1583-7.
26. Suleiman, H.Y., et al., *Injury-induced actin cytoskeleton reorganization in podocytes revealed by super-resolution microscopy.* JCI Insight, 2017. **2**(16).
27. Andrews, P.M., *Investigations of cytoplasmic contractile and cytoskeletal elements in the kidney glomerulus.* Kidney Int, 1981. **20**(5): p. 549-62.
28. Cortes, P., et al., *F-actin fiber distribution in glomerular cells: structural and functional implications.* Kidney Int, 2000. **58**(6): p. 2452-61.
29. Vasmant, D., M. Maurice, and G. Feldmann, *Cytoskeleton ultrastructure of podocytes and glomerular endothelial cells in man and in the rat.* Anat Rec, 1984. **210**(1): p. 17-24.
30. Shankland, S.J., *The podocyte's response to injury: role in proteinuria and glomerulosclerosis.* Kidney Int, 2006. **69**(12): p. 2131-47.
31. Drenckhahn, D. and R.P. Franke, *Ultrastructural organization of contractile and cytoskeletal proteins in glomerular podocytes of chicken, rat, and man.* Lab Invest, 1988. **59**(5): p. 673-82.
32. Lennon, R., M.J. Randles, and M.J. Humphries, *The importance of podocyte adhesion for a healthy glomerulus.* Front Endocrinol (Lausanne), 2014. **5**: p. 160.
33. Raats, C.J., et al., *Expression of agrin, dystroglycan, and utrophin in normal renal tissue and in experimental glomerulopathies.* Am J Pathol, 2000. **156**(5): p. 1749-65.
34. Regele, H.M., et al., *Glomerular expression of dystroglycans is reduced in minimal change nephrosis but not in focal segmental glomerulosclerosis.* J Am Soc Nephrol, 2000. **11**(3): p. 403-412.
35. Kocylowski, M.K., et al., *A slit-diaphragm-associated protein network for dynamic control of renal filtration.* Nat Commun, 2022. **13**(1): p. 6446.
36. Asanuma, K., et al., *Synaptopodin orchestrates actin organization and cell motility via regulation of RhoA signalling.* Nat Cell Biol, 2006. **8**(5): p. 485-91.
37. Nielsen, J.S. and K.M. McNagny, *The role of podocalyxin in health and disease.* J Am Soc Nephrol, 2009. **20**(8): p. 1669-76.
38. Wieder, N. and A. Greka, *Calcium, TRPC channels, and regulation of the actin cytoskeleton in podocytes: towards a future of targeted therapies.* Pediatr Nephrol, 2016. **31**(7): p. 1047-54.
39. Miner, J.H., *Renal basement membrane components.* Kidney Int, 1999. **56**(6): p. 2016-24.
40. Ito, K., Y.C. Ger, and S. Kawamura, *Actin filament alterations in glomerular epithelial cells of adriamycin-induced nephrotic rats.* Acta Pathol Jpn, 1986. **36**(2): p. 253-60.
41. Whiteside, C.I., et al., *Podocytic cytoskeletal disaggregation and basement-membrane detachment in puromycin aminonucleoside nephrosis.* Am J Pathol, 1993. **142**(5): p. 1641-53.
42. Pullen, N. and A. Fornoni, *Drug discovery in focal and segmental glomerulosclerosis.* Kidney Int, 2016. **89**(6): p. 1211-20.
43. Grahammer, F., N. Wanner, and T.B. Huber, *mTOR controls kidney epithelia in health and disease.* Nephrol Dial Transplant, 2014. **29 Suppl 1**: p. i9-i18.
44. Imasawa, T. and R. Rossignol, *Podocyte energy metabolism and glomerular diseases.* Int J Biochem Cell Biol, 2013. **45**(9): p. 2109-18.
45. Beeken, M., et al., *Alterations in the ubiquitin proteasome system in persistent but not reversible proteinuric diseases.* J Am Soc Nephrol, 2014. **25**(11): p. 2511-25.
46. Meyer-Schwesinger, C., *The ubiquitin-proteasome system in kidney physiology and disease.* Nat Rev Nephrol, 2019. **15**(7): p. 393-411.

47. Heintz, L. and C. Meyer-Schwesinger, *The Intertwining of Autophagy and the Ubiquitin Proteasome System in Podocyte (Patho)Physiology.* Cell Physiol Biochem, 2021. **55**(S4): p. 68-95.
48. Xu, H. and D. Ren, *Lysosomal physiology.* Annu Rev Physiol, 2015. **77**: p. 57-80.
49. Meyer-Schwesinger, C., et al., *Ubiquitin C-terminal hydrolase-l1 activity induces polyubiquitin accumulation in podocytes and increases proteinuria in rat membranous nephropathy.* Am J Pathol, 2011. **178**(5): p. 2044-57.
50. Sachs, W., et al., *The proteasome modulates endocytosis specifically in glomerular cells to promote kidney filtration.* Nat Commun, 2024. **15**(1): p. 1897.
51. MacGurn, J.A., P.C. Hsu, and S.D. Emr, *Ubiquitin and membrane protein turnover: from cradle to grave.* Annu Rev Biochem, 2012. **81**: p. 231-59.
52. Rudolphi, C.F., et al., *Urinary extracellular vesicles and tubular transport.* Nephrol Dial Transplant, 2023. **38**(7): p. 1583-1590.
53. Levick, J.R. and L.H. Smaje, *An analysis of the permeability of a fenestra.* Microvasc Res, 1987. **33**(2): p. 233-56.
54. Dalal, R., Z.S. Bruss, and J.S. Sehdev, *Physiology, Renal Blood Flow and Filtration*, in *StatPearls*. 2025: Treasure Island (FL).
55. Benedum, M.M.J., *Einführung in die Medizinische Terminologie.* 2. Auflage ed. 1981: Springer Verlag.
56. Initiative, M. Retrieved December 29, 2024; Available from: https://monarchinitiative.org/HP:0100820.
57. Walz, G., *[Pathogenetic aspectics of nephrotic syndrome].* Internist (Berl), 2003. **44**(9): p. 1075-82.
58. Verma, P.R. and P. Patil, *Nephrotic Syndrome: A Review.* Cureus, 2024. **16**(2): p. e53923.
59. Maas, R.J., J.K. Deegens, and J.F. Wetzels, *Permeability factors in idiopathic nephrotic syndrome: historical perspectives and lessons for the future.* Nephrol Dial Transplant, 2014. **29**(12): p. 2207-16.
60. Achenbach, J., et al., *Parietal epithelia cells in the urine as a marker of disease activity in glomerular diseases.* Nephrol Dial Transplant, 2008. **23**(10): p. 3138-45.
61. Flyvbjerg, A., *Putative pathophysiological role of growth factors and cytokines in experimental diabetic kidney disease.* Diabetologia, 2000. **43**(10): p. 1205-23.
62. Cooper, M.E., *Interaction of metabolic and haemodynamic factors in mediating experimental diabetic nephropathy.* Diabetologia, 2001. **44**(11): p. 1957-72.
63. Viberti, G.C., et al., *Microalbuminuria as a predictor of clinical nephropathy in insulin-dependent diabetes mellitus.* Lancet, 1982. **1**(8287): p. 1430-2.
64. Mogensen, C.E. and C.K. Christensen, *Predicting diabetic nephropathy in insulin-dependent patients.* N Engl J Med, 1984. **311**(2): p. 89-93.
65. Cooper, M.E., R.E. Gilbert, and M. Epstein, *Pathophysiology of diabetic nephropathy.* Metabolism, 1998. **47**(12 Suppl 1): p. 3-6.
66. Zatz, R., et al., *Prevention of diabetic glomerulopathy by pharmacological amelioration of glomerular capillary hypertension.* J Clin Invest, 1986. **77**(6): p. 1925-30.
67. Hargrove, G.M., et al., *Diabetes mellitus increases endothelin-1 gene transcription in rat kidney.* Kidney Int, 2000. **58**(4): p. 1534-45.
68. Adler, A.I., et al., *Association of systolic blood pressure with macrovascular and microvascular complications of type 2 diabetes (UKPDS 36): prospective observational study.* BMJ, 2000. **321**(7258): p. 412-9.
69. Stratton, I.M., et al., *Association of glycaemia with macrovascular and microvascular complications of type 2 diabetes (UKPDS 35): prospective observational study.* BMJ, 2000. **321**(7258): p. 405-12.

70. Conley, M.E., M.D. Cooper, and A.F. Michael, *Selective deposition of immunoglobulin A1 in immunoglobulin A nephropathy, anaphylactoid purpura nephritis, and systemic lupus erythematosus.* J Clin Invest, 1980. **66**(6): p. 1432-6.
71. Julian, B.A. and J. Novak, *IgA nephropathy: an update.* Curr Opin Nephrol Hypertens, 2004. **13**(2): p. 171-9.
72. Novak, J., et al., *Progress in molecular and genetic studies of IgA nephropathy.* J Clin Immunol, 2001. **21**(5): p. 310-27.
73. Czerkinsky, C., et al., *Circulating immune complexes and immunoglobulin A rheumatoid factor in patients with mesangial immunoglobulin A nephropathies.* J Clin Invest, 1986. **77**(6): p. 1931-8.
74. Schena, F.P., et al., *Increased serum levels of IgA1-IgG immune complexes and anti-F(ab')2 antibodies in patients with primary IgA nephropathy.* Clin Exp Immunol, 1989. **77**(1): p. 15-20.
75. Novak, J., et al., *Interactions of human mesangial cells with IgA and IgA-containing immune complexes.* Kidney Int, 2002. **62**(2): p. 465-75.
76. Tomana, M., et al., *Circulating immune complexes in IgA nephropathy consist of IgA1 with galactose-deficient hinge region and antiglycan antibodies.* J Clin Invest, 1999. **104**(1): p. 73-81.
77. Tomana, M., et al., *Galactose-deficient IgA1 in sera of IgA nephropathy patients is present in complexes with IgG.* Kidney Int, 1997. **52**(2): p. 509-16.
78. Allen, A.C., et al., *Mesangial IgA1 in IgA nephropathy exhibits aberrant O-glycosylation: observations in three patients.* Kidney Int, 2001. **60**(3): p. 969-73.
79. Hiki, Y., et al., *Mass spectrometry proves under-O-glycosylation of glomerular IgA1 in IgA nephropathy.* Kidney Int, 2001. **59**(3): p. 1077-85.
80. Suzuki, H., et al., *The pathophysiology of IgA nephropathy.* J Am Soc Nephrol, 2011. **22**(10): p. 1795-803.
81. Suzuki, H., et al., *IgA nephropathy: characterization of IgG antibodies specific for galactose-deficient IgA1.* Contrib Nephrol, 2007. **157**: p. 129-33.
82. Pitcher, D., et al., *Long-Term Outcomes in IgA Nephropathy.* Clin J Am Soc Nephrol, 2023. **18**(6): p. 727-738.
83. Berthoux, F., et al., *Predicting the risk for dialysis or death in IgA nephropathy.* J Am Soc Nephrol, 2011. **22**(4): p. 752-61.
84. Okonogi, H., et al., *A grading system that predicts the risk of dialysis induction in IgA nephropathy patients based on the combination of the clinical and histological severity.* Clin Exp Nephrol, 2019. **23**(1): p. 16-25.
85. Roxe, D.M., *Toxic nephropathy from diagnostic and therapeutic agents. Review and commentary.* Am J Med, 1980. **69**(5): p. 759-66.
86. Perazella, M.A. and M.H. Rosner, *Drug-Induced Acute Kidney Injury.* Clin J Am Soc Nephrol, 2022. **17**(8): p. 1220-1233.
87. Krishnan, N., D.G. Moledina, and M.A. Perazella, *Toxic Nephropathies of the Tubulointerstitium: Core Curriculum 2024.* Am J Kidney Dis, 2024. **83**(5): p. 659-676.
88. Joyce, E., et al., *Tubulointerstitial nephritis: diagnosis, treatment, and monitoring.* Pediatr Nephrol, 2017. **32**(4): p. 577-587.
89. Fogo, A.B., et al., *AJKD Atlas of Renal Pathology: Toxic Acute Tubular Injury.* Am J Kidney Dis, 2016. **67**(6): p. e31-2.
90. Ronco, P., E. Plaisier, and H. Debiec, *Advances in Membranous Nephropathy.* J Clin Med, 2021. **10**(4).
91. McGrogan, A., C.F. Franssen, and C.S. de Vries, *The incidence of primary glomerulonephritis worldwide: a systematic review of the literature.* Nephrol Dial Transplant, 2011. **26**(2): p. 414-30.

92. Hogan, S.L., et al., *A review of therapeutic studies of idiopathic membranous glomerulopathy.* Am J Kidney Dis, 1995. **25**(6): p. 862-75.
93. Ponticelli, C., *Membranous nephropathy.* J Nephrol, 2007. **20**(3): p. 268-87.
94. Wasserstein, A.G., *Membranous glomerulonephritis.* J Am Soc Nephrol, 1997. **8**(4): p. 664-74.
95. Borza, D.B., et al., *Mouse models of membranous nephropathy: the road less travelled by.* Am J Clin Exp Immunol, 2013. **2**(2): p. 135-45.
96. Hoxha, E., et al., *An Indirect Immunofluorescence Method Facilitates Detection of Thrombospondin Type 1 Domain-Containing 7A-Specific Antibodies in Membranous Nephropathy.* J Am Soc Nephrol, 2017. **28**(2): p. 520-531.
97. Ronco, P. and H. Debiec, *Pathophysiological advances in membranous nephropathy: time for a shift in patient's care.* Lancet, 2015. **385**(9981): p. 1983-92.
98. Fogo, A.B., et al., *AJKD Atlas of Renal Pathology: Membranous Nephropathy.* Am J Kidney Dis, 2015. **66**(3): p. e15-7.
99. Sethi, S. and F.C. Fervenza, *Membranous nephropathy-diagnosis and identification of target antigens.* Nephrol Dial Transplant, 2024. **39**(4): p. 600-606.
100. Beck, L.H., Jr. and D.J. Salant, *Membranous nephropathy: recent travels and new roads ahead.* Kidney Int, 2010. **77**(9): p. 765-70.
101. Schiller, B., et al., *Inhibition of complement regulation is key to the pathogenesis of active Heymann nephritis.* J Exp Med, 1998. **188**(7): p. 1353-8.
102. Kerjaschki, D., et al., *Transcellular transport and membrane insertion of the C5b-9 membrane attack complex of complement by glomerular epithelial cells in experimental membranous nephropathy.* J Immunol, 1989. **143**(2): p. 546-52.
103. Seifert, L., et al., *The classical pathway triggers pathogenic complement activation in membranous nephropathy.* Nat Commun, 2023. **14**(1): p. 473.
104. Herwig, J., et al., *Thrombospondin Type 1 Domain-Containing 7A Localizes to the Slit Diaphragm and Stabilizes Membrane Dynamics of Fully Differentiated Podocytes.* J Am Soc Nephrol, 2019. **30**(5): p. 824-839.
105. Beck, L.H., Jr., et al., *M-type phospholipase A2 receptor as target antigen in idiopathic membranous nephropathy.* N Engl J Med, 2009. **361**(1): p. 11-21.
106. Tomas, N.M., et al., *Thrombospondin type-1 domain-containing 7A in idiopathic membranous nephropathy.* N Engl J Med, 2014. **371**(24): p. 2277-2287.
107. Beck, L.H., Jr., *PLA2R and THSD7A: Disparate Paths to the Same Disease?* J Am Soc Nephrol, 2017. **28**(9): p. 2579-2589.
108. Hofstra, J.M., et al., *Anti-phospholipase A(2) receptor antibodies correlate with clinical status in idiopathic membranous nephropathy.* Clin J Am Soc Nephrol, 2011. **6**(6): p. 1286-91.
109. Hoxha, E., et al., *An immunofluorescence test for phospholipase-A(2)-receptor antibodies and its clinical usefulness in patients with membranous glomerulonephritis.* Nephrol Dial Transplant, 2011. **26**(8): p. 2526-32.
110. Hoxha, E., et al., *Enhanced expression of the M-type phospholipase A2 receptor in glomeruli correlates with serum receptor antibodies in primary membranous nephropathy.* Kidney Int, 2012. **82**(7): p. 797-804.
111. Sethi, S., et al., *Neural epidermal growth factor-like 1 protein (NELL-1) associated membranous nephropathy.* Kidney Int, 2020. **97**(1): p. 163-174.
112. Sethi, S., *New 'Antigens' in Membranous Nephropathy.* J Am Soc Nephrol, 2021. **32**(2): p. 268-278.
113. Sethi, S., et al., *Exostosin 1/Exostosin 2-Associated Membranous Nephropathy.* J Am Soc Nephrol, 2019. **30**(6): p. 1123-1136.
114. Couser, W.G., *Primary Membranous Nephropathy.* Clin J Am Soc Nephrol, 2017. **12**(6): p. 983-997.

115. Cattran, D.C. and P.E. Brenchley, *Membranous nephropathy: integrating basic science into improved clinical management.* Kidney Int, 2017. **91**(3): p. 566-574.
116. Braden, G.L., et al., *Changing incidence of glomerular diseases in adults.* Am J Kidney Dis, 2000. **35**(5): p. 878-83.
117. Feehally, J., et al., *Comprehensive clinical nephrology*. 4th ed. Expert consult. 2010, Philadelphia, Pa: Saunders/Elsevier.
118. Fogo, A.B., *Causes and pathogenesis of focal segmental glomerulosclerosis.* Nat Rev Nephrol, 2015. **11**(2): p. 76-87.
119. Schwartz, M.M. and S.M. Korbet, *Primary focal segmental glomerulosclerosis: pathology, histological variants, and pathogenesis.* Am J Kidney Dis, 1993. **22**(6): p. 874-83.
120. Rennke, H.G. and P.S. Klein, *Pathogenesis and significance of nonprimary focal and segmental glomerulosclerosis.* Am J Kidney Dis, 1989. **13**(6): p. 443-56.
121. Deegens, J.K., E.J. Steenbergen, and J.F. Wetzels, *Review on diagnosis and treatment of focal segmental glomerulosclerosis.* Neth J Med, 2008. **66**(1): p. 3-12.
122. Maas, R.J., et al., *Minimal change disease and idiopathic FSGS: manifestations of the same disease.* Nat Rev Nephrol, 2016. **12**(12): p. 768-776.
123. Deegens, J.K., et al., *Podocyte foot process effacement as a diagnostic tool in focal segmental glomerulosclerosis.* Kidney Int, 2008. **74**(12): p. 1568-76.
124. Ranheim, T., et al., *Interaction between BTBR and C57BL/6J genomes produces an insulin resistance syndrome in (BTBR x C57BL/6J) F1 mice.* Arterioscler Thromb Vasc Biol, 1997. **17**(11): p. 3286-93.
125. Clee, S.M., S.T. Nadler, and A.D. Attie, *Genetic and genomic studies of the BTBR ob/ob mouse model of type 2 diabetes.* Am J Ther, 2005. **12**(6): p. 491-8.
126. Clee, S.M. and A.D. Attie, *The genetic landscape of type 2 diabetes in mice.* Endocr Rev, 2007. **28**(1): p. 48-83.
127. Hudkins, K.L., et al., *BTBR Ob/Ob mutant mice model progressive diabetic nephropathy.* J Am Soc Nephrol, 2010. **21**(9): p. 1533-42.
128. Brosius, F.C., 3rd, et al., *Mouse models of diabetic nephropathy.* J Am Soc Nephrol, 2009. **20**(12): p. 2503-12.
129. O'Donnell, M.P., et al., *Adriamycin-induced chronic proteinuria: a structural and functional study.* J Lab Clin Med, 1985. **106**(1): p. 62-7.
130. Wang, Y., et al., *Role of CD8(+) cells in the progression of murine adriamycin nephropathy.* Kidney Int, 2001. **59**(3): p. 941-9.
131. Wang, Y., et al., *Progressive adriamycin nephropathy in mice: sequence of histologic and immunohistochemical events.* Kidney Int, 2000. **58**(4): p. 1797-804.
132. Wang, Y.M., et al., *Adriamycin nephropathy in BALB/c mice.* Curr Protoc Immunol, 2015. **108**: p. 15 28 1-15 28 6.
133. Lee, V.W. and D.C. Harris, *Adriamycin nephropathy: a model of focal segmental glomerulosclerosis.* Nephrology (Carlton), 2011. **16**(1): p. 30-8.
134. Yang, J.W., et al., *Recent advances of animal model of focal segmental glomerulosclerosis.* Clin Exp Nephrol, 2018. **22**(4): p. 752-763.
135. Sun, Y.B., et al., *Glomerular endothelial cell injury and damage precedes that of podocytes in adriamycin-induced nephropathy.* PLoS One, 2013. **8**(1): p. e55027.
136. Guo, J., et al., *RAGE mediates podocyte injury in adriamycin-induced glomerulosclerosis.* J Am Soc Nephrol, 2008. **19**(5): p. 961-72.
137. Meyer-Schwesinger, C., G. Lambeau, and R.A. Stahl, *Thrombospondin type-1 domain-containing 7A in idiopathic membranous nephropathy.* N Engl J Med, 2015. **372**(11): p. 1074-5.

138. Seifert, L., et al., *The Most N-Terminal Region of THSD7A Is the Predominant Target for Autoimmunity in THSD7A-Associated Membranous Nephropathy.* J Am Soc Nephrol, 2018. **29**(5): p. 1536-1548.
139. Tomas, N.M., et al., *A Heterologous Model of Thrombospondin Type 1 Domain-Containing 7A-Associated Membranous Nephropathy.* J Am Soc Nephrol, 2017. **28**(11): p. 3262-3277.
140. Hershko, A. and A. Ciechanover, *The ubiquitin system.* Annu Rev Biochem, 1998. **67**: p. 425-79.
141. Pickart, C.M., *Mechanisms underlying ubiquitination.* Annu Rev Biochem, 2001. **70**: p. 503-33.
142. Ciechanover, A. and A.L. Schwartz, *The ubiquitin-proteasome pathway: the complexity and myriad functions of proteins death.* Proc Natl Acad Sci U S A, 1998. **95**(6): p. 2727-30.
143. Collins, G.A. and A.L. Goldberg, *The Logic of the 26S Proteasome.* Cell, 2017. **169**(5): p. 792-806.
144. Chau, V., et al., *A multiubiquitin chain is confined to specific lysine in a targeted short-lived protein.* Science, 1989. **243**(4898): p. 1576-83.
145. Thrower, J.S., et al., *Recognition of the polyubiquitin proteolytic signal.* EMBO J, 2000. **19**(1): p. 94-102.
146. Groll, M., et al., *Structure of 20S proteasome from yeast at 2.4 A resolution.* Nature, 1997. **386**(6624): p. 463-71.
147. Heinemeyer, W., et al., *The active sites of the eukaryotic 20 S proteasome and their involvement in subunit precursor processing.* J Biol Chem, 1997. **272**(40): p. 25200-9.
148. Kruger, E. and P.M. Kloetzel, *Immunoproteasomes at the interface of innate and adaptive immune responses: two faces of one enzyme.* Curr Opin Immunol, 2012. **24**(1): p. 77-83.
149. Aki, M., et al., *Interferon-gamma induces different subunit organizations and functional diversity of proteasomes.* J Biochem, 1994. **115**(2): p. 257-69.
150. Driscoll, J., et al., *MHC-linked LMP gene products specifically alter peptidase activities of the proteasome.* Nature, 1993. **365**(6443): p. 262-4.
151. Reichelt, J., et al., *Non-functional ubiquitin C-terminal hydrolase L1 drives podocyte injury through impairing proteasomes in autoimmune glomerulonephritis.* Nat Commun, 2023. **14**(1): p. 2114.
152. Meyer-Schwesinger, C., et al., *A new role for the neuronal ubiquitin C-terminal hydrolase-L1 (UCH-L1) in podocyte process formation and podocyte injury in human glomerulopathies.* J Pathol, 2009. **217**(3): p. 452-64.
153. Liu, Y., et al., *UCH-L1 expression of podocytes in diseased glomeruli and in vitro.* J Pathol, 2009. **217**(5): p. 642-53.
154. Pan, B.T. and R.M. Johnstone, *Fate of the transferrin receptor during maturation of sheep reticulocytes in vitro: selective externalization of the receptor.* Cell, 1983. **33**(3): p. 967-78.
155. Fruhbeis, C., D. Frohlich, and E.M. Kramer-Albers, *Emerging roles of exosomes in neuron-glia communication.* Front Physiol, 2012. **3**: p. 119.
156. Luga, V., et al., *Exosomes mediate stromal mobilization of autocrine Wnt-PCP signaling in breast cancer cell migration.* Cell, 2012. **151**(7): p. 1542-56.
157. Regev-Rudzki, N., et al., *Cell-cell communication between malaria-infected red blood cells via exosome-like vesicles.* Cell, 2013. **153**(5): p. 1120-33.
158. Roy, S., F.H. Hochberg, and P.S. Jones, *Extracellular vesicles: the growth as diagnostics and therapeutics; a survey.* J Extracell Vesicles, 2018. **7**(1): p. 1438720.
159. Karpman, D., A.L. Stahl, and I. Arvidsson, *Extracellular vesicles in renal disease.* Nat Rev Nephrol, 2017. **13**(9): p. 545-562.

160. van Niel, G., et al., *Challenges and directions in studying cell-cell communication by extracellular vesicles.* Nat Rev Mol Cell Biol, 2022. **23**(5): p. 369-382.
161. Wiklander, O.P.B., et al., *Advances in therapeutic applications of extracellular vesicles.* Sci Transl Med, 2019. **11**(492).
162. Wollert, T. and J.H. Hurley, *Molecular mechanism of multivesicular body biogenesis by ESCRT complexes.* Nature, 2010. **464**(7290): p. 864-9.
163. Colombo, M., et al., *Analysis of ESCRT functions in exosome biogenesis, composition and secretion highlights the heterogeneity of extracellular vesicles.* J Cell Sci, 2013. **126**(Pt 24): p. 5553-65.
164. Hsu, C., et al., *Regulation of exosome secretion by Rab35 and its GTPase-activating proteins TBC1D10A-C.* J Cell Biol, 2010. **189**(2): p. 223-32.
165. Meckes, D.G., Jr. and N. Raab-Traub, *Microvesicles and viral infection.* J Virol, 2011. **85**(24): p. 12844-54.
166. Mulcahy, L.A., R.C. Pink, and D.R. Carter, *Routes and mechanisms of extracellular vesicle uptake.* J Extracell Vesicles, 2014. **3**.
167. Sohal, I.S. and A.L. Kasinski, *Emerging diversity in extracellular vesicles and their roles in cancer.* Front Oncol, 2023. **13**: p. 1167717.
168. Erdbrugger, U., et al., *Urinary extracellular vesicles: A position paper by the Urine Task Force of the International Society for Extracellular Vesicles.* J Extracell Vesicles, 2021. **10**(7): p. e12093.
169. Akers, J.C., et al., *Biogenesis of extracellular vesicles (EV): exosomes, microvesicles, retrovirus-like vesicles, and apoptotic bodies.* J Neurooncol, 2013. **113**(1): p. 1-11.
170. Welsh, J.A., et al., *Minimal information for studies of extracellular vesicles (MISEV2023): From basic to advanced approaches.* J Extracell Vesicles, 2024. **13**(2): p. e12404.
171. Blijdorp, C.J., et al., *Nephron mass determines the excretion rate of urinary extracellular vesicles.* J Extracell Vesicles, 2022. **11**(1): p. e12181.
172. Barreiro, K., et al., *An in vitro approach to understand contribution of kidney cells to human urinary extracellular vesicles.* J Extracell Vesicles, 2023. **12**(2): p. e12304.
173. Pisitkun, T., R.F. Shen, and M.A. Knepper, *Identification and proteomic profiling of exosomes in human urine.* Proc Natl Acad Sci U S A, 2004. **101**(36): p. 13368-73.
174. Wen, H., et al., *Urinary excretion of aquaporin-2 in rat is mediated by a vasopressin-dependent apical pathway.* J Am Soc Nephrol, 1999. **10**(7): p. 1416-29.
175. Svenningsen, P., R. Sabaratnam, and B.L. Jensen, *Urinary extracellular vesicles: Origin, role as intercellular messengers and biomarkers; efficient sorting and potential treatment options.* Acta Physiol (Oxf), 2020. **228**(1): p. e13346.
176. Gamez-Valero, A., et al., *Urinary extracellular vesicles as source of biomarkers in kidney diseases.* Front Immunol, 2015. **6**: p. 6.
177. Merchant, M.L., et al., *Isolation and characterization of urinary extracellular vesicles: implications for biomarker discovery.* Nat Rev Nephrol, 2017. **13**(12): p. 731-749.
178. Erozenci, L.A., et al., *Urinary exosomal proteins as (pan-)cancer biomarkers: insights from the proteome.* FEBS Lett, 2019. **593**(13): p. 1580-1597.
179. Grange, C., et al., *Urinary Extracellular Vesicles Carrying Klotho Improve the Recovery of Renal Function in an Acute Tubular Injury Model.* Mol Ther, 2020. **28**(2): p. 490-502.
180. Dimuccio, V., et al., *Urinary CD133+ extracellular vesicles are decreased in kidney transplanted patients with slow graft function and vascular damage.* PLoS One, 2014. **9**(8): p. e104490.
181. Burrello, J., et al., *Identification of a serum and urine extracellular vesicle signature predicting renal outcome after kidney transplant.* Nephrol Dial Transplant, 2023. **38**(3): p. 764-777.

182. Blijdorp, C.J., et al., *Comparing Approaches to Normalize, Quantify, and Characterize Urinary Extracellular Vesicles.* J Am Soc Nephrol, 2021. **32**(5): p. 1210-1226.
183. Varderidou-Minasian, S. and M.J. Lorenowicz, *Mesenchymal stromal/stem cell-derived extracellular vesicles in tissue repair: challenges and opportunities.* Theranostics, 2020. **10**(13): p. 5979-5997.
184. Salih, M., et al., *An immunoassay for urinary extracellular vesicles.* Am J Physiol Renal Physiol, 2016. **310**(8): p. F796-F801.
185. Melentijevic, I., et al., *C. elegans neurons jettison protein aggregates and mitochondria under neurotoxic stress.* Nature, 2017. **542**(7641): p. 367-371.
186. Buzas, E.I., *The roles of extracellular vesicles in the immune system.* Nat Rev Immunol, 2023. **23**(4): p. 236-250.
187. Cooper, J.F., et al., *Stress increases in exopher-mediated neuronal extrusion require lipid biosynthesis, FGF, and EGF RAS/MAPK signaling.* Proc Natl Acad Sci U S A, 2021. **118**(36).
188. Wang, Y., et al., *Large vesicle extrusions from C. elegans neurons are consumed and stimulated by glial-like phagocytosis activity of the neighboring cell.* Elife, 2023. **12**.
189. Nicolas-Avila, J.A., et al., *A Network of Macrophages Supports Mitochondrial Homeostasis in the Heart.* Cell, 2020. **183**(1): p. 94-109 e23.
190. Turek, M., et al., *Muscle-derived exophers promote reproductive fitness.* EMBO Rep, 2021. **22**(8): p. e52071.
191. Arnold, M.L., et al., *Intermediate filaments associate with aggresome-like structures in proteostressed C. elegans neurons and influence large vesicle extrusions as exophers.* Nat Commun, 2023. **14**(1): p. 4450.
192. Yang, Y., et al., *Autophagy protein ATG-16.2 and its WD40 domain mediate the beneficial effects of inhibiting early-acting autophagy genes in C. elegans neurons.* Nat Aging, 2024. **4**(2): p. 198-212.
193. Wu, Z., et al., *Nonapoptotic role of EGL-1 in exopher production and neuronal health in Caenorhabditis elegans.* Proc Natl Acad Sci U S A, 2025. **122**(2): p. e2407909122.
194. Tomas, N.M., et al., *Autoantibodies against thrombospondin type 1 domain-containing 7A induce membranous nephropathy.* J Clin Invest, 2016. **126**(7): p. 2519-32.
195. Seifert, L., et al., *An antigen-specific chimeric autoantibody receptor (CAAR) NK cell strategy for the elimination of anti-PLA2R1 and anti-THSD7A antibody-secreting cells.* Kidney Int, 2024. **105**(4): p. 886-889.
196. Sosna, J., et al., *The proteases HtrA2/Omi and UCH-L1 regulate TNF-induced necroptosis.* Cell Commun Signal, 2013. **11**: p. 76.
197. Augert, A., et al., *PLA2R1 kills cancer cells by inducing mitochondrial stress.* Free Radic Biol Med, 2013. **65**: p. 969-977.
198. Boerries, M., et al., *Molecular fingerprinting of the podocyte reveals novel gene and protein regulatory networks.* Kidney Int, 2013. **83**(6): p. 1052-64.
199. Takemoto, M., et al., *A new method for large scale isolation of kidney glomeruli from mice.* Am J Pathol, 2002. **161**(3): p. 799-805.
200. Somogyi, P. and H. Takagi, *A note on the use of picric acid-paraformaldehyde-glutaraldehyde fixative for correlated light and electron microscopic immunocytochemistry.* Neuroscience, 1982. **7**(7): p. 1779-83.
201. Gaffling, S., et al., *A Gauss-Seidel iteration scheme for reference-free 3-D histological image reconstruction.* IEEE Trans Med Imaging, 2015. **34**(2): p. 514-30.
202. Witwer, K.W., et al., *Updating MISEV: Evolving the minimal requirements for studies of extracellular vesicles.* J Extracell Vesicles, 2021. **10**(14): p. e12182.
203. Blankenburg, S., et al., *Improving Proteome Coverage for Small Sample Amounts: An Advanced Method for Proteomics Approaches with Low Bacterial Cell Numbers.* Proteomics, 2019. **19**(23): p. e1900192.

204. Kolberg, L., et al., *gprofiler2 -- an R package for gene list functional enrichment analysis and namespace conversion toolset g:Profiler.* F1000Res, 2020. **9**.
205. Simon P. Couch, A.P.B., Chester Ismay, Evgeni and B.S.B. Chasnovski, and Mine Çetinkaya-Rundel, *infer: An R package for tidyverse-friendly statistical inference.* Journal of Open Source Software, 2021. **6**.
206. Wilke, C.O.W.B., *ggtext: improved text rendering support for 'ggplot2'*. 2022.
207. Hester, J.B.J., *glue*
208. van den Brand, T., *ggh4x*.
209. Ashburner, M., et al., *Gene ontology: tool for the unification of biology. The Gene Ontology Consortium.* Nat Genet, 2000. **25**(1): p. 25-9.
210. Artelt, N., et al., *Comparative Analysis of Podocyte Foot Process Morphology in Three Species by 3D Super-Resolution Microscopy.* Front Med (Lausanne), 2018. **5**: p. 292.
211. Thomas, P.E., et al., *GLEPP1, a renal glomerular epithelial cell (podocyte) membrane protein-tyrosine phosphatase. Identification, molecular cloning, and characterization in rabbit.* J Biol Chem, 1994. **269**(31): p. 19953-62.
212. Arnold, M.L., et al., *Quantitative Approaches for Scoring in vivo Neuronal Aggregate and Organelle Extrusion in Large Exopher Vesicles in C. elegans.* J Vis Exp, 2020(163).
213. Nicolas-Avila, J.A., et al., *Macrophages, Metabolism and Heterophagy in the Heart.* Circ Res, 2022. **130**(3): p. 418-431.
214. Blumenthal, A., et al., *Morphology and migration of podocytes are affected by CD151 levels.* Am J Physiol Renal Physiol, 2012. **302**(10): p. F1265-77.
215. van de Logt, A.E., J.M. Hofstra, and J.F. Wetzels, *Serum anti-PLA2R antibodies can be initially absent in idiopathic membranous nephropathy: seroconversion after prolonged follow-up.* Kidney Int, 2015. **87**(6): p. 1263-4.
216. Ramachandran, R., et al., *Serial monitoring of anti-PLA2R in initial PLA2R-negative patients with primary membranous nephropathy.* Kidney Int, 2015. **88**(5): p. 1198-9.
217. van Niel, G., G. D'Angelo, and G. Raposo, *Shedding light on the cell biology of extracellular vesicles.* Nat Rev Mol Cell Biol, 2018. **19**(4): p. 213-228.
218. Thery, C., et al., *Minimal information for studies of extracellular vesicles 2018 (MISEV2018): a position statement of the International Society for Extracellular Vesicles and update of the MISEV2014 guidelines.* J Extracell Vesicles, 2018. **7**(1): p. 1535750.
219. Colombo, M., G. Raposo, and C. Thery, *Biogenesis, secretion, and intercellular interactions of exosomes and other extracellular vesicles.* Annu Rev Cell Dev Biol, 2014. **30**: p. 255-89.
220. Yanez-Mo, M., et al., *Biological properties of extracellular vesicles and their physiological functions.* J Extracell Vesicles, 2015. **4**: p. 27066.
221. Alpers, C.E. and K.L. Hudkins, *Mouse models of diabetic nephropathy.* Curr Opin Nephrol Hypertens, 2011. **20**(3): p. 278-84.
222. Cloutier, N., et al., *The exposure of autoantigens by microparticles underlies the formation of potent inflammatory components: the microparticle-associated immune complexes.* EMBO Mol Med, 2013. **5**(2): p. 235-49.
223. Nielsen, C.T., et al., *Increased IgG on cell-derived plasma microparticles in systemic lupus erythematosus is associated with autoantibodies and complement activation.* Arthritis Rheum, 2012. **64**(4): p. 1227-36.
224. Zhao, W.J., et al., *Gene expression profiling identifies the novel role of immunoproteasome in doxorubicin-induced cardiotoxicity.* Toxicology, 2015. **333**: p. 76-88.
225. Dimitrakis, P., et al., *Effects of doxorubicin cancer therapy on autophagy and the ubiquitin-proteasome system in long-term cultured adult rat cardiomyocytes.* Cell Tissue Res, 2012. **350**(2): p. 361-72.

226. Montalvo, R.N., et al., *Doxorubicin-induced oxidative stress differentially regulates proteolytic signaling in cardiac and skeletal muscle.* Am J Physiol Regul Integr Comp Physiol, 2020. **318**(2): p. R227-R233.
227. Buzas, E.I., et al., *Molecular interactions at the surface of extracellular vesicles.* Semin Immunopathol, 2018. **40**(5): p. 453-464.
228. Vistoli, G., et al., *Advanced glycoxidation and lipoxidation end products (AGEs and ALEs): an overview of their mechanisms of formation.* Free Radic Res, 2013. **47 Suppl 1**: p. 3-27.
229. Neale, T.J., et al., *Proteinuria in passive Heymann nephritis is associated with lipid peroxidation and formation of adducts on type IV collagen.* J Clin Invest, 1994. **94**(4): p. 1577-84.
230. Solin, M.L., et al., *Lipid peroxidation in human proteinuric disease.* Kidney Int, 2001. **59**(2): p. 481-7.
231. Gerke, V., C.E. Creutz, and S.E. Moss, *Annexins: linking Ca2+ signalling to membrane dynamics.* Nat Rev Mol Cell Biol, 2005. **6**(6): p. 449-61.
232. Koerdt, S.N., A.P.K. Ashraf, and V. Gerke, *Annexins and plasma membrane repair.* Curr Top Membr, 2019. **84**: p. 43-65.
233. Jeppesen, D.K., et al., *Reassessment of Exosome Composition.* Cell, 2019. **177**(2): p. 428-445 e18.
234. Jones, D.H., et al., *Expression and structural analysis of 14-3-3 proteins.* J Mol Biol, 1995. **245**(4): p. 375-84.
235. Bustad, H.J., et al., *The peripheral binding of 14-3-3gamma to membranes involves isoform-specific histidine residues.* PLoS One, 2012. **7**(11): p. e49671.
236. Martin, H., et al., *Subcellular localisation of 14-3-3 isoforms in rat brain using specific antibodies.* J Neurochem, 1994. **63**(6): p. 2259-65.
237. Faul, C., et al., *The actin cytoskeleton of kidney podocytes is a direct target of the antiproteinuric effect of cyclosporine A.* Nat Med, 2008. **14**(9): p. 931-8.
238. Alexopoulos, E., et al., *Induction and long-term treatment with cyclosporine in membranous nephropathy with the nephrotic syndrome.* Nephrol Dial Transplant, 2006. **21**(11): p. 3127-32.
239. Dias, C. and J. Nylandsted, *Plasma membrane integrity in health and disease: significance and therapeutic potential.* Cell Discov, 2021. **7**(1): p. 4.
240. Reddy, A., E.V. Caler, and N.W. Andrews, *Plasma membrane repair is mediated by Ca(2+)-regulated exocytosis of lysosomes.* Cell, 2001. **106**(2): p. 157-69.
241. Rood, I.M., et al., *Increased expression of lysosome membrane protein 2 in glomeruli of patients with idiopathic membranous nephropathy.* Proteomics, 2015. **15**(21): p. 3722-30.
242. Lee, D., et al., *Expression of the transmembrane lysosomal protein SCARB2/Limp-2 in renin secretory granules controls renin release.* Nephron Exp Nephrol, 2012. **122**(3-4): p. 103-13.
243. Schmid, J., et al., *Parallel regulation of renin and lysosomal integral membrane protein 2 in renin-producing cells: further evidence for a lysosomal nature of renin secretory vesicles.* Pflugers Arch, 2013. **465**(6): p. 895-905.
244. Fujigaki, Y., M. Nagase, and N. Honda, *Intraglomerular basement membrane translocation of immune complex (IC) in the development of passive in situ IC nephritis of rats.* Am J Pathol, 1993. **142**(3): p. 831-42.
245. Hengel, F.E., et al., *Autoantibodies Targeting Nephrin in Podocytopathies.* N Engl J Med, 2024. **391**(5): p. 422-433.

7 Supplement

Table S1

Supplement table 1: Blood and urine parameters of patients with membranous nephropathy at time points of analyses (U1= diagnostic samples; Ux = follow up samples)

	THSD7A$^+$-MN								**PLA$_2$R1$^+$-MN**	
gender	male								female	
age	62	62	63	64	64	64	64	64	19	21
collection time point	U1	U2	U3	U4	U5	U6	U7	U8	U1	U2
GFR (CKD-EPI; ml/min)	>90	64	16 (-)	33 (-)	29 (-)	29 (-)	31 (-)	41 (-)	>90	>90
blood urea nitrogen (mg/dL)	54	71 (+)	130 (+)	92 (+)	81 (+)	79 (+)	82 (+)	65 (+)	17	20
serum triglycerides (mg/dL)	310 (+)	183 (+)	218 (+)	147	211 (+)	195 (+)	121	90	226 (+)	
serum cholesterol (mg/dL)	442 (+)	286 (+)	307 (+)	173	213 (+)	214 (+)	185	147	380 (+)	
serum albumin (g/L)	12.4 (-)	11.0 (-)	10.6 (-)	23.1 (-)	19.3 (-)	22.4 (-)	28.9 (-)	30.8 (-)	17.3 (-)	35.9
serum THSD7A titer (IFT)	1:160	1:160	1:160	Neg.	1:10	Neg.	Neg.	Neg.	Neg.	
serum PLA$_2$R1-AutoAK (U/ml)	Neg.	0.8							92.5 (+)	Neg.
urine creatinine (g/L)	1.11	0.15 (-)	0.44	0.91	0.62	0.92	1.40	0.13 (-)	0.79	1.57 (+)
urine protein (mg/L)	14852 (+)	3172 (+)	8215 (+)	12099 (+)	8674 (+)	12987 (+)	11551 (+)	821 (+)	10647 (+)	2582 (+)
urine albumin (mg/L)	10500 (+)	2252 (+)	4138 (+)	9003 (+)	6853 (+)	9141 (+)	8583 (+)	617 (+)	7452 (+)	1760 (+)
urine protein-creatinine (mg/g)	13376 (+)	20571 (+)	18670 (+)	13265 (+)	13885 (+)	14186 (+)	8228 (+)	6436 (+)	13474 (+)	1640 (+)
urine albumin-creatinine (mg/g)	9456 (+)	14604 (+)	9404 (+)	9870 (+)	10970 (+)	9984 (+)	6114 (+)	4839 (+)	9430 (+)	1118 (+)
urine IgG (mg/L)	473 (+)									57 (+)
urine □2-macroglobulin (mg/L)	2.93									<2.50
urine spec. weight	1.105									1.005
urine pH	~6									~6
urine ketones (mg/dL)	Neg.									Neg.
urine urobilinogen (mg/dL)	Neg.									Neg.
urine bilirubin (mg/dL)	Neg.									Neg.
urine glucose (mg/dL)	Neg.									~100 (+)
urine nitrite	Neg.									Neg.
urine erythrocytes (per µL)	~25 (+)									~10 (+)
urine leukocytes (per µL)	Neg.									~100 (+)

Table S2

Supplement table 2: Blood and urine parameters of nephrotic control patients at time points of analyses (U1 = diagnostic samples)

	MCD	IgAN	Tubulo-toxic kidney injury	pFSGS
gender	female	female	male	male
age	82	58	64	68
collection time point	U1	U1	U1	U1
GFR (CKD-EPI; ml/min)	12 (-)	25 (-)	13 (-)	15 (-)
blood urea nitrogen (mg/dL)	258 (+)	72 (+)	174 (+)	150 (+)
serum triglycerides (mg/dL)	255 (+)			248 (+)
serum cholesterol (mg/dL)	221 (+)			
serum albumin (g/L)	14.8 (-)	41.7	23.4 (-)	23.5 (-)
serum THSD7A titer (IFT)	Neg.	Neg.		
serum PLA_2R1-AutoAK (U/ml)	Neg.	Neg.	Neg.	Neg.
urine creatinine (g/L)	0.78		0.47	0.41
urine protein (mg/L)	13688 (+)		3390 (+)	2591 (+)
urine albumin (mg/L)	9481 (+)	2565 (+)	1690 (+)	1942 (+)
urine protein-creatinine (mg/g)	17441 (+)		7217 (+)	6272 (+)
urine albumin-creatinine (mg/g)	12080 (+)	3103 (+)	3598 (+)	4001 (+)
urine spec. weight				
urine pH				
urine ketones (mg/dL)				
urine urobilinogen (mg/dL)				
urine bilirubin (mg/dL)				
urine glucose (mg/dL)				
urine nitrite				
urine erythrocytes (per µL)				
urine leukocytes (per µL)				

Figure S1

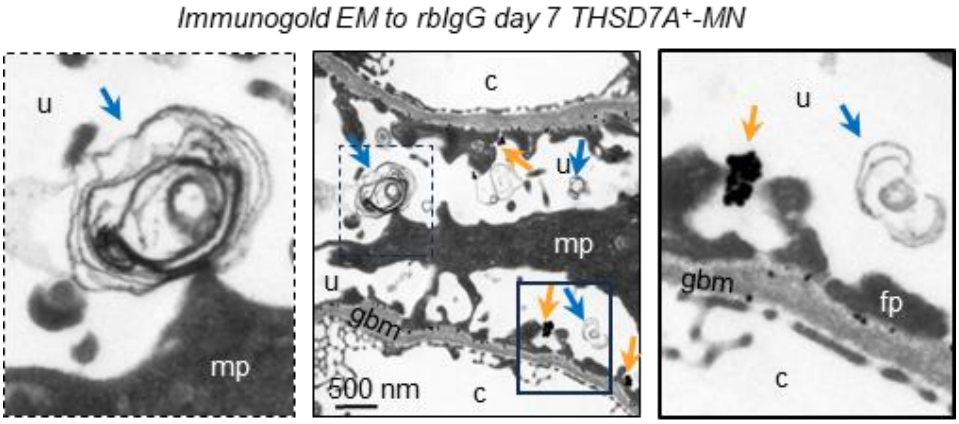

Supplement figure 1: Immunogold EM to rbIgG in a day 7 THSD7A$^+$-MN glomerulus. Blue arrows highlight gold-free membrane whorls in the urinary space (u), orange arrows = gold-labeled exopher-like vesicles, gbm = glomerular basement membrane, fp = foot process, c = capillary lumen, mp = major process

8 Acknowledgements

First and foremost, I would like to express my deepest gratitude to Prof. Dr. Catherine Meyer-Schwesinger. Without her expertise, unbelievable motivation, and steadfast support, both professionally and personally, this thesis would not have been possible. Her openness, thoughtful criticism, and incredible encouragement have shaped this work profoundly. I am truly grateful for the opportunity to be part of your lab, for the stimulating discussions, and for the trust you placed in me throughout this journey. I could not have imagined a better supervisor and mentor.

I would also like to thank Prof. Dr. Julia Kehr for kindly agreeing to supervise my work in the department of biology.

A heartfelt thank you goes to Prof. Dr. Tobias N. Meyer from the Asklepios Clinic Barmbek for providing patient urine samples and supporting my thesis. Thanks as well to his great team for making the process run so smoothly.
I would also like to thank all collaborators who made essential contributions to this work. In particular, Prof. Dr. Lars Fester and PD Dr. Oliver Kretz for the electron microscopic analyses, and the group of Prof. Dr. Uwe Völker for the proteomic analysis.

To my amazing lab: thank you for the daily laughter, the scientific exchange, the sense of community and your support in every situation. Your help was indispensable, both scientifically and personally. Working alongside you has made every single day in the lab not only productive but genuinely enjoyable.

I am deeply grateful to my family, my parents and my sister, for their unwavering support and belief in me throughout my life. Your encouragement has been the foundation of my personal and academic path. The emotional and mental support from you has always been invaluable to continue moving forward. My deepest thanks also go to Marten, for your patience, love, and strong support. Especially during the most stressful times, I was glad to have you by my side. Thanks to the best family, for your endless motivation, and for being the ones I can always count on, knowing I had you in my back made all the difference!

Lastly, I would like to thank my friends and the best teammates at the amazing sports club Hamburg GAA. You gave me the perfect space to switch off and recharge. After long and exhausting days, stepping onto the pitch with you was the best remedy, fighting for every ball, laughing, and sharing unforgettable tournaments and training sessions. Massive thanks for your support, for the conversations over a good beer, thoughtful care packages during stressful times, celebrations, and the always fun travels. Having friends like you keeps me going and never fails to put a smile on my face, you are incredible!

9 Eidesstattliche Erklärung

Hiermit versichere ich an Eides statt, die vorliegende Dissertationsschrift selbst verfasst und keine anderen als die angegebenen Hilfsmittel und Quellen benutzt zu haben. Sofern im Zuge der Erstellung der vorliegenden Dissertationsschrift generative Künstliche Intelligenz (gKI) basierte elektronische Hilfsmittel verwendet wurden, versichere ich, dass meine eigene Leistung im Vordergrund stand und dass eine vollständige Dokumentation aller verwendeten Hilfsmittel gemäß der Guten wissenschaftlichen Praxis vorliegt. Ich trage die Verantwortung für eventuell durch die gKI generierte fehlerhafte oder verzerrte Inhalte, fehlerhafte Referenzen, Verstöße gegen das Datenschutz- und Urheberrecht oder Plagiate.

Affidavit:

I hereby declare and affirm that this doctoral dissertation is my own work and that I have not used any aids and sources other than those indicated. If electronic resources based on generative artificial intelligence (gAI) were used in the course of writing this dissertation, I confirm that my own work was the main and value-adding contribution and that complete documentation of all resources used is available in accordance with good scientific practice. I am responsible for any erroneous or distorted content, incorrect references, violations of data protection and copyright law or plagiarism that may have been generated by the gAI.

Hamburg, 21.05.2025

Ort, Datum

Unterschrift

10 List of publications

Parts of the thesis are published as a preprint on bioRxiv server:

Lahme, K. et al. *Podocyte exopher-formation as a novel pathomechanism in membranous nephropathy*. Biorxiv, 2024.

doi: https://doi.org/10.1101/2024.04.04.588146